UCLA
UCLA Electronic Theses and Dissertations

Title
MEMS multi-pole electromagnets: Compact electron optics and undulators

Permalink
https://escholarship.org/uc/item/8dj562hs

Author
Harrison, Jere Charles

Publication Date
2014

Peer reviewed|Thesis/dissertation

eScholarship.org Powered by the California Digital Library
University of California

University of California
Los Angeles

MEMS multi-pole electromagnets: Compact electron optics and undulators

A dissertation submitted in partial satisfaction
of the requirements for the degree
Doctor of Philosophy in Electrical Engineering

by

Jere Harrison

2014

© Copyright by
Jere Harrison
2014

Abstract of the Dissertation

MEMS multi-pole electromagnets: Compact electron optics and undulators

by

Jere Harrison

Doctor of Philosophy in Electrical Engineering

University of California, Los Angeles, 2014

Professor Rob N. Candler, Co-chair

Professor Jack W. Judy, Co-chair

MEMS electromagnets occupy a unique niche in the design space of magnetic devices: they are small enough that length-scaling enables Tesla-scale field intensity and kTesla-scale field gradient, but large enough that power dissipation does not exceed practical power density limits for conductive cooling. This work demonstrates the first application of MEMS electromagnets to charged particle beam optics. Particle beam optics are an important component in beam transport systems for medical and scientific instruments such as Hadron therapy for cancer treatment and free electron lasers for high energy coherent light production. These MEMS devices promise smaller and higher performance instruments using the performance scaling that results from reducing the electromagnet gap. This work demonstrated a MEMS multi-pole $Ni_{80}Fe_{20}$-yoke electromagnet with a 600-μm pole-pole gap producing a 24-mT dipole field at 3 A, steering a 34-keV electron beam in two dimensions without measurable hysteresis. The same multi-pole electromagnet producing a 220-T/m quadrupole field gradient at 4.7 A was used to focus a 34-keV electron beam. The spatial distribution of the quadrupole field was characterized using a novel electron beam-probe method. Simulations project that 4-pole electromagnets with 100 μm pole-pole gap electromagnets and a 200 μm thick $Co_{57}Ni_{13}Fe_{30}$ yoke will produce 850 mT dipole fields and 20,000 T/m quadrupole field gradients, exceeding all published quadrupole optics by more than an order of magnitude.

The dissertation of Jere Harrison is approved.

Pietro Musuemci

Jack W. Judy, Committee Co-chair

Rob N. Candler, Committee Co-chair

University of California, Los Angeles

2014

Dedicated to the memory of Ira Goldberg,
whose insights form the basis for this work,
and the memory of Hannah Bartle,
whose wit, laughter, and love taught me to love life.

Table of Contents

List of Figures

List of Tables

Acknowledgments

Special thanks to Jack Judy for starting me on this journey, my friends for keeping me sane through it, and Rob Candler for seeing me to the end of it.

Vita

1985	Born, Phoenix, Arizona, USA
2004-2005	Design Engineer Intern ADTRAN, Inc. Phoenix, Arizona
2005-2008	Undergraduate Research Assistant Arizona State University Tempe, Arizona
2008	Bachelor of Science in Electrical Engineering, *summa cum laude* Arizona State University Tempe, Arizona Minor in Mathematics and an honors degree from Barrett Honors College Thesis: Characterization of nano-structure tuned MEMS microphones
2006-2008	Engineer Department of Defense Fort Meade, Maryland
2009	Process Engineer Intern Innovative Micro Technology Goleta, California
2009-2012	Teaching Assistant and Graduate Student Researcher University of California, Los Angeles Los Angeles, California

2011	Master of Science in Electrical Engineering University of California, Los Angeles Los Angeles, California Thesis: Design analysis and fabrication process development for a micro-fabricated magnetostatic RF switch
2012-2014	Ph.D. Candidate University of California, Los Angeles Los Angeles, California
2014	Doctor of Philosophy in Electrical Engineering University of California, Los Angeles Los Angeles, California
2014-Present	Chief Technology Officer Theia Scientific Corporation Los Angeles, California

Publications and Presentations

SS Je, J Harrison, I Deligoz, B Bakkaloglu, S Kiaei, and J Chae, "Microdevices and front-end interface circuitry for hearing aids", Proceedings of the Sensor, Signal and Information Processing (SenSIP) Workshop, Sedona, AZ, 05/11-14/2008.

SS Je, J Kim, J Harrison, MN Kozicki, and J Chae, "*In situ* tuning of omnidirectional micro-electro-mechanical-systems microphones to improve performance fit in hearing aids", Applied Physics Letters, vol. 93, no. 12, 035015, 2008.

SS Je, J Harrison, M Kozicki, and J Chae, "*In situ* tuning of micro devices for directional

microphone application", Technical Digest of the 2008 Solid-state Sensors, Actuators and Microsystems Workshop, Hilton Head Isl., SC, 06/01/2008 Transducer Research Foundation, Cleveland, pp. 232-235, 2008.

SS Je, J Harrison, MN Kozicki, B Bakkaloglu, S Kiaei, and J Chae, "*In situ* tuning of a MEMS microphone using electrodeposited nano structures", Journal of Micromechanics and Microengineering, vol. 19, no. 3, 2009.

M Glickman, P Tseng, J Harrison, IB Goldberg, P Johnson, P Smeys, T Niblock, JW Judy, "CMOS-compatible back-end process for in-plane actuating ferromagnetic MEMS", Technical Digest of the 2009 Solid-state Sensors, Actuators and Microsystems Conference (TRANSDUCERS 2009), Denver, CO, 6/21/2009, IEEE, New Jersey, pp. 248-251.

M Glickman, J Harrison, T Niblock, I Goldberg, P Tseng, and JW Judy, "High Permeability Permalloy for MEMS", Technical Digest of the 2010 Solid-state Sensors, Actuators and Microsystems Workshop, Hilton Head Isl., SC, 06/06/2010 Transducer Research Foundation, Cleveland, pp. 328-332, 2010.

M Glickman, P Tseng, J Harrison, T Niblock, IB Goldberg, and JW Judy, "High-performance lateral-actuating magnetic MEMS switch", Journal of Microelectromechanical Systems, vol. 20, no. 4, pp. 842-851, 2011.

J Harrison, X Wu, and R Candler, "CMOS-Compatible Surface-Micromachined RF-Relay", 2011 UCLA Annual Research Review, November 14, 2011.

M Culjat, C Wottawa, W Grundfest, R Candler, O Paydar, J Harrison, X Wu, and R Fan, Sterilizible force sensor for surgical or remote grasper tools, US Provisional Patent 61/693,915, 2012.

J Harrison, A Joshi, J Lake, R Candler, and P Musumeci, "Surface-micromachined magnetic undulator with period length between 10 μm and 1 mm for advanced light sources", Physical Review Special Topics: Accelerators and Beams, vol. 15, 070703, 2012.

J Harrison and A Joshi, Surface micromachined magnetic undulator, US Patent Application WO2013112226 A3, 2013.

R Candler, O Stafsudd, P Musumeci, J Harrison, and A Joshi, Surface micro-machined multi-pole electromagnets, US Provisional Patent 61/892,968, 2013.

J Harrison and R Candler, "Microfabricated multi-pole electromagnets for particle beam manipulation", 2013 UCLA Annual Research Review, December 11, 2013.

R Candler and J Harrison, Stacked micro-machined multi-pole electromagnet, US Provisional Patent US 61/892,976, 2014.

J Harrison, O Paydar, Y Hwang, J Wu, E Threlkeld, P Musumeci, and R Candler, "Fabrication process for thick-film micromachined multi-pole electromagnets", Journal of Microelectromechanical Systems, vol. 23, no. 3, pp. 505-507, 2014.

J Harrison, J Wu, O Paydar, Y Hwang, E Threlkeld, J Rosenzweig, P Musumeci, and R Candler, "High-gradient electromagnets for particle beam manipulation", Technical Digest of the 2014 Solid-state Sensors, Actuators and Microsystems Workshop, Hilton Head Isl., SC, 06/08/2014 Transducer Research Foundation, Cleveland, pp. 60-63, 2014.

J Lake and J Harrison, Post process tuning of quality factor using a stress layer to modify structure and anchor stress, US Provisional Patent 61/940,244, 2014.

J Harrison, A Joshi, Y Hwang, O Paydar, J Lake, P Musumeci, and R Candler, "Surface-

micromachined electromagnets for 100 μm-scale undulators and focusing optics", Physics Procedia, vol. 52, pp. 19-26, 2014.

CHAPTER 1

Introduction

CONTINUOUS IMPROVEMENTS over the last century in the understanding and control of charged particle beams have led to revolutionary scientific discoveries [Gol76, CKS13], live-saving medical technologies [Wil46, GKP10], and advanced tools for manufacturing [MS60, BEH86] and metrology [KR32, RPB57]. Magnetic optics play a key role in these particle beam systems, controlling the motion, focus, and dispersion of high-energy particle beams.

Manipulation of charged particle beam motion is accomplished through the Lorentz force, $\gamma m\vec{a} = \vec{F} = q(\vec{E} + \vec{v} \times \vec{B})$, where γ is the Lorentz factor, m is the particle mass, a is particle acceleration, F is relativistic Lorentz force, q is the particle charge, E is electric field, v is particle velocity, and B is magnetic flux density. Static electric fields are limited by field emission and Paschen breakdown to 100 MV/m-scale, while electromagnet heating limits resistive electromagnets to Tesla-scale intensity. For particles traveling faster than 1/3 the speed of light, a Tesla-scale magnetic fields displace a beam more strongly than a 100 MV/m-scale electric field, making magnetic optics the preferred technology. Further, magnetic fields only produce forces transverse to particle motion, conserving beam momentum and simplifying beam transport systems.

The last 30 years have also seen a revolution in manufacturing technology, where tooling developed for the integrated circuit industry has been employed on a more general set of problems. Micro-electromechanical systems, or MEMS, is the science, techniques, and systems developed in the size-scale between 1 μm and 1 mm—beyond the precision of traditional machining, but larger than systems produced by the chemistry and self-assembly techniques of nanotechnology. Today, MEMS manufacturing techniques are being employed

wherever performance can be improved or cost can be reduced by shrinking the size of a system. This has led to high-performance microphones [WBB06], accelerometers [FHW04], and gyroscopes [TSS09] in every cellular phone, high-resolution projectors [Hor97] in every theater and conference room, micro-scale DNA biosensors [BNN11] in medical laboratories, portable chemical sensors [KBC12] for environmental monitoring, and even chip-scale atomic clocks [KSS04] in satellites.

This dissertation presents the first application of MEMS to magnetic optics for charged particle beams. This chapter introduces the scaling laws that motivate this work. Chapter 2 discusses prior work in the area of magnetic optics. Chapter 3 presents the design techniques employed in this work for magnetic optics and systems. Chapter 4 presents the fabrication techniques used to manufacture the devices presented in this work. Chapter 5 presents the characterization of the manufactured devices. Chapter 6 discusses the ongoing work to produce light from a microfabricated undulator. Chapter 7 concludes this work. Appendices A, B, and C contain data processing and simulation scripts and the fabrication traveller used during the manufacture of these MEMS magnetic optics.

1.1 Historical improvement of beam quality

A typical particle beam system starts with a charged particle source, a cathode in the case of an electron beam or a plasma in the case of an ion beam, followed by an acceleration stage, either by a static potential or a phase-matched periodic electric field, and a beam transport system consisting of dipoles, quadrupoles, and sextupoles to condition the beam and project it to a desired location. The performance of particle beam-based systems is directly tied to the quality of the charged particle beam, which has led to a concerted research effort over several decades to to improve the performance of particle beam system components.

One measure of beam quality that underlies compatibility with miniaturized optics is emittance—the spread in position and momentum of a particle beam. The normalized root-mean-square (rms) transverse emittance (ε_n) sets the minimum product of a beam's spot size and angular divergence and is conserved throughout linear transformations of the beam,

such as deflection, focusing, and dispersion. With a small emittance (mm-mrad-scale), a particle beam can be focused for insertion into the sub-mm bore of MEMS beam optics.

Early charged particle beams had emittance greater than 10 mm×mrad and several percent energy spread, leading to mm-scale transverse beam sizes, rapid angular divergence, and a longitudinal spread in focal length. Field emission electron sources and radiation damping in synchrotron storage rings can produce beams with 0.01 mm-mrad-scale emittance, but suffer from other limitations. The emitting area of field emission sources are too small to produce the large beam current (100+ A) required for light sources and beams in a storage ring have large emittance until they have traversed the ring many times. Photoinjector technology [RBH94] producing reliable electron beams with sub-1-mm-mrad transverse emittance was developed in the late 2000's, making MEMS magnetic optics and undulators a possible alternative to traditionally machined devices. Beams from thermionic sources and laser-plasma wakefield sources have recently become compatible with MEMS-scale beam optics as well. Figure 1.1 shows improvement of normalized rms transverse emittance over time for several commissioned electron guns.

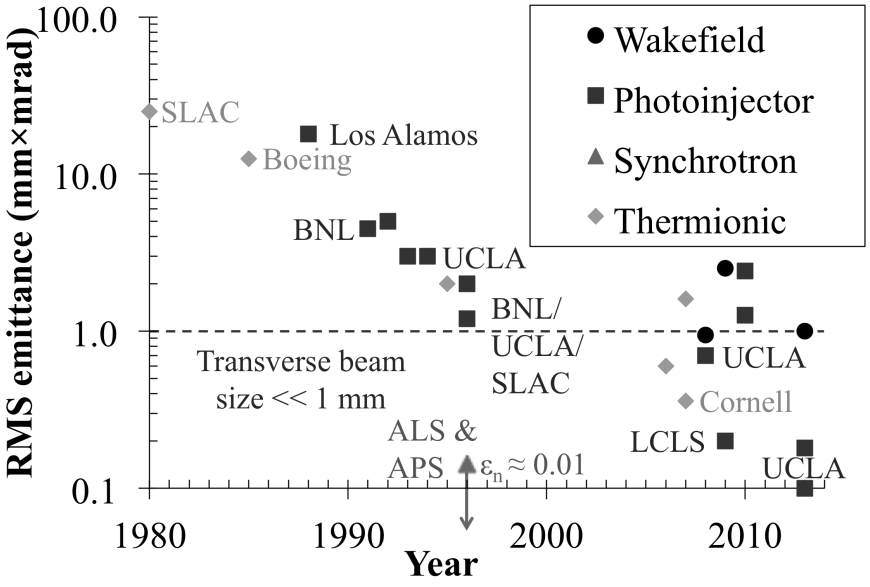

Figure 1.1: Normalized transverse rms emittance vs. commissioning year for high-current electron sources [Dow10, SGF88, RBH94, DCS95, OS99, Shi06, DSB07, MME08, Cen14, SBK10, Sch13]. Emittance is reported in the standard convention of the product of spot-width in mm and divergence in mrad. The beams circulating in synchrotron storage rings have emittance on the order of 10^{-3} mm×mrad because of radiation damping.

Recent breakthroughs in compact laser accelerators using dielectric structures [NVP12] and plasma wakes [WIW10, WRP12] promise to dramatically reduce the size of particle accelerators while maintaining the ultra-low emittance and low energy spread of modern RF-photoinjector sources, promising a dramatic reduction in the size and cost of particle beam sources. The size and performance of particle beam optics and undulators, however, has not seen the same rapid progress as beam sources.

1.2 Multi-pole field scaling

Lorentz force optics producing dipole, quadruple, and higher order fields control the direction, focus, and dispersion in particle beams [Lee04]. Improving the size and performance of the beam transport system is necessary to realize the potential of the next generation of beam sources and systems. The large angular divergence of laser plasma wakefield accelerated beams, for example, necessitate immediate and high-gradient focusing to minimize bunch elongation and reduction in beam current [WFP11]. High gradient focusing of high-current beams will also improve the efficiency of particle-beam based light sources, matching the particle beam width to the optimal size of the optical beam in free electron laser [Xie00] and inverse Compton scattering (ICS) sources [SLC96, PBH00].

Many linear manipulations of the 3-D momentum and position of a charged particle beam are possible with well controlled magnetic fields. A simple 4-pole electromagnet can produce both steering and focusing fields (Figure 1.2), and the field intensity from these electromagnets improves with a reduction in the gap between the electromagnet poles.

Particle beam deflection is accomplished with a dipole magnetic field. Solving the Lorentz force for a particle moving through a dipole field results in the momentum-normalized equation of motion, $R^{-1} = qB/p$, where R is the radius of curvature, B is the magnetic field, q is the particle charge, and p is the particle momentum. For a small-gap dipole electromagnet with a high-permeability yoke, magnetic circuit analysis approximates magnetic field intensity as $B = \mu nI/2r$, where μ is the permeability of free space, n is the number of electromagnet turns, I is the electromagnet current and r is the distance between the center

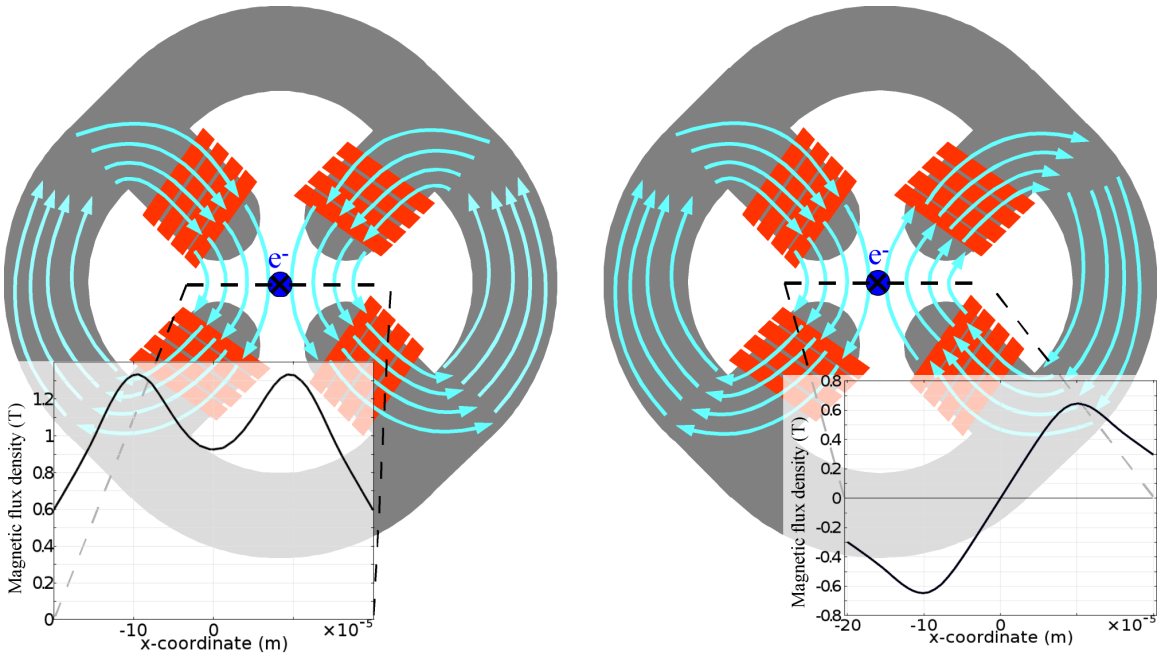

Figure 1.2: Illustration showing the layout of a 4-pole electromagnet producing (a) dipole steering fields or (b) quadrupole focusing fields. Gray shows the electromagnet yoke and poles, orange shows the top of the electromagnet windings, blue shows the electron beam location, and cyan lines show the flow of magnetic flux. The inset plots show example field magnitude along the marked transverse direction of the electromagnet.

of the gap and pole tip. Simple scaling of the transverse dimensions from the cm-scale of traditional systems to sub-mm-scale of MEMS results in more than 2 orders of magnitude improvement in field intensity for a fixed electromagnet drive current. This allows much 'thinner' optics for a given deflection angle. The deflection of a charged particle beam by a simple normalized dipole field is shown in Figure 1.3.

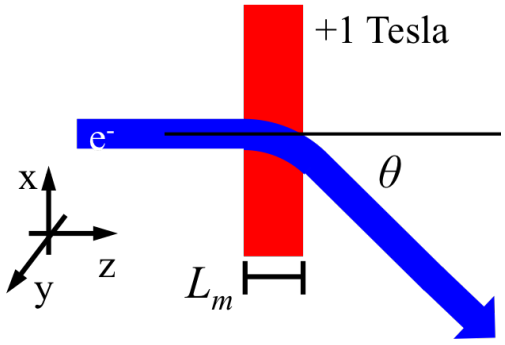

Figure 1.3: Illustration of electron deflection by a normalized dipole field.

Focusing is necessary to transport the beam over a distance without loss or to improve the beam intensity at a point, and is accomplished for high-energy particle beams with quadrupole magnetic fields. A particle beam focused by a quadrupole field can be described using a momentum-normalized focusing strength, $k = qg/p$, where q is the particle charge and g is the field gradient. For a monochromatic particle beam, the focal length transverse to the field gradient is $f^{-1} = kl$, where l is the effective magnetic length of the quadrupole, or the normalized interaction distance between the particle and the field. The field gradient in a small-gap quadrupole with a high-permeability yoke can be approximated as $g = 2\mu nI/r^2$. Reducing a cm-scale gap in a set of quadrupole beam optics to sub-mm-size leads to more than 4 orders of magnitude improvement in field gradient for a fixed electromagnet drive current, and can enable record-setting focusing performance.

Lorentz forces in a quadrupole field imply that particles distributed on one transverse axis focus while particles distributed on an orthogonal transverse axis defocus. Net focusing then requires 2 or more quadrupoles rotated 90° to each other. The reduction in size-scale and improvement in field gradient enables dramatic reductions in the size and overhead of a particle-beam focusing lattice. The focusing of a charged particle beam by a simple normalized quadrupole field is shown in Figure 1.4.

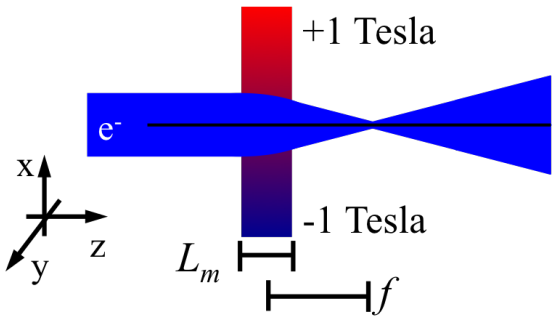

Figure 1.4: Illustration of electron focusing by a normalized quadrupole field'.

For both dipole and quadrupole fields, the strength of a multi-pole electromagnet is related inversely to the distance between the pole tips, while material parameters such as the yoke's magnetic saturation or the maximum current density of the electromagnet windings is not directly affected by scaling. Additionally, smaller electromagnet gaps reduce the to-

tal magnetic flux necessary for a given field. This is reflected in the electromagnet design as a reduced number of turns, lowering the resistance, inductance, $\int_A \vec{B}/I = L$, and the RLC circuit time constant. A circuit time constant shorter than the time between electron pulses allows short-duty-cycle pulsing of the electromagnets, enabling dynamic pulse-to-pulse reconfiguration of the electromagnet array while reducing system power consumption and relaxing thermal design constraints. As a result, scaling down from traditional centimeter-scale out-of-vacuum magnetic optics to sub-mm-scale in-vacuum surface-micromachined magnetic optics provides a clear path for improvements in steering, focusing, and chromatic correction while dramatically reducing the size, weight, and power consumption of a particle-beam transport system.

1.3 Undulator scaling

Undulator and wiggler magnets producing a periodic magnetic field play a key role in the development of modern x-ray sources. As electrons move through the periodic undulator magnetic field, photons are emitted at a central wavelength

$$\lambda_r \cong \frac{\lambda_u(1 + K^2/2)}{2\gamma^2} \tag{1.1}$$

with radiated power of

$$P_T = \frac{N}{6} Z_0 e I \frac{2\pi c}{\lambda_u} \gamma^2 K^2 \tag{1.2}$$

where λ_u is the undulator period, K is the normalized root-mean-square (rms) undulator vector potential, γ is the relativistic Lorentz factor, N is the number of periods, and Z_0 is the impedance of free space (377 Ω), e is the electron charge, and I is the beam current. Reducing the length-scale of an undulator blue-shifts the radiated light for a given set of electron parameters. Figure 1.5 illustrates an undulator light source.

The normalized undulator parameter, K, describes the transverse deflection imparted onto the traveling electron. The undulator parameter plays a prominent role in the phase matching condition for undulator radiation and its deflection strength determines the number

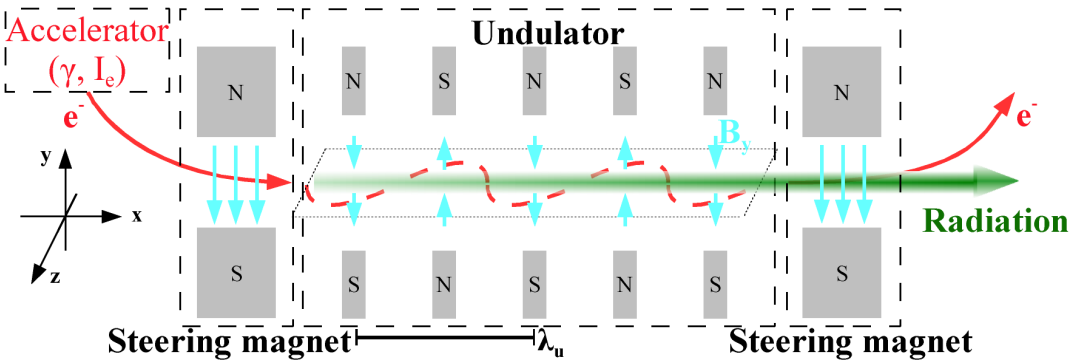

Figure 1.5: Illustration of an undulator light source. Blue shows the electron beam path (deflected in the z-direction inside the undulator), cyan shows the magnetic field direction (oriented in the y-axis), and green shows the radiation intensity and direction. The characteristic length of the periodic field is defined as λ_u.

of photons emitted each period, making it a common metric for comparing undulators. It is defined by

$$K = \frac{eB_0\lambda_u}{2\pi m_e c} \tag{1.3}$$

where e is electron charge, B_0 is transverse magnetic field, m_e is electron mass, and c is the speed of light.

The radiation produced by one electron acts on other electrons, introducing an interaction [Pel01] between the two. As a result, the beam evolves toward a distribution with the electrons regularly spaced within the beam at a distance of the undulator radiation wavelength. As electrons bunch in regular intervals, a larger electromagnetic field is formed that results in increased energy exchange and bunching. This process, called the Free Electron Laser (FEL) instability, results in an exponential gain in radiation field amplitude, saturating when the number of electrons radiating coherently becomes on the order of number of electrons in the beam. The instability growth rate for an ideal 1-D system, called the gain length, is

$$L_g = \frac{\lambda_u}{4\pi\rho} \tag{1.4}$$

where the Pierce parameter, ρ, is

$$\rho = \left(\frac{K\lambda_u\Omega_p}{8\pi c\gamma}\right)^{1/3} \tag{1.5}$$

and Ω_p is the relativistic plasma frequency. For an undulator with many gain lengths of distance, the intensity grows as

$$I \sim \frac{I_0}{9} e^{z/L_g}. \tag{1.6}$$

Conventional undulator technology uses permanent magnet and high-permability-yoke or superconducting electromagnetic undulators with period $\lambda_u > 1$ mm. To access the $\lambda_r = 1$ nm x-ray region of the electromagnetic spectrum with these period lengths, a minimum beam energy of 500 MeV ($\gamma \sim 1000$) is required. Modern radio-frequency (RF)-accelerator gradients still remain below 20 MV/m, requiring at at least 25 m of linear accelerator for a 500 MeV beam. This component drives the size and cost of high energy beam systems, often requiring national-scale facilities to house them. If a beam of sufficiently high quality or phase space density is transported through a long undulator, the free-electron laser instability develops causing coherent radiation generation with exponential optical gain [BPN84].

These linear accelerator FEL light sources, known today as 4^{th} generation light sources, are the most intense sources of coherent light ever made, and under great demand for scientific experiments, drug discovery, and medical imaging. Undulators with period range between 100 μm and 1 mm would enable access to this region of the electromagnetic spectrum with medium energy (<100 MeV) electron beams. These microundulators could take advantage of the continuous progress in the generation of high brightness electron beams and would constitute an attractive solution for lowering the energy requirements of electron accelerators for next generation FEL-based x-ray sources, dramatically reducing cost [BPN84]. At the same time, microundulators would also constitute a valid alternative to inverse Compton scattering [SLC96] sources, as short wiggling periods and long interaction lengths could be obtained without the use of high power laser systems. Figure 1.6 compares the wavelengths and light intensity accessible by several light source technologies, highlighting the application space that MEMS microundulators and focusing optics are intended for.

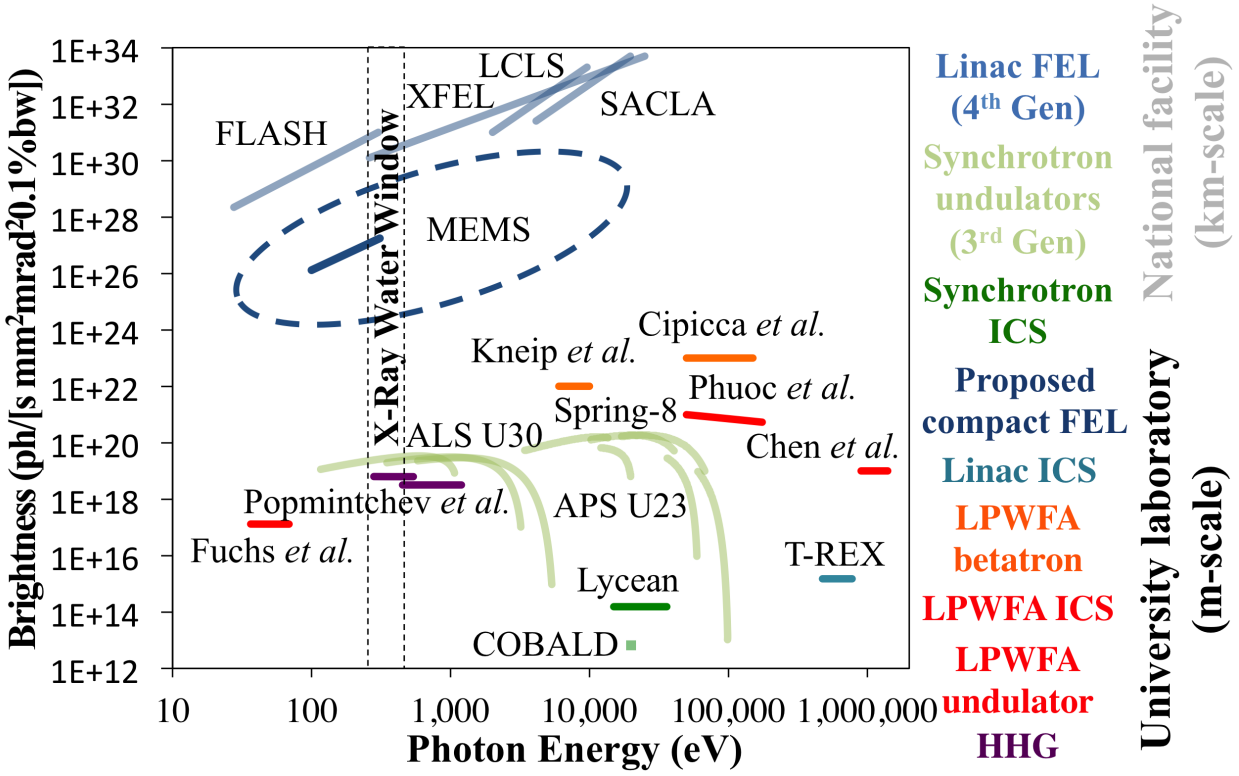

Figure 1.6: Peak brightness vs. photon energy for existing light sources, both m-scale and km-scale [Lab14, Ins14, Cen14, Ele14b, Ele14a, OS12, FWP09, KMM10, CIE11, AAG11, PLP10, ABS13, PCT12, CPG13, CAP10, PCP12]. Brightness is reported in the standard convention of photons/second normalized to 1 mm^2 surface area and 1 mrad^2 solid angle. Between the national-scale 4^{th} generation light sources and the 3^{rd} generation and compact light sources is a technological gap, limited by the lack of high-performance short-period undulators. The solid blue line shows the calculated power output power of a compact soft X-Ray free electron laser operating in the Raman regime with a micro-undulator.

CHAPTER 2

Prior art

THERE have been continuous improvements in magnetic optics and undulators as the underlying physics have been explored and as materials and manufacturing precision has improved. Steering magnets, focusing optics, and undulators have all seen several orders of magnitude improvement in strength and operating frequency, enabling several new generations of beam systems at each new performance level.

2.1 Steering magnets

Steering magnets for particle beam systems can be generalized into three groups: slow magnets used for constant beam deflection, fast (kHz) sweeping magnets for beam steering in electron and ion beam microscopy, and very fast pulse (μs) 'kicker' magnets at slow repetition rates (Hz) for injecting and extracting beam pulses from circulation in synchrotron storage rings. Figure 2.1 shows an assortment of commercially available slow steering magnets, Figure 2.2 compares an assortment of fast sweeping magnets, and Figure 2.3 shows an assortment of kicker magnets.

While miniaturization has clear performance benefits for operating frequency and dipole field intensity, the deflection angle of a steering magnet, $\theta = qBL_{\mathrm{m}}/p$ is also dependent on L_{m}, the normalized distance the charged particles travel through the magnetic field. MEMS manufacturing places upper limits on the size of individual devices due to limitations on aspect ratio during patterning and material deposition, preventing the scaling of the electromagnet gap while maintaining the interaction length. These limitations makes MEMS steering electromagnets promising for fast sweeping stages, short period undulators, or kick-

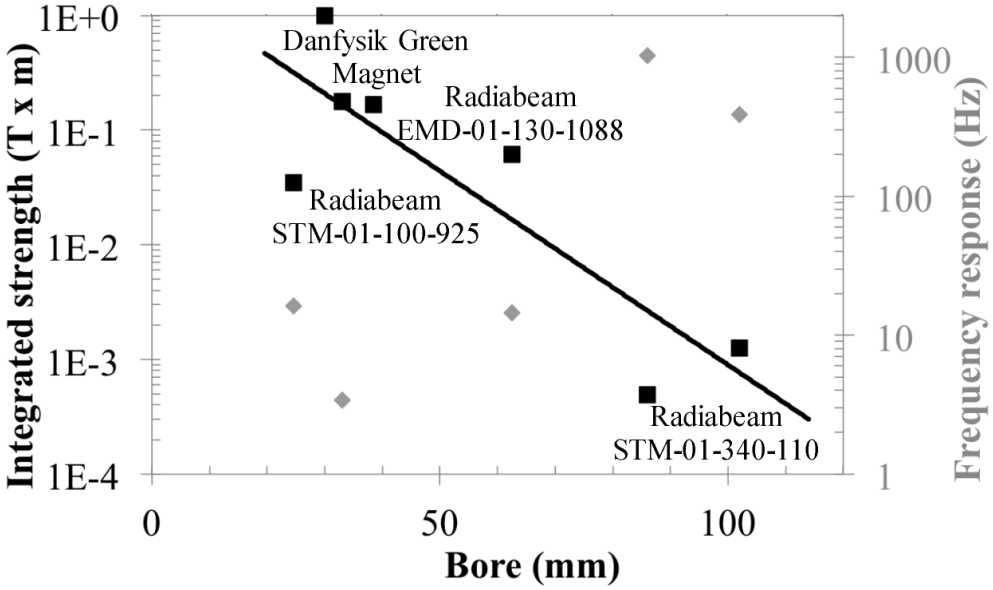

Figure 2.1: Integrated deflection strength ($B \times L_m$) and maximum frequency response vs magnet bore for several commercial slow deflection electromagnets [Tec14d, Tec14e, Tec14a, Tec14b, Tec14c, Dan14b]. Black shows the integrated deflection strength and gray shows the fastest operating frequency.

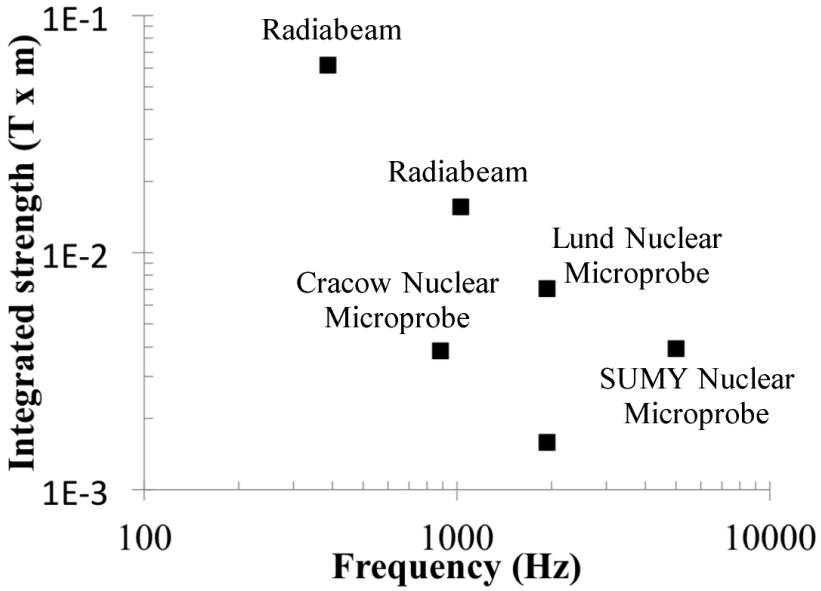

Figure 2.2: Integrated deflection strength ($B \times L_m$) vs. sweep frequency for several beam sweeping electromagnets [Tec14d, Tec14e, DKG03, LSC01, Leb99, LCC99, TLK87, SPD07, BVS01, BKJ01].

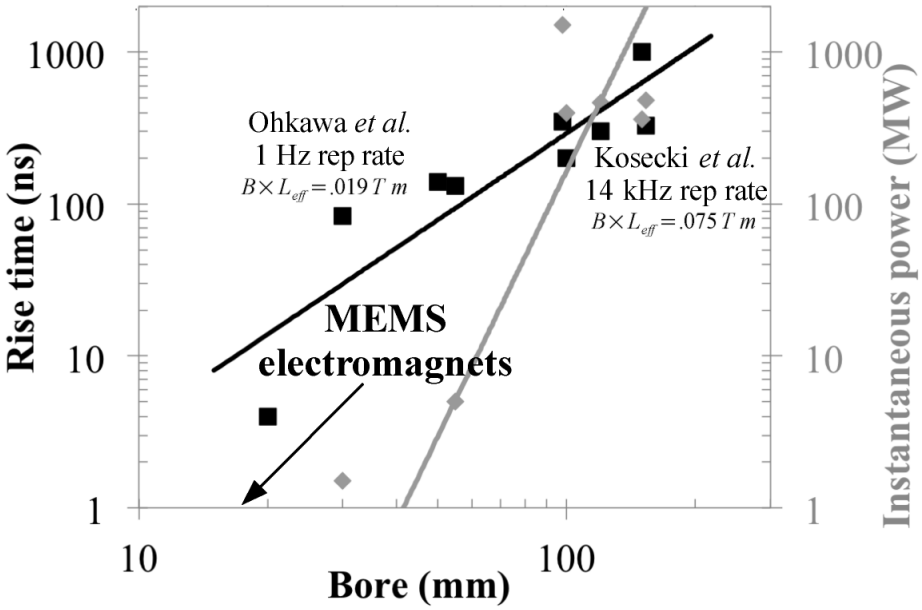

Figure 2.3: Magnet pulse rise time and power draw vs. magnetic gap for several 'kicker' electromagnets [NTY11, GPR97, ZSH04, AAB09, OCW05, OCW02, BCD07, ELM03, ADD05, YOG08, Nak09, FMS12, KTK06, KM14, Dan14c, Lee12]. Black shows the rise time of the magnetic pulse and gray shows the power draw during the pulse. The repititon rate and integrated deflection strength ($B \times L_m$) of some example kickers are annotated on the plot.

ers for compact low-energy storage rings, but limits their use for constant deflection magnets or kicker electromagnets in high-energy synchrotron storage rings.

2.2 Focusing magnets

Improvements of quadrupole focusing optics has centered on integrated strength, field quality, and tuneability, depending on the needs of the application. Improvements in integrated focusing strength have focused on reducing the electromagnet gap, using permanent magnets, or using very high electromagnet drive currents. Permanent magnet quadrupoles lack tuneability, but can produce very high field gradients in a small gap without power consumption. Lim *et al*. used this strategy to demonstrate a 5-mm bore Halbach configured permanent magnet quadrupole producing 560 T/m for high-intensity inverse Compton scattering experiments [LFT05]. Very high electromagnet drive currents in a macro-scale quadrupole electromagnet requires specialized electromagnet geometries to reduce inductance and also requires

high-voltage energy-storage systems to provide power for the pulse, but can produce very high gradients. Winkler *et al*. demonstrated this with a 1-Hz 20-kA pulsed quadrupole electromagnet that produced 1400-T/m gradient across a 20-mm gap [WCB03]. Improvements in field quality have relied on electromagnets with very precisely machined magnetic pole tips. Rebrov *et al*. demonstrated a quadrupole electromagnet producing 650-T/m gradients across a 13-mm gap with less than 0.1% higher order multipole field components [RPP07] using precision electrical-discharge machining tools. Improvements in tuneability have relied on secondary coils used to tune other multi-pole components of the field. Volk *et al*., for example, used field shimming coils to provide 6-T/m of tuneability to a 36-T/m gradient permanent magnet quadrupole [Spe01]. Each of these performance metrics can improve directly with miniaturization and MEMS fabrication technologies. Figure 2.4 compares a variety of quadrupole focusing electromagnets.

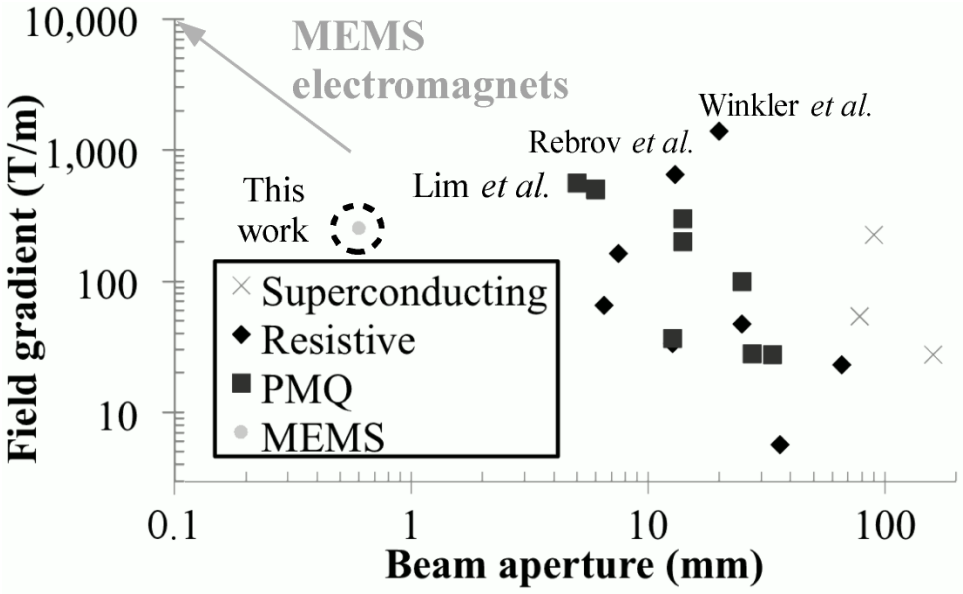

Figure 2.4: Quadrupole field gradient vs. beam aperture for several resistive, superconducting, and permanent magnet quadrupoles used in operating beamlines [Spe01, Dan14a, WCB03, TOO01, LHR98, KAC09, CDF09, KAK12, BGL99, RPP07, WFP11, ZCK13, MIK04b, LFT05, MLM12, MIK04a, TPC12, SPR07]. The gray line denotes the projected performance of optimized MEMS quadrupole electromagnets.

2.3 Undulators

Macro-scale undulators have been well established since Hanz Motz used an undulator and an electron beam to produce the first man-made coherent infrared light [MTW53]. Since then, national-scale user facilities have been set up in many developed countries, providing access to a variety of difficult to reach wavelengths. Undulators in synchrotron facilities such as SPRING-8 in Japan, BESSY in Germany, and the Advanced Light Source and Advanced Photon Source in the United States produce light from deep ultraviolet to hard X-rays. Undulators at the end of ultra-bright linear accelerators are known as 4^{th} generation light sources, and produce ultra-bright coherent beams of VUV to hard X-rays at facilities such as the Linac Coherent Light Source in the United States, SACLA in Japan, and the European XFEL in Germany. Most of these undulators utilize permanent magnets, but some electromagnetic [KBH98] and superconducting undulators [HKM98] are also in service.

Undulator designs with period lengths in the mm to sub-mm range have been pursued to reduce the size and cost of high-energy light sources since the mid-1980's. V. Granatstein proposed a design for mm-scale pulsed electromagnetic undulators [GDM85]. G. Ramian proposed using periodic grooves ground into samarium cobalt blocks to produce a mm-scale undulating field [REK86]. K.P. Paulson built and characterized this undulator design, demonstrating that machined permanent magnets could be used to reduce the period length to 4 mm. His work noted the unsolved drawbacks inherent in small machined permanent magnets of smaller magnetic fields, continuous offset and long-period field errors, and large end fields [Pau90]. Paulson proposed integrated electromagnets and magnetic end-caps as potential solutions, but this was not pursued further at the time due to the expected manufacturing complexities. Tatchyn *et al.* proposed and fabricated hybrid-bias-permanent-magnet undulators with period lengths in the range of λ_u = 700 - 800 μm. Magnetic testing of these 'micropole' undulators showed magnetic fields as high as 0.38 T [TC87]. These undulators demonstrated 1 pW of 66-eV soft x-ray/VUV radiation from a 70-MeV 1-nA linear accelerator at Lawrence Livermore National Laboratory [TTH89]. The magnetic field in these devices was limited by the low remnant field of the NdFeB permanent magnets (0.73 T) and

by the 200+ μm gap, which still was not wide enough to fully accommodate the electron beam available at the time. Electron beam size, positioning, and stability were identified as primary limitations on further developing the technology. Another limitation was identified in the transverse and longitudinal disturbances to the electron beam energy by wakefields within the undulator [TCT89]. In subsequent years, the emittance and stability of electron beams have improved by orders of magnitude [DBD09].

Since these early efforts, the range of undulator period lengths between 10 μm and 700 μm has remained inaccessible. Laser undulators at these wavelengths are limited by a lack of high intensity gain media. Permanent magnets, on the other hand, are limited by crystal grain and magnetic domain size limits [AW09]. Machining technology does not exist to manufacture superconducting undulators with sub-mm period, and the only other feasible alternative, 'slow light' cavity undulators, have yet to be experimentally demonstrated [PBM09]. Figure 2.5 compares the performance of several demonstrated undulators.

Recent progress on surface-micromachined magnetic materials [GHN10, OTH98] and devices [OHC06, GTH09, GTH11] has enabled soft-magnet inductors and actuators to be fabricated by photolithography and electroforming with precision on the range of a few μm in the lateral dimensions and film thicknesses in excess of 50 μm. These surface-micromachined inductors are the predecessors to this work.

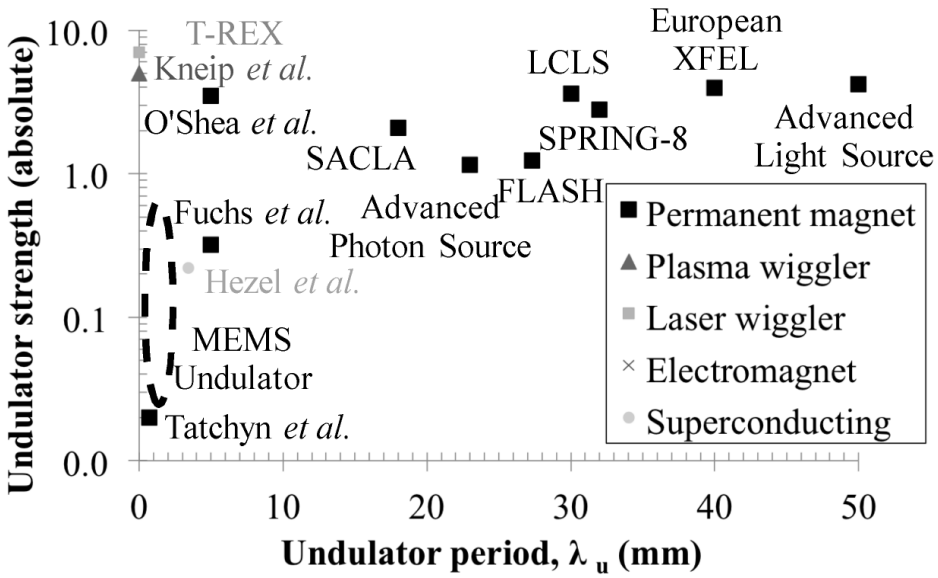

Figure 2.5: Undulator strength vs. undulator period for several research undulators and operating light source undulators. Annotations identify the undulators by facility or author, and the black circle indicates the range of parameters targeted for MEMS undulators. The inverse Compton scattering light source Thompson-Radiated Extreme X-Ray (T-REX) [GAA10] and plasma betatron light source Kneip *et al.* [KMM10] driven by Terawatt sub-micron wavelength laser facilities are included for reference. The T-REX light source is optimized for the production of gamma rays, however, and plasma betatron light sources cannot produce monochromatic light.

CHAPTER 3

Design

HIGH-PERFORMANCE and manufacturable designs for MEMS-based electromagnet systems require a combination of analytical and computational modeling at the device and system level. Guided by the scaling laws for these devices and the process constraints discovered during manufacturing, quadrupole and undulator electromagnets were modeled as magnetic circuits, optimized using 3-D finite element method (FEM) simulations, and the resulting parameters were used in 3-D physics simulations modeling a MEMS-based light source.

3.1 Electromagnets

Soft-magnet electromagnets require an actively powered coil producing magneto-motive-force (MMF) to generate magnetic flux, a magnetic yoke to direct the flux across a free-space gap, and engineered magnetic pole tips to concentrate the magnetic flux density. The maximum field that can be generated is limited by the saturation magnetization of the magnetic yoke, which is as high as 1.1 T for electroplated alloys of NiFe [GHN10] and 2.1 T for electroplated alloys of CoNiFe [OTH98]. Other limitations on peak free-space field result from the lost magnetic flux that fringes across the yoke before reaching the undulator or quadrupole magnetic gap. Peak flux densities in these devices may range from 10 mT to over 1 T in the gap, depending on the design. The pole separation for quadrupoles and period length for undulators is limited at a lower bound by the resolution of the thick photoresist mold that is used in the magnetic yoke fabrication process, typically ~ 10 μm, and at an upper bound by wafer bow due to the volume of deposited material, typically ~ 0.1 mm^3 of permalloy and

copper for a 9 mm^2 silicon die. Overall device size is limited by the size of the silicon wafer used in fabrication, typically 100 mm in a university cleanroom and 300 mm in a commercial cleanroom.

Several obstacles have prevented soft-magnet MEMS devices from achieving widespread use. The complex fabrication process required to produce integrated 3-D coils has limited most previous devices to less efficient planar coils or external magnetic flux sources, two options that would prevent the scaling of microfabricated undulator period length and quadrupole gap diameter to the sub-mm level. Depositing high-quality ferromagnetic films thicker than 10 μm requires expertise in electrochemistry and controlled atmosphere tools [GHN10], a significant barrier to entry in the field. Additionally, microfabrication requires an assortment of cleanroom fabrication tools and a complicated skill set for the tool operator. Thick magnetic film devices, in particular, use atypical processes such as thick photoresist electroplating molds and photolithography over high aspect-ratio topology.

The electromagnet geometry is primarily limited by two effects during manufacturing, diffraction and uneven absorption during photolithography and high internal stress in the photoresist electroplating molds. The diffraction limited critical dimension for photolithography, where adjacent lines and spaces follow precisely from the mask pattern, is expressed by

$$b_{\text{crit}} = \frac{3}{2}\sqrt{\frac{\lambda_l z}{2}} \tag{3.1}$$

where b_{crit} is the feature width that can be precisely resolved, λ_l is the wavelength of the photolithography light source, and z is the thickness of the photoresist [Mad02]. For the 100 μm thick photoresist electroplating mold proposed for the electromagnet yoke exposed with an i-line (365 nm) mercury arc-vapor lamp, experimental results confirm the simple estimates based on equation 3.1 and yield a limit between 5 μm and 10 μm for minimum geometry feature size [FWT99]. Thick chemically-amplified photoresists have experimentally demonstrated 7 μm lateral features in 100 μm thick SU-8 10 [FWT99], 15 μm lateral features in 1.5 mm thick SU-8 [CCD10] and 18 μm lateral features in 180 μm thick KMPR [LJ08].

The resolution limitations imposed by internal stress in the photoresist can be significantly coarser than the effects of diffraction and dose absorption in negative-tone thick-film photoresists. For some geometries, the internal stress of the negative-tone photoresist electroplating mold used during fabrication of the yoke and windings will exceed the adhesion strength between the mold and the preceding film. Fabrication test structures have shown electroplating mold failure with negative tone photoresists for length-to-width ratios less than 4 to 1 for 50 μm thick films and 10 to 1 for 25 μm thick films. For example, the limitations for an undulator with a 100 μm yoke width and height are 50 μm spacing between pole tips and 10 μm spacing between windings given the limitation stated above. Positive tone photoresists do not suffer from stress limitations, but are limited in thickness by exposure-induced opacity and do not achieve the vertical sidewall aspect-ratio required to produce magnetic films for uniform field distribution.

3.1.1 Magnetic circuits and geometry

The achievable peak magnetic flux density and uniformity is governed by the geometry of the flux source. Different geometric designs can be analyzed using Hopkinson's/Rowland's magnetic analogy to Ohm's law

$$\phi = \frac{\mathcal{F}}{\mathcal{R}_{\text{total}}} \tag{3.2}$$

where ϕ is the total magnetic flux, $\mathcal{F}$ is the MMF, and $\mathcal{R}_{\text{total}}$ is the total reluctance of all flux paths (Figure 3.1). The reluctance of a flux path is

$$\mathcal{R} = \frac{L}{\mu T W} \tag{3.3}$$

where L is the magnetic flux pathlength, μ is the magnetic permeability, T is the yoke thickness, and W is the yoke width. Reluctances in parallel add like electrical resistors in parallel ($\mathcal{R}_{parallel}^{-1} = \mathcal{R}_1^{-1} + \mathcal{R}_2^{-1}$), while reluctances in series add like resistors in series ($\mathcal{R}_{series} = \mathcal{R}_1 + \mathcal{R}_2$). The total magnetic flux delivered to the undulator gap will be reduced by the fringing flux paths in parallel with the desired flux path in the system. Because there are numerous fringing flux-paths for complicated 3-D geometries, magnetic circuit analysis

is primarily useful as an optimization tool for seeding 3-D the geometric parameters of a finite element model.

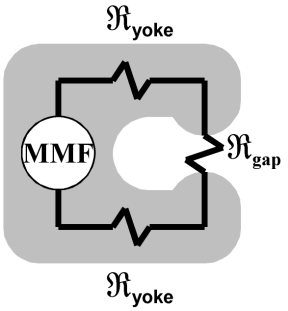

Figure 3.1: Illustration of a magnetic circuit. Gray denotes the ferromagnetic yoke material and the electric circuit symbols denote magnetomotive force source (windings) and magnetic reluctance around the magnetic circuit path.

For a multi-pole electromagnet with a high permeability magnetic yoke, the fraction of generated magnetic flux that is channeled into the gap is a function of the reluctance of the magnetic path across the gap relative to the magnetic reluctance of all other return paths in parallel. Careful design of the flux path is required to minimize the reluctance of the desired path and maximize the reluctance of all other paths.

The 'racetrack' solenoidal coil is an area-efficient design that fits the windings and yoke into a compact solenoidal configuration, ideal for multi-pole electromagnets and short period undulators (Figure 3.2). The solenoidal coil design can fit an order of magnitude or more windings into a given surface area than the simpler and more common planar MEMS coil design.

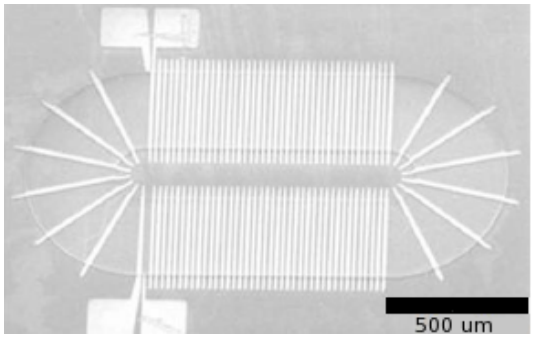

Figure 3.2: Scanning electron micrograph of a surface-micromachined 'racetrack' transformer fabricated at UCLA.

3.2 Multi-pole electromagnets

An electromagnet with an even number of poles can produce dipole fields by energizing poles on one side as 'North' and poles on the other side as 'South'. Figure 3.3 shows one flux path through a 2-pole electromagnet producing a dipole field.

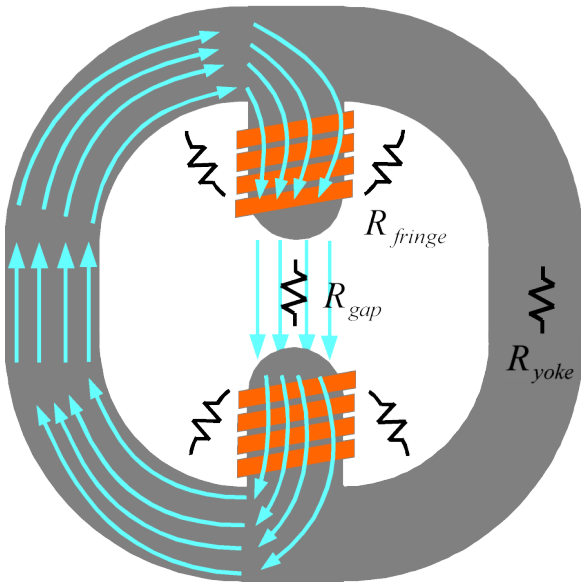

Figure 3.3: Illustration of a 2-pole magnetic circuit. Gray denotes the ferromagnetic yoke material, cyan the magnetic flux lines, and circuit symbols denote the magnetic circuit paths.

An electromagnet with 4-N poles can produce quadrupole fields by energizing the poles in each quadrant with fields in alternating directions. Figure 3.4 shows one set of flux paths through a 4-pole electromagnet producing a quadrupole field.

Dipole, quadrupole, and higher order fields are orthogonal to each other, allowing the linear superposition of fields by adding the electrical current configuration of each electromagnet winding for each desired multi-pole field. A 4-pole electromagnet that can superimpose a dipole field on a quadrupole field is known as a combined-function quadrupole, and can either steer and focus a been simultaneously, or use the dipole field to electrically shift the quadrupole field centroid about the electromagnet gap. Figure 3.5 illustrates the soft-tuning of a MEMS quadrupole field centroid.

Magnetic circuit analysis of several 4-pole electromagnet geometries indicated that the pole tip taper angle most significantly influenced field strength. Figure 3.6 shows a model of

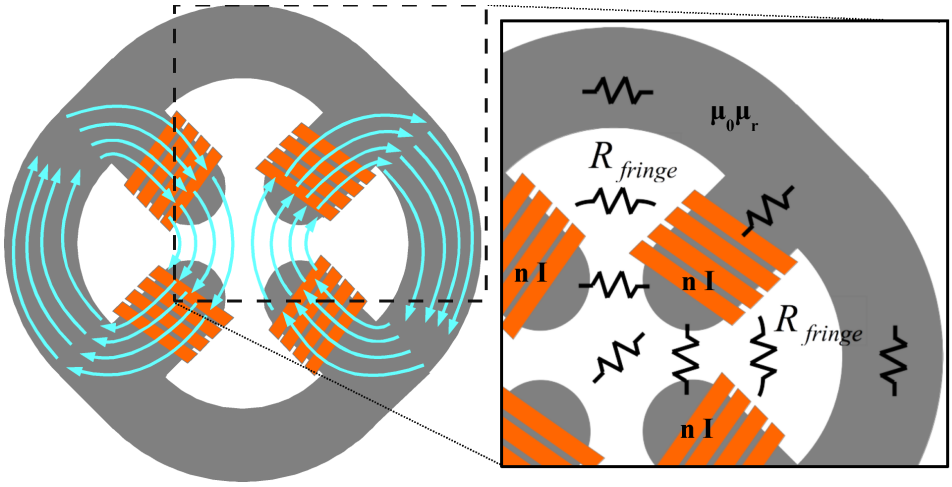

Figure 3.4: Illustration of a 4-pole magnetic circuit. Grey denotes ferromagnetic yoke material, orange denotes the electromagnet windings, and cyan denotes magnetic flux lines. The inset shows the in-plane magnetic circuit parameters.

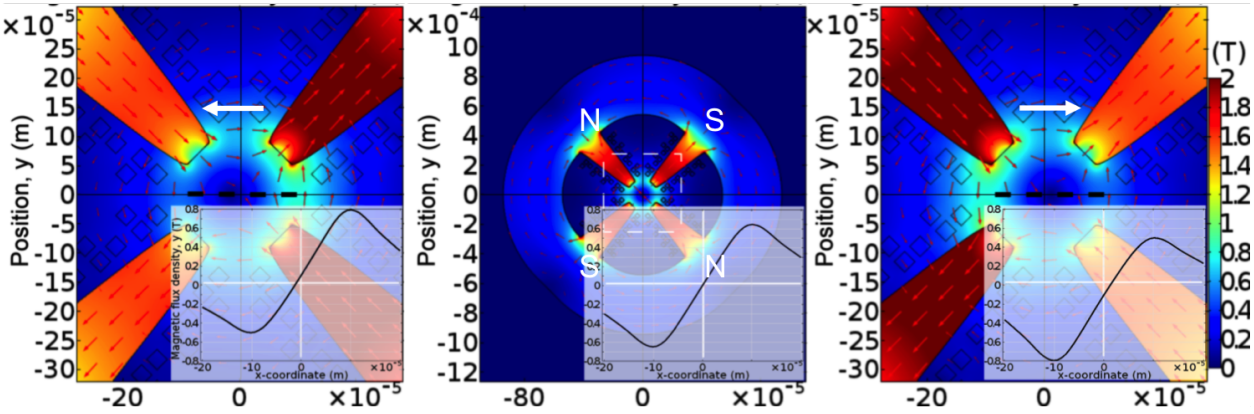

Figure 3.5: Illustration of a combined-function electromagnet electronically shifting the quadrupole field centroid from left to right. The inset shows the transverse y-component of the magnetic flux density across the transverse x-axis of the quadrupole center.

the magnetic flux density along a quadrupole magnet pole of a 600 μm-gap electromagnet for a variety of pole taper angles. Figure 3.6(a) and (b) illustrate the difference in field for the case of an electromagnet with a 10° and 35° pole taper angle.

Table 3.1 shows the result of a parameterized 3-D FEM optimization of quadrupole electromagnet geometry seeded by optimized geometries with a NiFe yoke (B_{sat} = 1.1 T) using magnetic circuit analysis. The quadruple that was actually fabricated and tested is included as the last entry in the table.

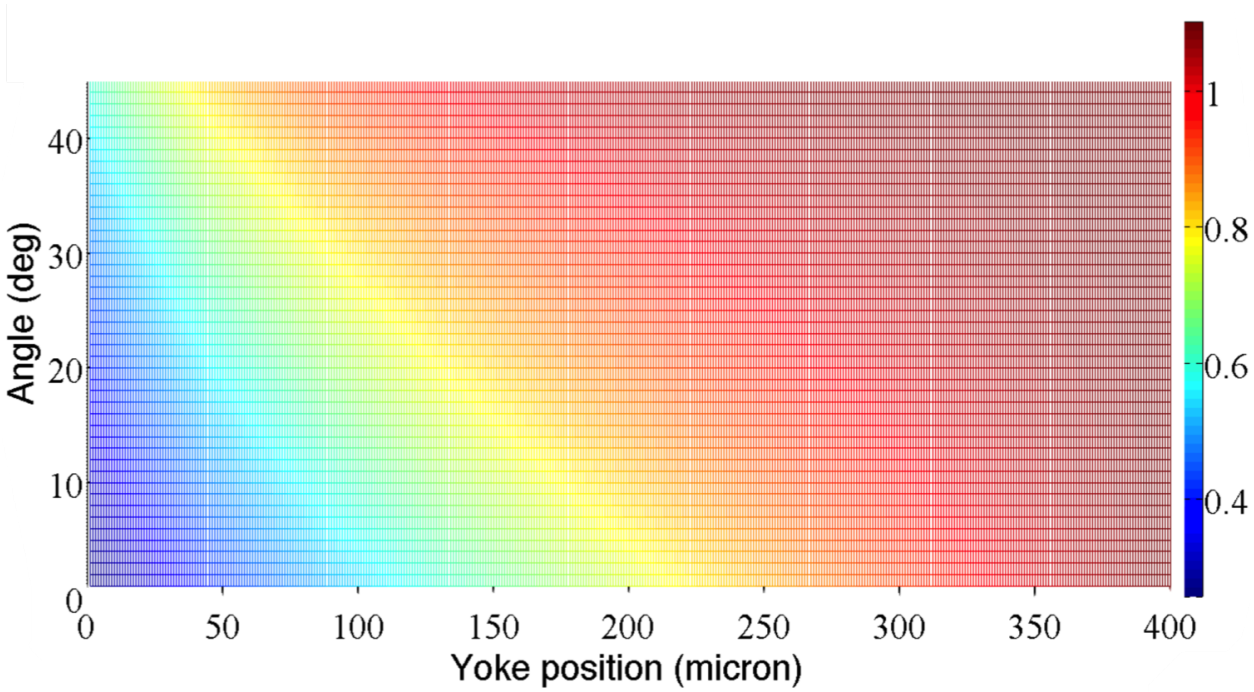

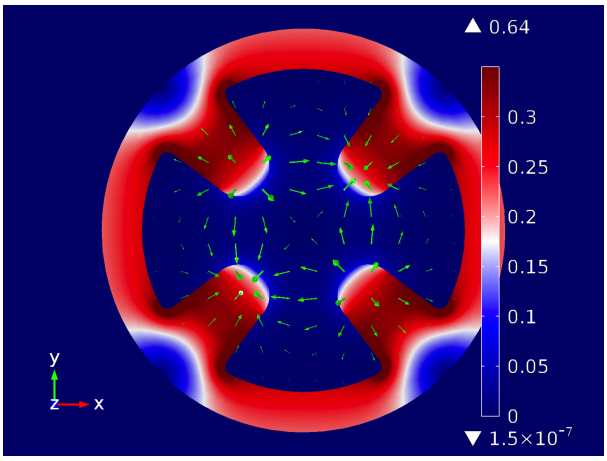

(a) Quadrupole with 10° taper angle

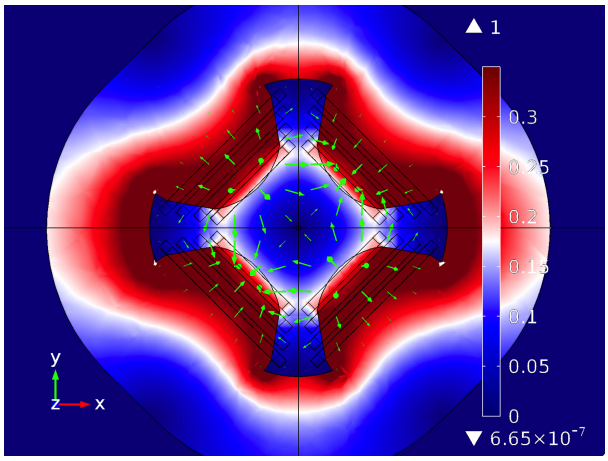

(b) Quadrupole with 35° taper angle

Figure 3.6: Calculated flux density along a quadrupole pole tip vs. pole taper angle.

Table 3.1: Optimized quadrupole geometries. The fabricated quadrupole is **bolded**.

Electromagnet gap (μm)	Winding pitch (μm)	Yoke thickness (μm)	Taper angle (°)	Field gradient (T/m)	Dipole strength (T)
100	45	200	30	10000	0.425
200	45	200	30	6800	0.400
300	65	200	38	3300	0.320
400	75	200	40	2200	0.300
600	100	200	35	1000	0.200
600	**85**	**55**	**10**	**220**	**0.024**

The field produced by -1.0 A in each coil of the fabricated quadrupole electromagnet was simulated using the 3-D magnetostatic simulation package in the finite element method multiphysics software COMSOL. Figure 3.7 shows the simulated dipole field profile and Figure 3.8 shows the simulated field profile for a quadrupole field. The magnetic length was 686 μm for the dipole field simulation and 384 μm for the quadruple field simulation. The inductance calculated by integrating the stored magnetic energy ($E = \int B^2/(2\mu)dv$) matched the measured inductance for the quadrupoles described in Chapter 5 within 6% before packaging and 21% after packaging. Post-packaging measurements were through 20 wire bonds reworked with a chlorine plasma etch, potentially explaining the variation between measurements.

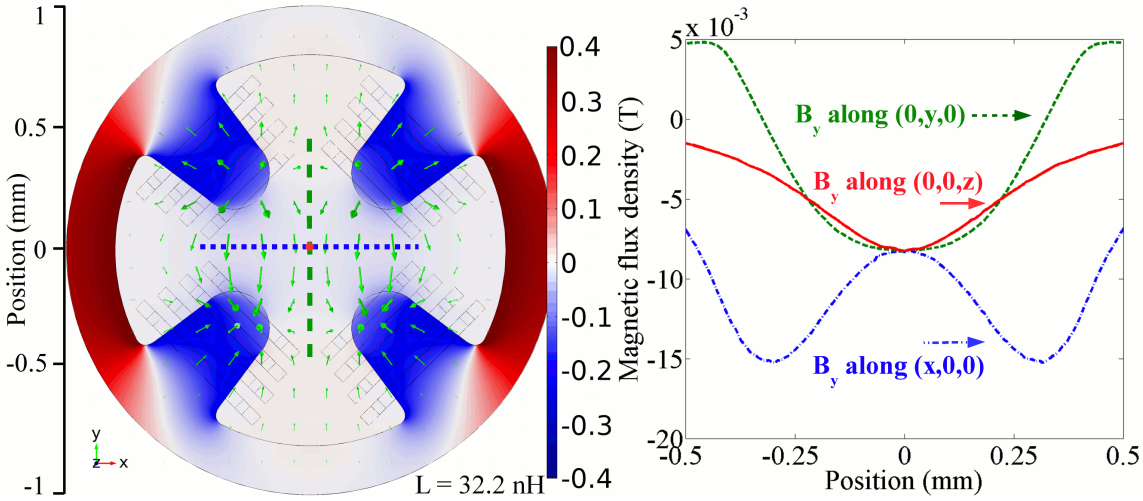

Figure 3.7: Simulated transverse magnetic dipole field profile for I = -1.0-A drive current. Integration across the model volume yields a 32.2-nH inductance. Dividing the z-integrated field by the peak field yields a 686-μm magnetic length, which is the normalized interaction distance of a charged particle.

These simulations show that the yoke for the electromagnet as-fabricated saturates with I = $\pm$2.35-A drive current when producing a dipole field and I = $\pm$4.7 A when producing a quadrupole field while the poles are only 25% saturated with magnetic field. The yoke width in these devices was limited by a 3-mm die size, limiting the maximum field. A 4$\times$ field strength improvement could be realized by simply extending the yoke width without further optimization, however, this design was selected given the fabrication design rules in place at the time.

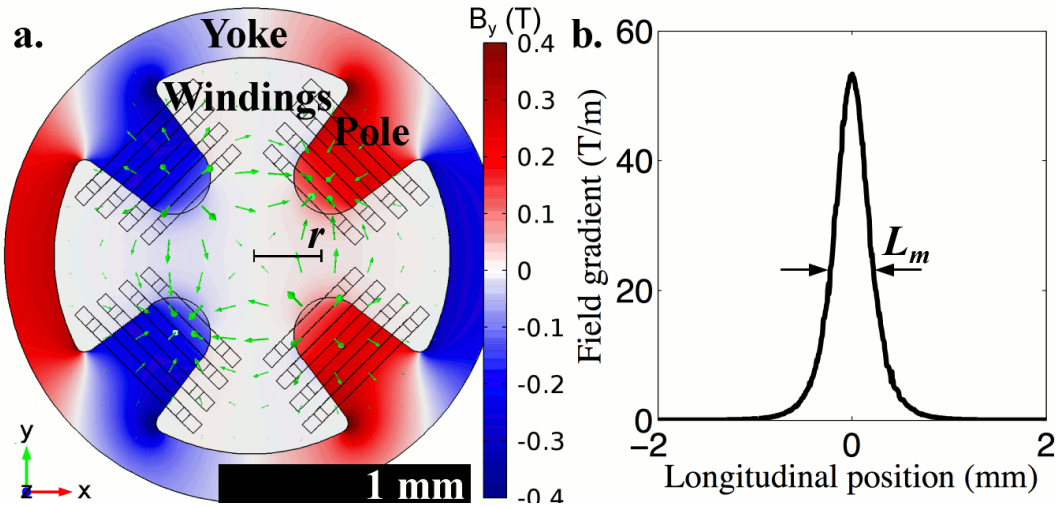

Figure 3.8: (a) Simulated transverse magnetic quadrupole field profile for I = -1.0-A drive current. (b) Dividing the z-integrated field gradient by the peak field yields a 384-μm magnetic length, which is the normalized interaction distance of a charged particle.

3.3 Undulators

The flux path configuration for an undulator allows more flexibility in design. It is possible to generate the magnetic flux on one side of the undulator (Design 1) or on both sides of the undulator axis as in a typical electromagnetic undulator (Design 2) [Cla04], as shown in Figure 3.9. Directing the flux through MMF sources located only on one side of the undulator axis to a short yoke on the other side of a gap (Design 1) allows doubling the yoke width and spacing for a given undulator period length, but at the cost of additional parasitic magnetic fringing between the short yokes. As a result, directing the flux through MMF sources on both sides of the undulator axis (Design 2) achieves a larger peak magnetic field but also a longer minimum period length for a given yoke thickness.

Figure 3.10 shows a reluctance model of the undulator neglecting 3-D fringing and period-to-period fringing. Period-to-period fringing is negligible if the yokes of each period are disconnected. The equations for the total, fringing, and return flux path reluctances can be obtained from Figure 3.10 and are shown below.

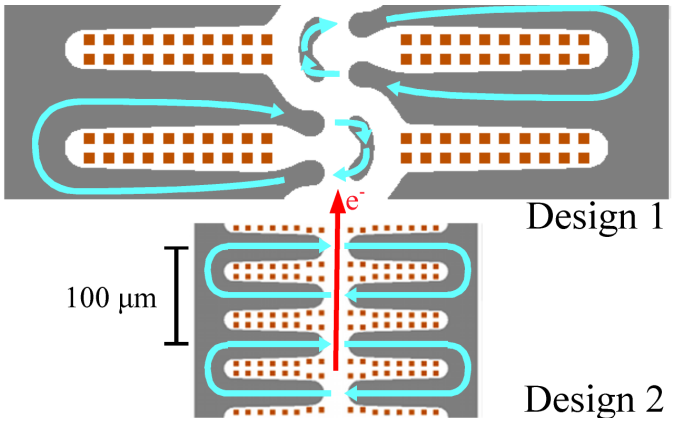

Figure 3.9: Illustration of a two period cross-section of two undulator designs with $\lambda_u = 100$ μm. Undulator design 1 allows further scaling. The magnetic yoke is shown in gray, the solenoid winding interconnect cross-sections are shown in orange, and the intended magnetic flux path is shown in blue.

$$\begin{aligned}
\mathcal{R}_{\text{total}} &= \mathcal{R}_{\text{yoke,f}} + \left(\mathcal{R}_{\text{fringe}}^{-1} + \mathcal{R}_{\text{return}}^{-1}\right)^{-1} \\
\mathcal{R}_{\text{fringe}} &= \left(\mathcal{R}_{\text{window,y}}^{-1} + \mathcal{R}_{\text{window,g}}^{-1}\right)^{-1} \qquad \textbf{Design 1} \\
\mathcal{R}_{\text{return}} &= 2\,\mathcal{R}_{\text{gap}} + \mathcal{R}_{\text{yoke,g}}
\end{aligned}$$

$$\begin{aligned}
\mathcal{R}_{\text{total}} &= \mathcal{R}_{\text{yoke,f}} + \left(\mathcal{R}_{\text{fringe}}^{-1} + \mathcal{R}_{\text{return}}^{-1}\right)^{-1} \\
\mathcal{R}_{\text{fringe}} &= \mathcal{R}_{\text{window}} \qquad \textbf{Design 2} \\
\mathcal{R}_{\text{return}} &= 2\,\mathcal{R}_{\text{gap}} + \left(\mathcal{R}_{\text{yoke}}^{-1} + \mathcal{R}_{\text{window}}^{-1}\right)^{-1}
\end{aligned}$$

Magnetic saturation sets the upper bound for efficient generation of magnetic flux in the undulator yoke. The magnetic flux density in the yoke is

$$B_{\text{yoke}} = \frac{\phi_{\text{total}}}{W_{\text{y}} T_{\text{y}}} \tag{3.4}$$

where W_{y} is the yoke width and T_{y} is the yoke thickness.

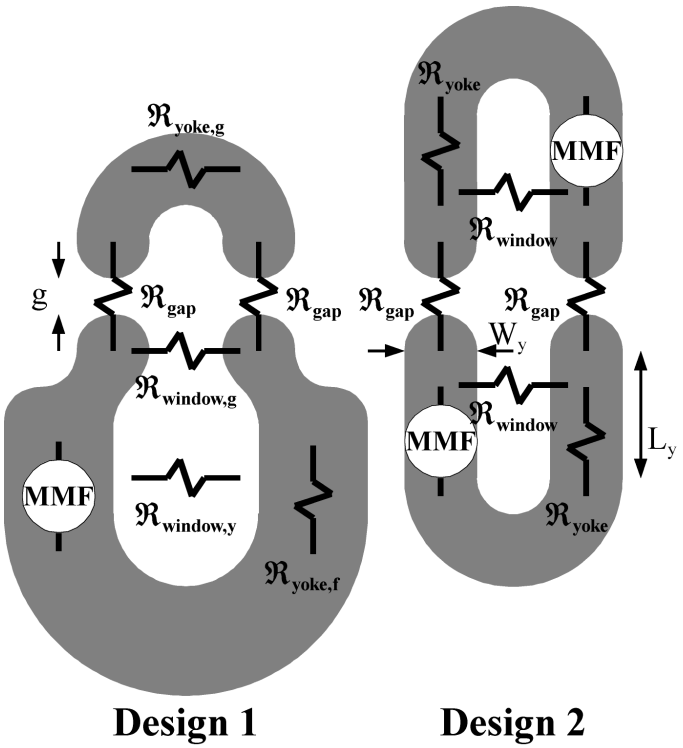

Figure 3.10: Illustration of a simple reluctance model of the two undulator designs illustrated in Figure 3.9.

Magnetic circuit analysis shows that the flux remaining at the magnetic pole tips is

$$\phi_{\text{tip}} = \frac{\phi_{\text{total}}}{1 + \mathcal{R}_{\text{return}}/\mathcal{R}_{\text{fringe}}}. \tag{3.5}$$

To get an analytical estimate of the field, we assume a linear and uniform magnetic material. The magnetic flux at the pole tip and the MMF at saturation can then be found by increasing ϕ_{tip} up to the point where $B_{\text{yoke}} = B_{\text{sat}}$ (2.1 T for CoNiFe).

The transverse magnetic flux density at the center of the undulator is reduced by fringing in the axial direction and can be significantly less than the flux density in the cross section of the yoke. The magnetic field of a standard (Design 2) undulator including 2D fringing was analyzed by Poole *et al*. and is given by

$$B_{\text{peak}} = \frac{\phi_{\text{tip}}}{W_{\text{y}} T_{\text{y}}} \frac{1}{\cosh(\xi)} \left(\frac{1 - \sinh(\xi)/(3\sinh(3\xi))}{1 - \sinh(\xi)/(3\sinh(\xi))} \right) \tag{3.6}$$

where $\xi = \pi g/\lambda_u$ [PW80], g is the gap between pole tips, and λ_u is the undulator period length.

Figure 3.11 shows the magnetic flux density of the undulator (Design 2) plotted at saturation using equations 3.4 and 3.6, varying the undulator period and gap. When all geometric parameters are scaled together, the peak magnetic flux density remains constant. To verify the analytical scaling law, a variety of undulator geometries were simulated using the 2D finite element method (FEM) magnetostatic package in COMSOL Multiphysics with a nonlinear CoNiFe material model derived from vibrating sample magnetometry (VSM) studies of electroplated $Ni_{80}Fe_{20}$ [GHN10] scaled to the saturation magnetization and initial permeability described in Osaka *et al.* [OTH98].

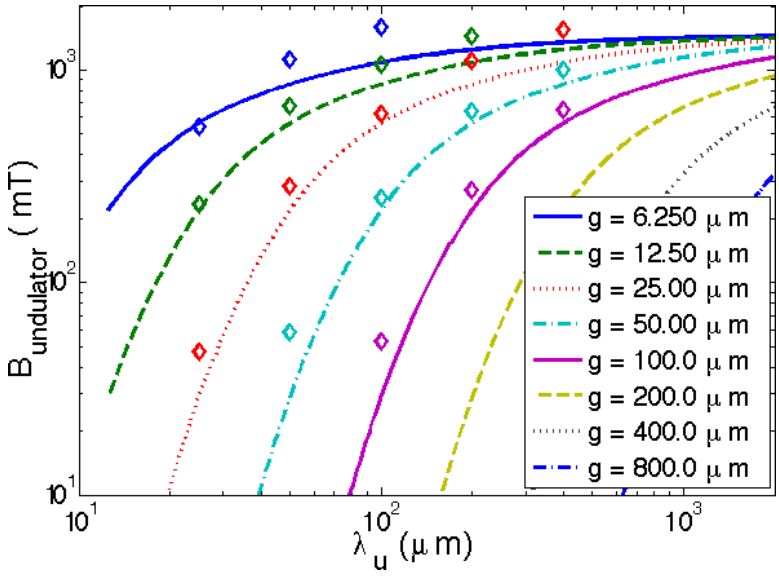

Figure 3.11: Plot showing the scaling of the transverse magnetic flux density in the center of the undulator vs. gap and period. Values of $L_y = \lambda_u/4$, $W_y = \lambda_u/4$ and $B_{sat} = 2.1$ T are used. Lines denote calculations and diamonds denote simulations.

Analytical results approximate the simulated fields well while $1 \leq \lambda_u/g \leq 8$. For large ratios of period to gap, the undulator tip curvature focuses the field and using $\phi_{tip}/W_y T_y$ as the flux density at the tip is inadequate. For small ratios of period to gap, longer fringing paths across the window that were neglected become relevant and $\mathcal{R}_{window}$ is inadequate.

Figure 3.12 shows the MMF in Amp-turn required to generate 1 T for many different ge-

ometries. Peak transduction of electrical current to magnetic field is found across wide bands of period lengths centered at $\lambda_u/g \approx 4$ and is approximately 0.528 A–turn/T/μm $\times$ $\lambda_u[\mu\text{m}]$.

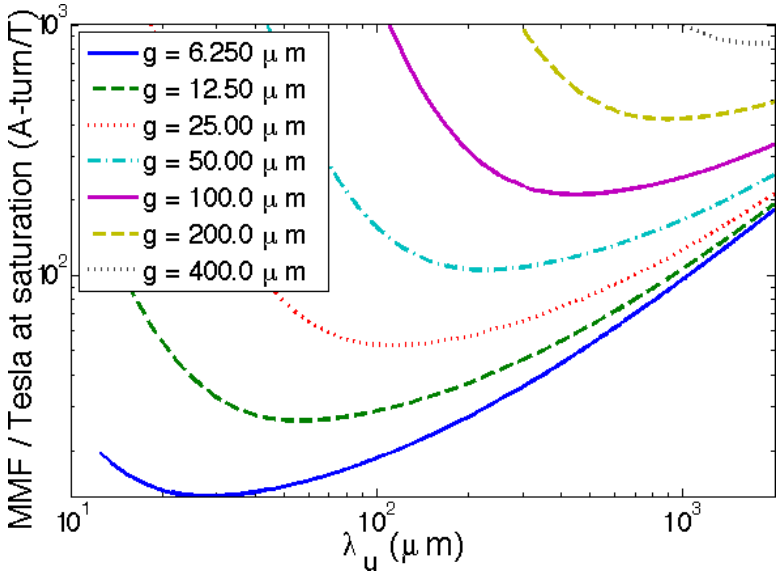

Figure 3.12: Plot showing the ratio of the MMF required to saturate the magnetic yoke, normalized to 1 T, for a variety of undulator geometries.

The maximum MMF that can be generated for each period of the undulator is limited by the maximum allowed current density through the coil before the maximum operating temperature is reached. The maximum operating temperature of the undulator will be reached when either the magnetic material passes the Curie temperature, the internal stress of the magnetic material increases significantly due to annealing, or the polymer used to isolate the windings from the magnetic yoke decomposes. The curie temperature of $Co_{65}Ni_{12}Fe_{23}$ is typically in excess of 800° C [Oma90]. The internal stress of magnetic alloys containing Ni and Fe anneal to high stress in excess of 250° C and the polymer SU-8 decomposes in vacuum at 280° C, setting a maximum operating temperature of 250° C.

Heat transport from the electromagnet through the substrate is limited by the thermal conductivity of silicon, 65 W/cm^2/°C for a 200-μm-thick substrate. At 10 kW/cm^2, 150 °C of the thermal budget is consumed in a 200-μm-thick Si substrate. The thickness of the bottom and top winding layers can be increased to improve heat transport and reduce Joule heating in the electromagnet using a damascene and through-mold electroplating process, respectively, but the cross section of the vias is limited by the available space between the

magnetic yokes. Figure 3.13 shows the maximum MMF that can be generated for different uniformly scaled geometries dissipating 10 kW/cm^2.

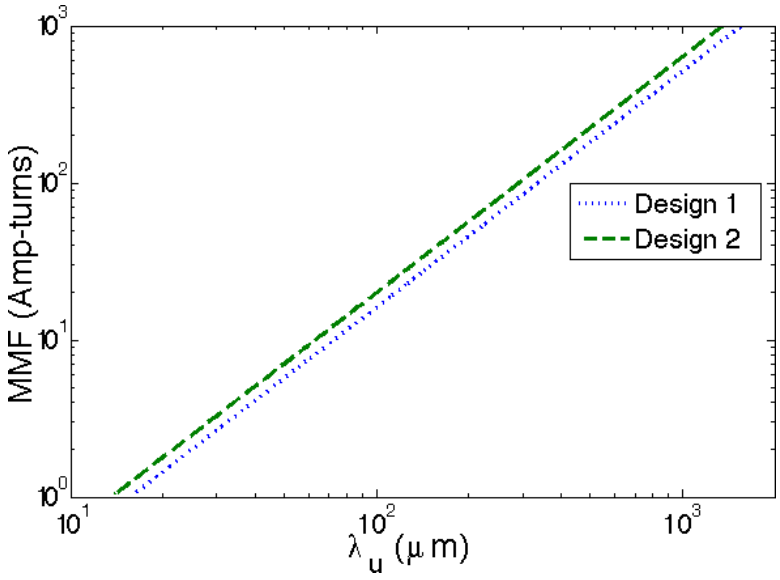

Figure 3.13: Plot showing the maximum MMF that can be generated by a 32-turn coil dissipating 10 kW/cm^2.

As an example, let us consider a λ_u = 100 μm g = 25 μm undulator with a 50 μm thick yoke, saturated with 160 A-turns of MMF. Assuming a 32 turn 0.8 Ω coil, we have J = 2.5$\times$10^{10} A/m^2 winding current density, and each period of the undulator will dissipate 5 W. The base of the 200 μm thick substrate needs to be maintained at a temperature below -143° C to keep the undulator from exceeding 250° C. This undulator should be capable of operation when cryogenically cooled by liquid nitrogen. To improve the thermal performance of the undulator, we can reduce the electromagnet yoke thickness to match the size of the gap between the poles. If a 25 μm thick yoke is used, the base of the substrate must be kept below 41° C and the undulator can operate at room temperature.

The optimal design for the undulator electromagnet is obtained as a compromise between i) reducing the length of the racetrack yoke to minimize the fringing flux losses to reduce the required MMF for a given field and ii) increasing the winding cross-section to reduce the current density and improve heat transport.

3.3.1 Optimization of undulator geometry for higher field

Another design option is to reduce the undulator magnetic gap width below $\lambda_u/4$. This causes the field down the undulator axis to deviate from sinusoidal uniformity, radiating power into higher order harmonics. This deviation can be corrected by shaping the magnetic pole tips. Increasing the radius of curvature of the poles slightly reduces the peak field, but also reduces the contribution of higher order (odd) harmonics in the magnetic field (Figure 3.14). Increasing the radius of curvature from 12.5 μm to 32 μm reduces the third harmonic from 11.5% of the total spectral content to 4.6% and increases the peak of the fundamental harmonic by 7%.

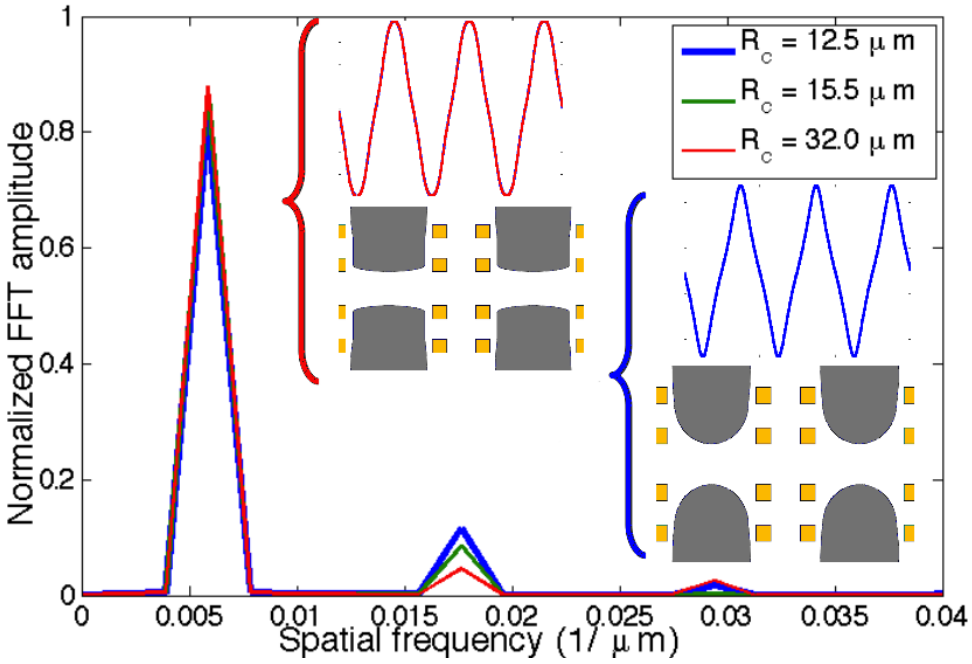

Figure 3.14: Plot of the spatial harmonics of the undulator field in undulator design 2 with λ_u = 100 μm and g = 12.5 μm for several pole tip curvature radii. Data was taken from from 2D magnetostatic FEM simulations.

For periods longer than 100 μm, tapering the yoke from a wide back to a $\lambda_u/4$ width pole reduces the magnetic reluctance (see Figure 3.9) and spreads out the flux at the back corners of the yoke where the undulator first saturates. 2D nonlinear magnetostatic FEM simulations show that a λ_u = 400 μm undulator with yoke tapering and a 50 μm wide magnetic gap produces a saturated peak field of 1500 mT, 45% greater than the un-tapered

yoke. As the undulator period is scaled down, this optimization becomes unfeasible due to the space requirements for the electromagnet winding vias. Table 3.2 lists the peak magnetic flux density simulated for a variety of optimized undulator geometries using a CoNiFe yoke (B_{sat} = 2.1 T).

Table 3.2: Optimized undulator geometries using undulator design 2

λ_u (μm)	Undulator gap (μm)	B_{peak} (mT)	K
25	6.25	540	8.9×10^{-4}
25	12.5	230	3.8×10^{-4}
100	25	727	4.8×10^{-3}
100	50	334	2.2×10^{-3}
400	50	1500	4.0×10^{-2}
400	100	970	2.6×10^{-2}

The strength of the coupling between the radiation and the relativistic beam is related to the normalized undulator parameter, K

$$K = \frac{eB_{\text{peak}}\lambda_u}{2\sqrt{2}\pi m_e c} \tag{3.7}$$

where e is the charge of an electron, B_{peak} is the peak on-axis transverse magnetic field, λ_u is the undulator period, m_e is the electron mass, and c is the speed of light. The achievable undulator parameter in the range of λ_u = 25 μm to λ_u = 1 mm scales between K = 9×10^{-4} and K = 0.1. This is comparable with the shortest period undulators discussed in recent literature, K = 0.03 for a 706 μm hybrid permanent 'micropole' undulator [TTH89], K = 0.4 for a λ_u = 5 mm permanent magnet undulator [EGB07], and K = 0.2 for a λ_u = 3.8 mm superconducting undulator [HKM98].

3.3.2 Undulator sextupole focusing

It is not uncommon for traditional permanent magnet undulators to operate with GeV beams. Scaling the undulator design to the micron-scale eliminates the need for GeV electron sources for X-ray photon energies, and enables more than an order of magnitude increase in photon energy over currently available sources with the same electron accelerator. Shorter undulator scales and lower energy electrons, however, place other demands on the electron

beam characteristics in order to maintain focus and alignment for long distances in sub-100 μm magnetic gaps. The undulator can either rely on upstream beam optics to maintain focus or be designed to achieve a large magnetic spatial gradient in transverse directions, producing a sextuple field to confine the beam.

Relying on upstream beam optics, the length that the electron beam will remain focused is given by

$$L_u \;=\; 2\sigma_0^2\gamma/\epsilon. \tag{3.8}$$

Assuming a normalized transverse beam emittance of $\epsilon = 1$ mm-mrad, a $\sigma = 20$ μm beam width and 120 MeV beam energy, the electron beam will remain focused for a distance of 19 cm, a distance compatible with the length of these microfabricated undulator sections. In order to reach power saturation, many additional stages of focusing optics and undulator segments must be used, or the undulator must be designed to provide natural-focusing in both transverse directions.

Natural-focusing in the out-of-plane transverse direction can be provided by generating an out-of-plane field gradient. This field can be accomplished with additional magnetic material above and below the magnetic pole tips (Figure 3.15).

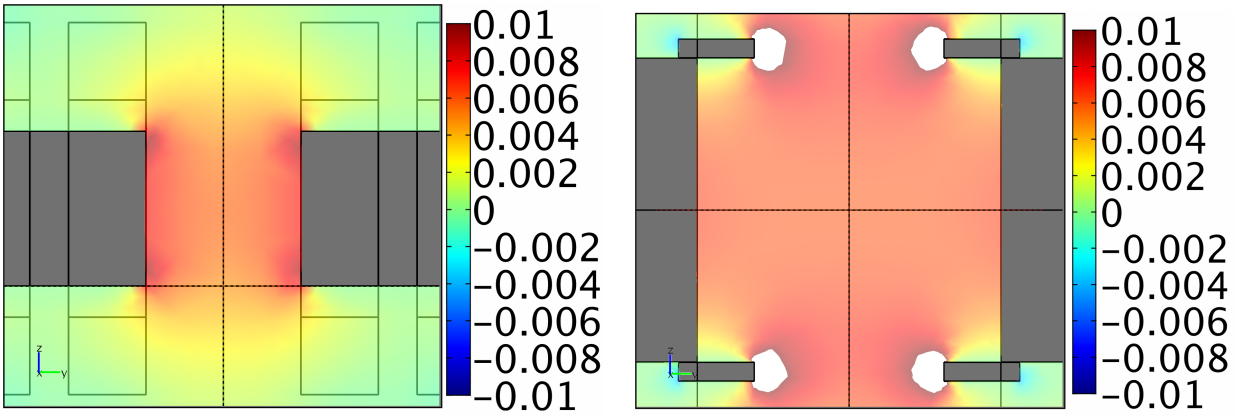

(a) Field intensity without flux lens (b) Field intensity with flux lens

Figure 3.15: Natural focusing sextupole field with additional magnetic material.

The natural focusing strength can be derived from the Lorentz force on an electron moving through the undulator with a field in the transverse y and z directions [HK07]. The natural

focusing strength in the y direction in a flat-pole electromagnetic undulator is defined by

$$k_n = \frac{2\pi K}{\sqrt{2}\lambda_u \gamma} \ll \frac{2\pi}{\lambda_u} \tag{3.9}$$

Typical natural focusing values in a short undulator X-ray FEL, such as a high-gain FEL using a MEMS undulator proposed below (Table 3.4), are $k_n = 1.6\ \mathrm{m}^{-1}$. The natural focusing strength stays constant with scaling of the undulator period, but increases linearly with a reduction in electron beam energy.

Natural focusing can be provided in both directions, as shown in Figure 3.15. The strength in the transverse directions, however, is limited to

$$k_{nx}^2 + k_{ny}^2 = k_{n0}^2 \tag{3.10}$$

providing transverse electron acceleration back toward the undulator center:

$$\frac{d^2 x_{\beta n}}{dz^2} = -k_{nx}^2 x_{\beta n} \tag{3.11}$$

$$\frac{d^2 y_{\beta n}}{dz^2} = -k_{ny}^2 y_{\beta n}. \tag{3.12}$$

Natural focusing in both directions can reduce or eliminate the need for quadrupole focusing optics in some low-energy beam cases, dramatically simplifying the construction of the FEL. Additionally, longitudinal modulation of the electron bunch phase relative to the radiation field, an effect that is detrimental to micro-bunching of the beam, can be avoided with the elimination of the FODO quadrupole focusing lattice [Sch85]. The additional patterned material used to provide focusing in the transverse out-of-plane direction comes at the expense of added fabrication complexity, but has the potential to provide a simpler compact FEL.

3.3.3 Magnetic field uniformity

The low K value of these undulators implies that magnetic field non-uniformity has a relatively small effect on the undulator resonance condition. However, beam position and focusing will be more sensitive to the magnetic field profile because the electron beam occupies much of the space between the magnetic pole tips. 3-D magnetostatic FEM simulations of the field in a 100 μm period, 50 μm $\times$ 50 μm gap undulator were performed with COMSOL Multiphysics to visualize the transverse behavior of the field. Figs. 3.16 and 3.17 show the transverse magnetic flux density at different positions in the undulator.

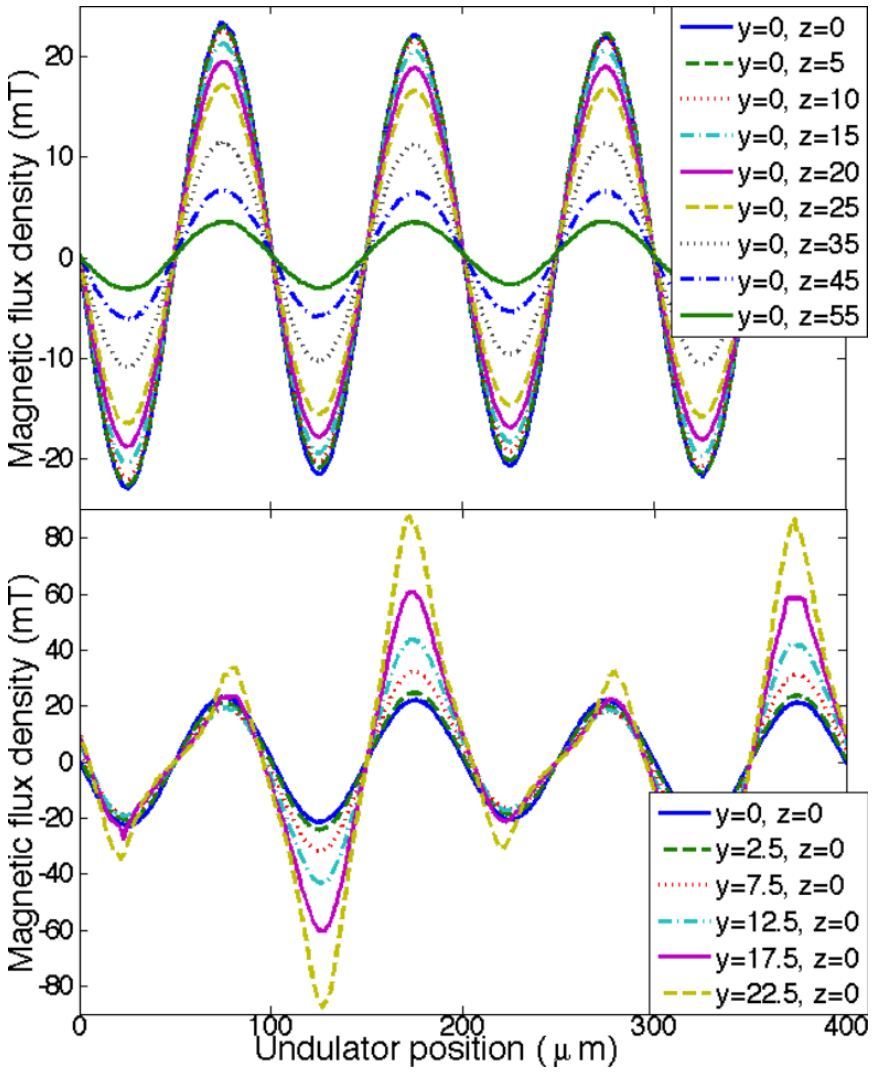

Figure 3.16: Transverse magnetic flux density at different positions for undulator design 1 with λ_u = 100 μm and g = 50 μm driven far below magnetic saturation. The plot spans 5 of 7 periods of an undulator with y = z = 0 μm at the center.

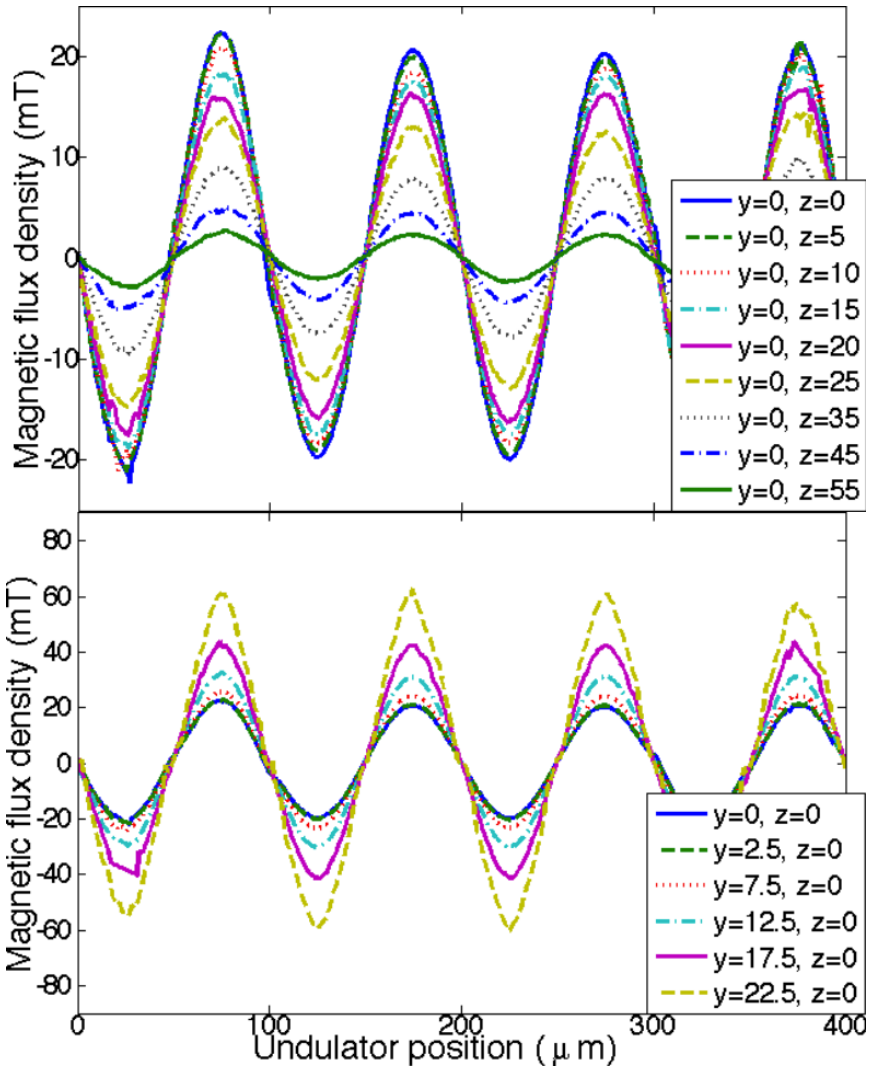

Figure 3.17: Transverse magnetic flux density at different positions for undulator design 2 with $\lambda_u = 100$ μm and g = 50 μm driven far below magnetic saturation. The plot spans 5 of 7 periods of an undulator with y = z = 0 μm at the center.

The z-dependence of the magnetic field seen in both designs is explained by the fact that out-of-plane magnetic fringing reduces the transverse magnetic flux density away from the center of the undulator. Conversely, in the undulator plane (along y-direction), the magnetic flux is larger as we approach the magnetic flux sources. This effect is more pronounced in undulator design 1, where the flux source is only on one side (see Figure 3.17).

In order to estimate the magnitude of the magnetic field errors in this undulator, we observe from equation 3.6 that the on-axis magnetic field varies inversely with the thickness of the yoke. The precise thickness of binary and trinary magnetic alloys is difficult to control

across a patterned feature. A typical random variation in the thickness of the undulator yoke with $\sigma_t = 0.01\ T_y$ corresponds to a $\sigma_{B,t} = 0.01\ B_u$ variation in the undulator field.

Non-uniformity in the photolithography exposure tool dose ($< 1\%$ for modern projection and 1.5% for contact lithography tools) will cause variation in the critical dimensions of the yoke. Using the lumped parameter model for optical lithography [Mac07] and assuming a high-contrast negative-tone photoresist and features that are larger than the critical dimension defined in equation 3.1, a $\sigma_I = 0.01\ \mathrm{I}_0$ variation in exposure dose will result in approximately a $\sigma_{CD} = 0.01\ b_{\mathrm{crit}}$ critical dimension variation. For a 100 μm thick electromagnet yoke electroplating mold, the undulator gap would then vary by $\sigma_g = 60$ nm. A Taylor expansion to first order of terms containing the gap in equation 3.6, $\xi = \pi g/\lambda_u$, at $g/\lambda_u = 1/2$ show that the magnetic field varies with $B_u \propto 1.05 - 0.525\ \xi$. A $\sigma_g = 60$ nm uncorrelated variation in the gap of a $\lambda_u = 100\ \mu$m g = 50 μm and $\lambda_u = 400\ \mu$m g = 100 μm undulator will result in a $\sigma_{B,g} = 0.005\ B_u$ and $\sigma_{B,g} = 0.0004\ B_u$ variation in undulator field, respectively.

The total effect of these uncorrelated transverse field errors on the undulator phase matching condition, defined in equation 1.1, will be limited by the small K of the undulator. A $\sigma_B = 0.011\ B_u$ total variation in the transverse field intensity with K = 0.003 will result in a $1{\times}10^{-7}$ rms error in the phase matching condition of a $\lambda_u = 100\ \mu$m undulator.

Electrically tuning individual undulator electromagnets can mitigate these errors. For undulator design 1, Hopkins analysis neglecting fringing yields a tuning range from $\mathrm{B} = 0$ to $\mathrm{B}_{\mathrm{peak}}$. For undulator design 2, full tuning range can be achieved when the yoke is unconnected between undulator periods. When the yoke reluctance between periods is much less than $\mathcal{R}_{\mathrm{total}}$ and there are many periods, however, tuning range approaches zero.

3.4 Challenges for free electron laser system using MEMS optics

Integrating a microfabricated electromagnetic undulator with a beam line poses several challenges that are not typically encountered with macroscopic permanent magnet, superconducting, or laser undulators. The undulator transverse structure is sub-mm size, and it must

be placed inside the vacuum beam line, complicating alignment, electrical interconnects, heat extraction, and beam focusing. Spatial measurements of the actual magnetic field will be complicated by the small undulator gap. Further, the proximity of the undulator surface to the electron bunch influences the beam characteristics.

3.4.1 Heat dissipation

Heat extraction is a serious challenge when operating electromagnetic undulators under vacuum. Further aggravating heat extraction from the undulator is the reduced cross-section of the windings as the undulator period scales down, driving up both current density and coil resistance. Depending on the geometry, the undulator dissipates 100s of W/cm^2 to 10s of kW/cm^2 during operation (Figure 3.18).

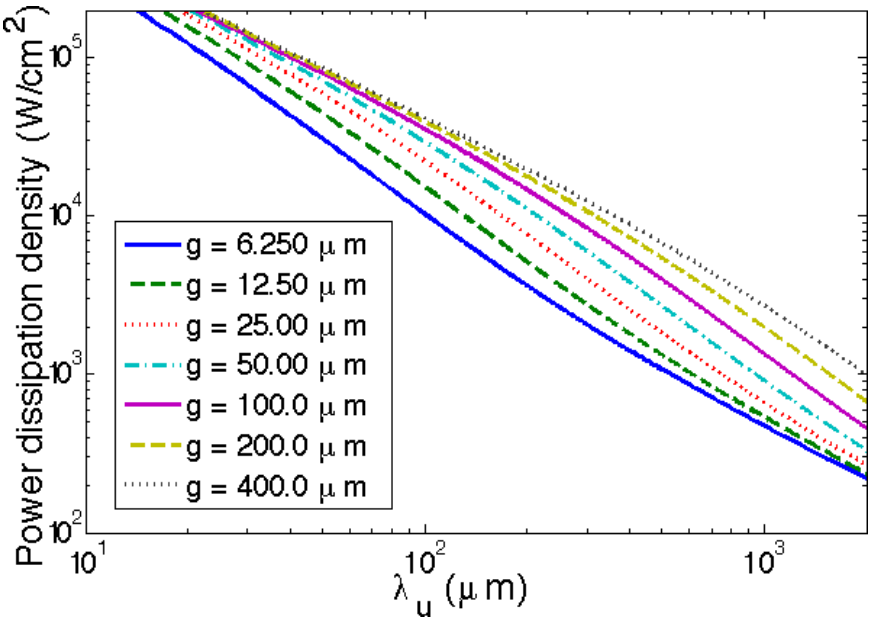

Figure 3.18: Plot showing the scaling of the surface power dissipation density generated by the undulator windings at saturation.

For a saturated 400 μm period undulator with a magnetic gap of 50 μm, 3820 W/cm^2 must be extracted from the undulator to maintain a steady-state temperature. Figure 3.19 shows the 2D temperature distribution simulated using COMSOL Multiphysics across a 50 μm tall winding cross section of a λ_u = 400 μm undulator on a 200 μm thick silicon wafer. Here, the base of the wafer must be held at less than 138° C to keep the structural polymer

from exceeding a safe temperature of 250° C. Figure 3.20 shows the simulated temperature distribution across a 25 μm tall winding cross section of a λ_u = 100 μm undulator on a 200 μm thick silicon wafer. Here, the base of the wafer must be held at less than 32° C.

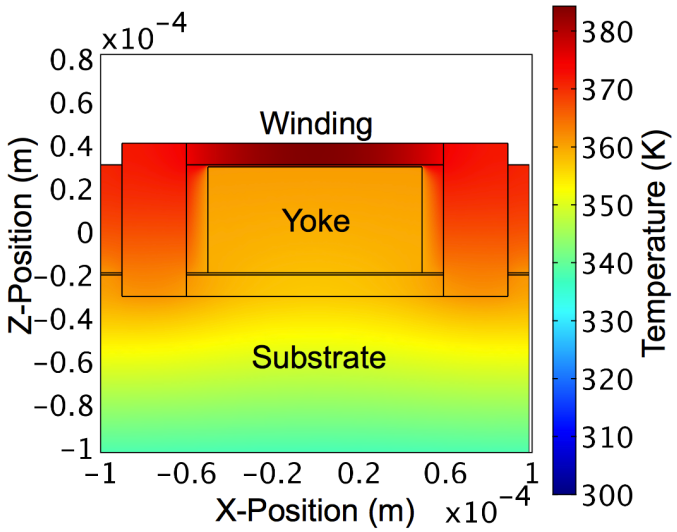

Figure 3.19: Temperature distribution simulation (Kelvin) of a λ_u = 400 μm undulator winding cross-section driven with 5 A, producing 1.2 T, fabricated on a 200 μm thick Si wafer.

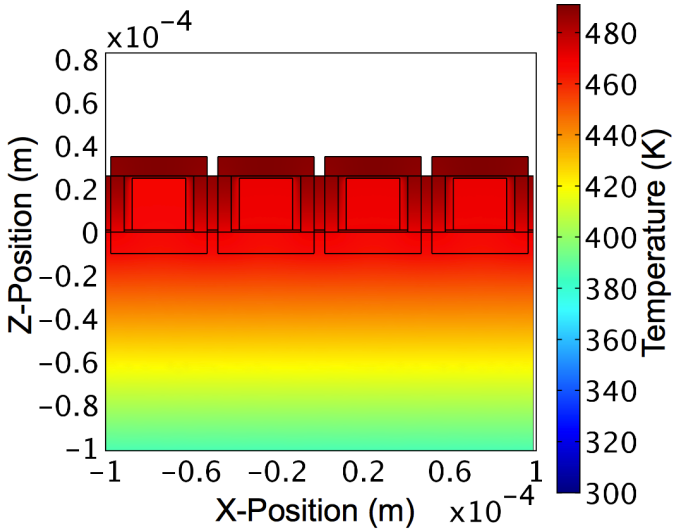

Figure 3.20: Temperature distribution simulation (Kelvin) of a λ_u = 100 μm undulator winding cross-section driven with 0.8 A, producing 0.3 T, fabricated on a 200 μm thick Si wafer.

For geometries that generate more surface heat density, conductive heat transfer from room temperature is not sufficient to keep the undulator below the structural polymer's

decomposition temperature. To address this limitation, the structural polymer may be removed by an O_2 plasma etch prior to operation, the undulator must be run pulsed, or a circulating liquid or cryogenic cooler may be used to extract heat from the undulator. Given the τ = 100 ns - 100 μs response of the undulator inductors, pulsed operation at 1 kHz with a 10% duty cycle would allow all undulator designs to be driven with the substrate held at room temperature. Integrated two-phase microjet impingement cooling [WZJ04] is another potential solution to dramatically increase heat transport allowing continuous wave operation without cryogenic cooling.

3.4.2 Wakefields

Wakefields generated by the electron beam in sub-mm gaps are significantly stronger than in mm- or cm-scale undulator beam pipes and have the potential to seriously affect the electron beam energy spread and propagation. There are two main sources for the wakefields, the resistive wall effect and the surface roughness effect.

The resistive wall wakefield is a result of electrical currents induced in the walls of the undulator electron beam waveguide. These finite currents will excite both transverse magnetic and transverse electric waveguide modes, resulting in longitudinal energy modulation and transverse instability of the electron bunch.

Longitudinal wakefields will induce a significant energy spread in the electron bunch as it travels through the undulator when the length of the electron bunch is comparable to a characteristic distance,

$$s_0 = \left(\frac{cg^2}{8Z_0\sigma} \right)^{1/3} \tag{3.13}$$

where c is the speed of light, g is the undulator gap (approximating the waveguide cross-section as round rather than rectangular), Z_0 is the impedance of free space, and σ is the conductivity of the undulator waveguide walls [BS96].

Studies by Bane *et al.* showed that a rectangular aluminum beam pipe reduced longitudi-

nal wakefields by 50% compared to an equivalent sized round copper beam pipe [Ban07]. An aluminum covered rectangular beam pipe is compatible with the fabrication process proposed here, and the wakefield effects for this configuration are calculated below. A $g = 100$ μm undulator with an aluminum covered waveguide has a characteristic distance $s_0 = 724$ nm and a loss factor of $k_z = 0.1$ MV/pC/m. The longitudinal energy modulation of a of a 750 A_{peak} 100 pC electron bunch by short-range resistive wall wakefields were calculated using the GENESIS module Genwake for a variety of undulator gap sizes and plotted in Figure 3.21.

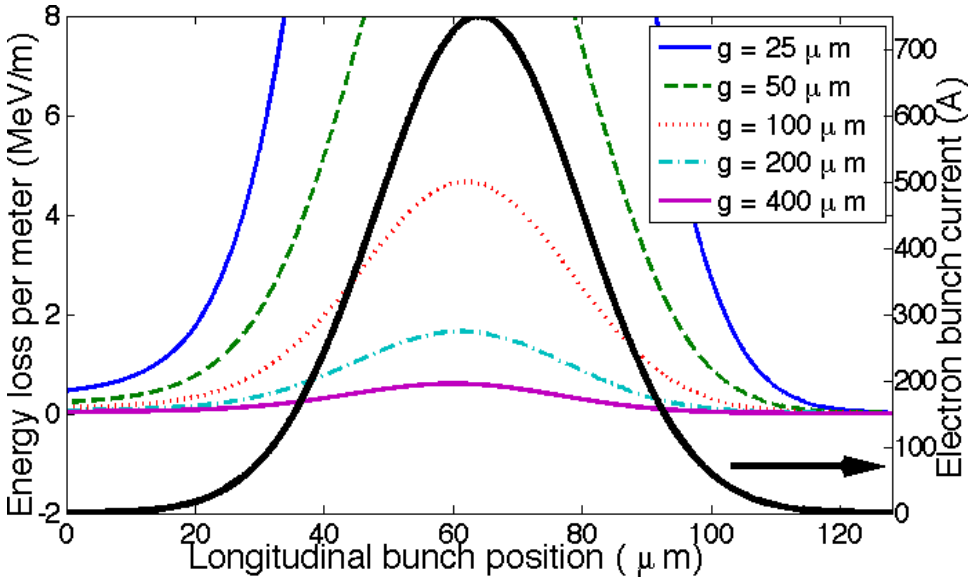

Figure 3.21: Resistive wall component of the longitudinal wakefield for a 750 A_{peak} 100 pC gaussian electron bunch between two parallel aluminum plates separated by g.

The other contribution to the undulator wakefield is due to the boundary conditions on the electric field induced by a rough waveguide wall. This field distortion will impact the energy of subsequent electrons in the bunch with an inductive load on the electron beam [BNC97]. To illustrate this effect, surface roughness wakefields were calculated using the GENESIS module Genwake for an aluminum coated g = 100 μm and g = 400 μm waveguide with a variety of surface roughnesses, R_q, and shown in Figure 3.22.

The surface morphology of evaporated or sputtered metal films is typically characterized by nm-scale surface roughness that follows the underlying topology. The proposed micro-undulator fabrication process uses SU-8 polymer patterned by UV photolithography to define

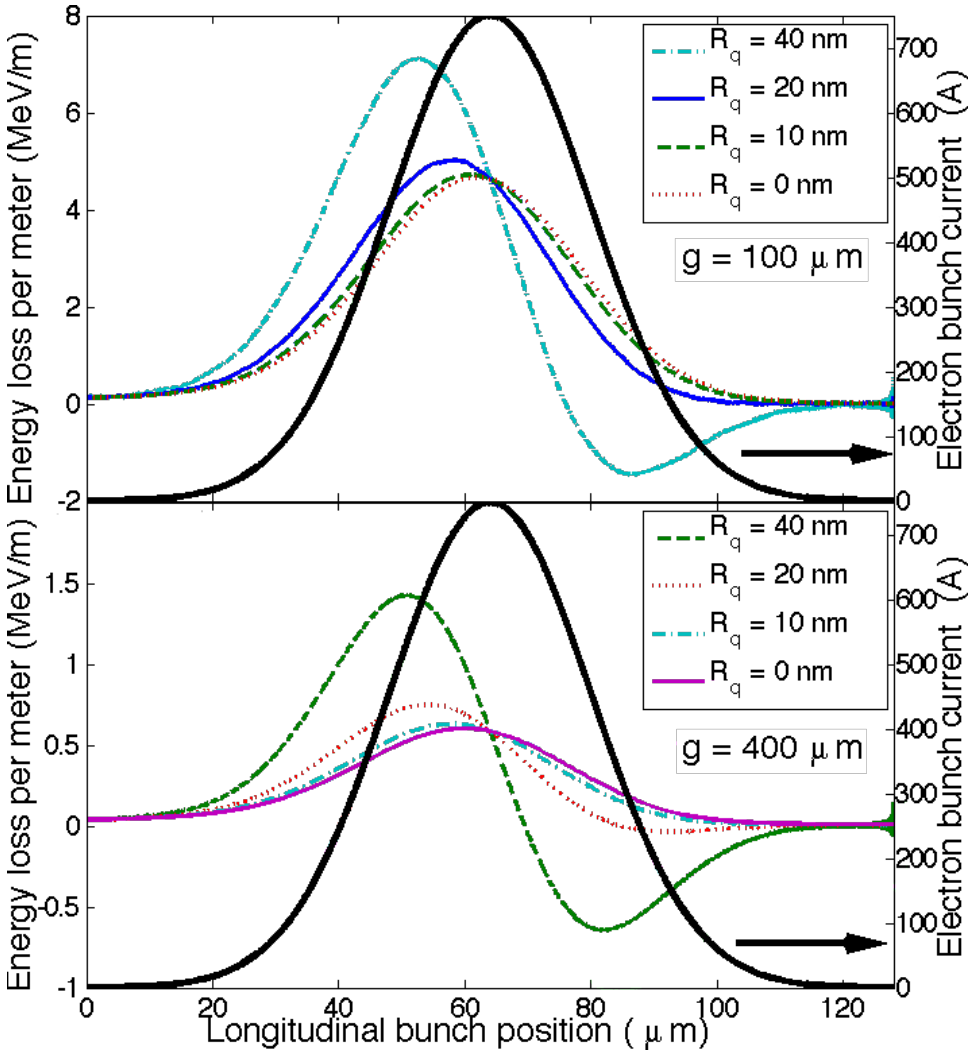

Figure 3.22: Longitudinal wakefield for a 100 pC gaussian electron bunch between two parallel aluminum plates separated by $g = 100$ μm (top) and $g = 400$ μm (bottom).

the sidewall topology. The sidewall of these SU-8 features have a surface roughness below the measurement capabilities ($\sim$ 5 nm) of the scanning electron microscopes used in this work (S-4700, Hitachi Instruments, Inc., San Jose, CA, USA). Tapping mode atomic force microscope measurements have been reported with $R_q \sim 4$ nm_{rms} sidewall surface roughness over a correlation length of 46 nm for proton beam patterned SU-8 [SBS04] and $R_q \sim 4$ nm_{rms} sidewall surface roughness without a reported correlation length for UV-patterned SU-8 [ZSC10]. These values are strongly affected by fabrication process conditions, especially the temperature and duration of subsequent anneal bakes and the temperature, duration, and chemistry of subsequent plasma etching steps. Scanning tip profile measurements of SU-8 films during

the proposed fabrication process have shown surface roughness ranging from $R_q \sim 1$ nm_{rms} to $R_q \sim 100$ nm_{rms}, depending on the exposure of the SU-8 to fabrication process conditions.

Because the FEL instability requires that the energy bandwidth in an FEL slice of the electron pulse be less than the FEL gain (Pierce) parameter, the energy chirp imparted by wakefields can prevent the micro-undulator from operating as a FEL [BS05]. Taking the parameters from the high-gain soft-x-ray FEL amplifier example below, E = 210 MeV, $L_g = 53$ cm, $L_c = 1.5$ μm, and $\rho = 4.5\times10^{-5}$, the induced energy spread across a FEL slice must be less than ∼18 keV/m for FEL operation.

In order to further mitigate the longitudinal energy modulation by wakefields, one needs to reduce the amplitude of the electron distribution or minimize the overlap of the spectral components of the beam longitudinal distribution with the impedance response of the structure. One possibility is to reduce the electron bunch charge and length. This wakefield will be reduced approximately in proportion with the reduction in charge, however, sub-micron bunch lengths may become comparable to the slippage length in the undulator, halting the FEL process. Figure 3.23 demonstrates the overlap between Fourier transformed $\sigma = 1.6$ μm and $\sigma = 16$ μm Gaussian electron bunches with the same 750 A current, and a g = 100 μm rectangular waveguide wake function ([Cha93], equation 2.75).

Bane *et al*. suggested that vanishingly small periodic fins in a rectangular waveguide beam-pipe would shift the resonant frequency of the cavities between fins beyond the high-frequency cutoff of a finite energy electron beam, $\omega = 2\gamma c/g$ ([BS03], footnote 17). This analysis was carried out to study surface roughness wakefields, but hints at an interesting strategy to mitigate the effects of wakefields in a waveguide. Periodic structures are a common method for eliminating unwanted propagating modes in microwave waveguides. Neglecting higher order modes, additional wakefields caused by the waveguide discontinuities, and the evanescent fields in the waveguide stop-bands, 15 μm fins spaced 15 μm apart in a 100 μm wide waveguide should reduce the resistive wall wakefield.

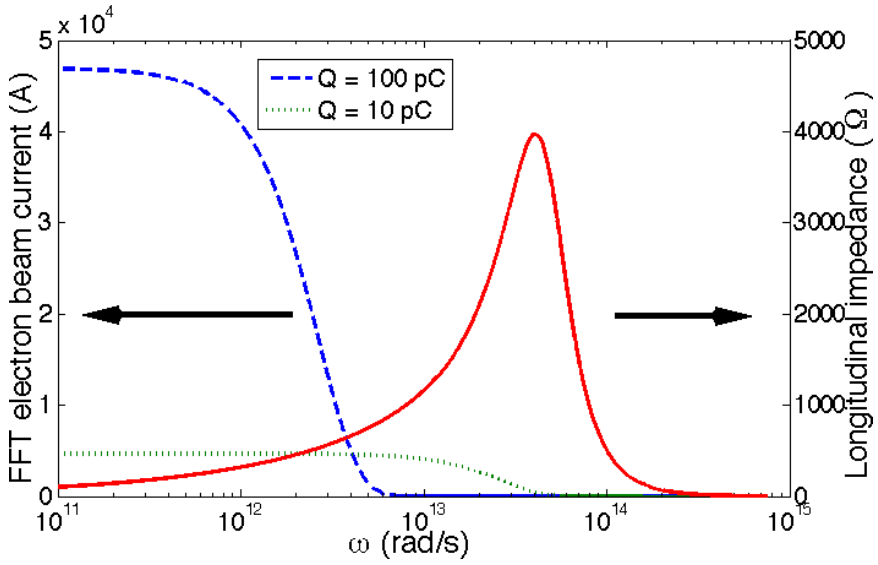

Figure 3.23: Spectral distribution of a 750 A_{peak} 10 pC and 100 pC gaussian electron bunch (dashed) and the resistive wall impedance per unit length for a g = 100 μm aluminum waveguide (solid).

3.4.3 Electron beam induced heating

Energy dissipation in the undulator waveguide by longitudinal wakefields will also cause Joule heating, further complicating thermal management of the undulator.

A 116 MeV electron beam with continuous 1 mA electron current will dissipate 200 W in 5 cm of a g = 100 μm undulator waveguide. Wakefield induced joule heating will dissipate 334 μJ per shot into each meter of undulator length for a 100 pC bunch in a g = 100 μm R_q = 10 nm_{rms} aluminum-coated undulator waveguide due to the wakefields shown in Figure 3.22. At a repetition rate of 1 MHz, wakefields will dissipate <1 kW/cm^2 in the waveguide.

The total of all electron induced heat loads is less than the expected electromagnet dissipation at saturation.

3.5 Micro-undulator system examples

While there are many potential applications of micro-undulators, two use cases are presented here: an undulator radiation source with a high average current beam and a high-gain soft

x-ray FEL amplifier.

3.5.1 Undulator radiation source with a high average current beam

The first example takes advantage of the relatively low power requirements of an electromagnetic micro-undulator. Competitive approaches to ultrashort wavelength undulators are all based on high power laser pulses which typically have limited repetition rates (< 1 kHz). In fact, it is common to invoke complex designs involving recirculating cavities and multi-interaction schemes to get a high average photon yield with a laser based source [JSG07]. Conversely, only a few amps of current are required to drive the electromagnetic micro-undulator, and it is practical to apply current continuously to the micro-coils and have the magnetic field on at all times. It is then natural to couple this undulator with an electron beam from a CW or high duty cycle electron accelerator.

As an example, we consider injecting a 1 mA 116 MeV beam with parameters typical of proposed Energy Recovery Linacs [MH10] into a micro-undulator with 400 μm period, 100 μm gap, and 18 cm total length. The magnetic field of the micro-undulator in this case can be as high as 1 T. The resonant wavelength for this case is $\lambda_r = 3.9$ nm. Assuming the undulator natural focusing is equal in the the two planes, the undulator beta function, a parameter proportional to the depth of focus and inversely proportional to the beam width, is

$$\beta^\star = \frac{\sqrt{2}\gamma\lambda_u}{K2\pi}. \tag{3.14}$$

Due to the small value of K, this only provides weak focusing. In principle, strong focusing could be added to the micro-undulator. But this would require a careful magnetic design because the yoke operates very close to saturation and non-linear effects may take place. The total undulator length is then set by the distance of the upstream optics required to focus the beam to a rms beam size small enough to fit the beam through the undulator. For the sake of discussion, we shall require $\sigma_0 < 20$ μm to minimize the portion of the beam incident on the undulator poles (0.1%, or $\sim$100 W). Assuming a normalized transverse emittance of

$\epsilon_n = 1$ mm-mrad, we can estimate the undulator length $L_u = 2\sigma_0^2\gamma/\epsilon_n \cong 18$ cm.

The total number of photons produced can be estimated using the fact that each electron traversing the undulator will emit $(\pi/3)\alpha K^2$ photons per undulator period (α is the fine structure constant) in a narrow cone with half-width $\sqrt{\lambda_r/(N_u\lambda_u)} = 0.1$ mrad. The number of photons per second is 3×10^{13} s^{-1}. This photon flux is larger than the state-of-the-art in advanced multi-interaction Inverse Compton Scattering schemes. Another important advantage of this scheme is the spectral brightness. The bandwidth of the radiation could be affected by various factors, such as beam energy spread and emittance. The contribution to the bandwidth due to the undulator itself could be very narrow ($< 0.1\%$). This is not easily achieved in ICS sources where many factors, such as the laser bandwidth or diffraction effects in the focusing geometry, come into play in broadening the spectrum of the generated x-rays [RW06]. The parameters of this example are listed in Table 3.3.

Table 3.3: High-average-power soft x-ray source based on a 400-μm period MEMS undulator

E-beam energy	116 MeV
E-beam current	1 mA
Beam emittance	1 mm-mrad
Undulator period	400 μm
Undulator gap	100 μm
Peak magnetic field	1.0 T
K (rms)	0.026
N_u	450
Undulator length	18 cm
λ_r	3.9 nm
E_r	319 eV
Average radiation power	800 μW
Total photon flux	10^{13} s^{-1}

The main problem limiting the obtainable x-ray flux using the micro-undulator is the small normalized vector potential K. An interesting possibility to increase the number of photons produced is to substantially decrease undulator gap, increasing the peak magnetic field. In this case, wakefields will broaden the radiation and higher (odd) harmonics appear in the undulator spectrum because the magnetic field on the undulator axis is no longer

sinusoidal. Nevertheless, the number of photons generated by the beam can be significantly larger.

Even with this preliminary design it is interesting to note that the micro-undulator opens the possibility of production of nearly monochromatic short wavelength radiation by relatively low energy electron beams without the need for expensive and bulky high average power laser systems.

3.5.2 High-gain soft x-ray FEL amplifier

The second example that we analyze is the possibility of using an ultra-high-brightness beam in conjunction with the micro-undulator. This is a very exciting case, since the energy requirements to access high gain FEL amplification and production of coherent radiation at short wavelength will be strongly reduced, bringing a significant advantage in terms of size and cost for a x-ray laser. While the potential of this device is exciting, wakefields will significantly impact the FEL process, requiring new strategies to mitigate these effects before a micro-FEL can be realized.

We consider an example where the micro-undulator period is 400 μm, gap is 100 μm, and produces a magnetic field amplitude of 1 T. Assuming an input beam energy of 210 MeV, the resonant wavelength of the system is 1.2 nm. The matched beam size for a 0.05 mm-mrad normalized emittance beam is 13 μm. It is straightforward to calculate the 1D FEL parameter $\rho = 4.5 \times 10^{-5}$. The 1D gain length of the system is 41 cm and taking into account the 3-D effects using Ming Xie's fitting formulas [Xie00] we get 53 cm gain length. In particular, this could be attractive to a variety of FEL test facilities in the 200 - 300 MeV energy range (SPARC, PSI, SDL) which have already demonstrated kA-class beams and sub-mm-mrad emittance. With some improvements to the beam brightness, it could be possible for these facilities to achieve the parameters used in our FEL simulation, which are reported in Table 3.4.

Exponential amplification of the undulator radiation was simulated with the 3-D FEL code GENESIS [RMG07] including in-slice longitudinal space charge effects without wake-

Table 3.4: High-gain soft x-ray FEL amplifier based on a 400-μm period MEMS undulator

E-beam energy	210 MeV
E-beam peak current	750 A
Beam emittance	0.05 mm-mrad
Undulator period	400 μm
Undulator gap	100 μm
Peak magnetic field	1.0 T
K (rms)	0.026
N_u	20000
Undulator length	8 m
λ_r	1.2 nm
E_r	1 keV
Peak radiation power	6.7 MW
Peak photon flux	10^{22} s^{-1}

fields and with resistive wall and surface roughness wakefields. Wakefields were calculated using the GENESIS module Genwake assuming a g = 100 μm aluminum covered waveguide with 10 nm surface roughness. Figure 3.24 shows the power output averaged across the 100 pC electron bunch from the beginning of the undulator to the saturation regime.

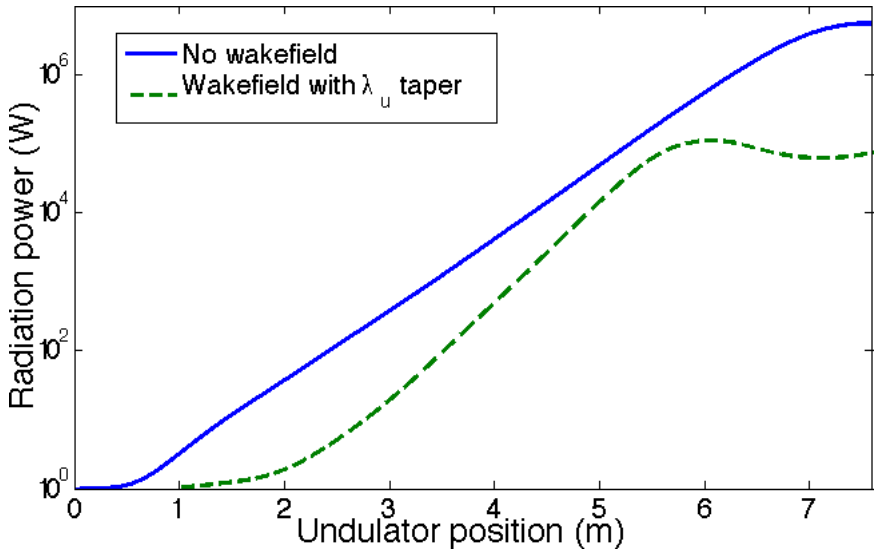

Figure 3.24: 3-D FEL simulation of the average micro-undulator radiation power across the electron bunch with and without longitudinal wakefields.

Without wakefields, we can extract a gain length for the FEL of 51 cm and estimate 5.5 MW of coherent radiation power in 8 m of undulator from the time independent GENESIS simulation. The difference between the simulated gain length and the gain length

calculated using Ming Xie's formula is likely due to space charge forces which are included in the GENESIS simulation, but not in Ming Xie's formulas. The space charge term in the FEL growth eigenfunction, σ_{SC}^2/ρ, has a stabilizing effect competing with the FEL instability [MPB85]. This stabilization increases the gain length, affecting the performance of short-period FELs. Preliminary work to obtain a simple fitting formula to including space charge effects has been made in Marcus *et al.* [MHR11], although three dimensional simulations are still required to self-consistently include the emittance effects.

Wakefields in the small gap of the undulator modulate the electron energy across the electron bunch. The finite electron bandwidth increases the length of the lethargy regime, prevents the FEL instability from developing in FEL slices where the wakefield-induced bandwidth is greater than 18 keV/m, and causes premature FEL saturation. GENESIS simulation shows that these effects increase the FEL gain length to 1.3 m, reduce the average power across the bunch to 110 kW at saturation, and cause FEL saturation after 6 m of undulator. Radiation bandwidth at saturation is 13%.

In practice, a high performance FEL design with a sub-mm gap undulator will require a larger Pierce parameter, shorter gain length, and a waveguide that mitigates the effects of wakefields. A low-emittance ultra-high current electron beam, such as the 10s of kA beams reported from laser-wakefield accelerators [GTV04, GNP08], could be an option to reduce the gain length below 10 cm and increase the Pierce parameter beyond 1×10^4. Real improvement in power output would be limited, however, because wakefields scale up with the peak current. A design that directly addresses longitudinal wakefields in the waveguide could include periodic fins to eliminate propagating transverse magnetic modes of the wakefield.

Since the maximum size of substrates and nanofabrication tooling is limited, a power saturated FEL micro-undulator will involve aligning 10s of 8+ cm undulator sections with sub-μm accuracy. Harmonic production will be limited due to the very small undulator K value. These results show potential for surface-micromachined magnetic undulators to couple with high-brightness beams for ultra-compact FELs operating in the exponential gain region.

CHAPTER 4

Fabrication

MAGNETIC MEMS at UCLA has benefitted from two decades of research in Prof. Judy's laboratory, JUDYLAB, and the generous contributions of expertise and equipment by Dr. Ira Goldberg. The surface-micromachined racetrack solenoid electromagnet manufacturing process started in JUDYLAB with Dr. Michael Glickman [GTH11], building long-throw MEMS relays. Building on this research, the UCLA RF-switch was developed in Prof. Candler's Sensors and Technology Laboratory as an extension of the magnetic relay with changes to increase the relay force and throw: a thicker magnet yoke and greater winding cross section. Fabrication process development continued from these RF-switches to magnetic beam optics, where the same benefits of high energy density and high magnetic gradients could be utilized for particle beam systems [HJL12, HJH14].

4.1 The UCLA RF-switch process

The UCLA RF-switch was a project between the successful UCLA MEMS relay and the magnetic beam optics that forms the majority of this dissertation. Several process changes to the UCLA relay were made to enable the increased yoke thickness necessary for longer actuation distance, and this increase in yoke thickness enabled the realization of effective particle beam optics. The final metallization step of the 3-D solenoid process in the UCLA magnetic relay process was replaced with a patterned planarizing photoresist film and a dual-damascene metallization step. The winding cross section in the UCLA magnetic relay had been limited to 1.8 μm by the process that defined the bottom layer of the windings, a plasma etch into oxide and a self aligned evaporative lift-off. This process was replaced

with a single-damascene process into oxide-coated silicon, increasing the bottom layer of the windings to 10-μm thickness.

The final metallization step in the relay process required a continuous lithographic pattern from the bottom layer of the windings, over the high-aspect-ratio magnet yoke sidewall, across the magnet yoke, and down the high-aspect-ratio sidewall to the other side. Negative-tone photoresists suffer from poor pattern fidelity at the base of the sidewall, where shadowing prevents cross linking of the polymer between adjacent windings. Increasing dose to compensate for shadowing leads to unacceptably high stress in the thick film, and delamination during the through-mold electroplating process. Positive-tone photoresists suffer similar shadowing challenges, but increasing the dose can resolve the pattern without increasing the stress. Thick positive-tone photoresists, however, become opaque with increasing dose. This limits the maximum photoresist thickness that can be patterned with a single exposure and development cycle, and the maximum yoke thickness of the UCLA magnetic relay process.

A planarizing photoresist layer step was added to address the step-coverage issues with thicker (>20 μm) yokes. The subsequent negative-tone photoresist electroplating mold can then resolve the top winding layer without shadowing.

Figure 4.1 illustrates the RF-Switch process and the following text describes it in detail.

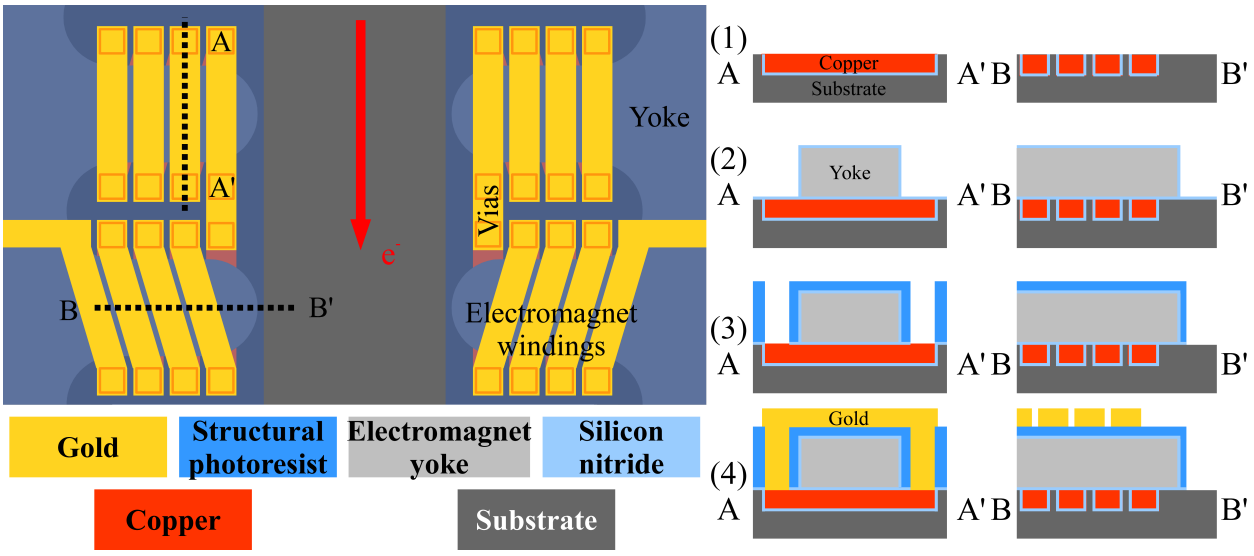

Figure 4.1: Illustration of the RF-switch process used for an early attempt at MEMS undulators and focusing optics.

4.1.1 Bottom winding layer

The pattern for the bottom coil windings is photolithographically defined on a high-resistivity silicon wafer using a 5-μm-thick sacrificial high-aspect-ratio negative-tone photoresist (KMPR 1007, Microchem Corp., Newton, MA, USA). Using this soft mask, 10-μm trenches are anisotropically etched in the silicon wafer using the Bosch process [LS96] with a deep reactive ion etcher (SLR-770, Plasma-Therm, St Petersburg, FL, USA). The duration of the second etching step of the Bosch process is reduced by 20% to provide a slightly canted sidewall (Figure 4.2). This improves coverage of the metallization adhesion layer in a later step. The photoresist is removed in an organic photoresist stripper (ALEG-380, J.T. Baker, Phillipsburg, NJ, USA) and the wafer surface is cleaned in an O_2 plasma (Matrix 105 Plasma Stripper, Matrix Integrated Systems, Richmond, CA, USA).

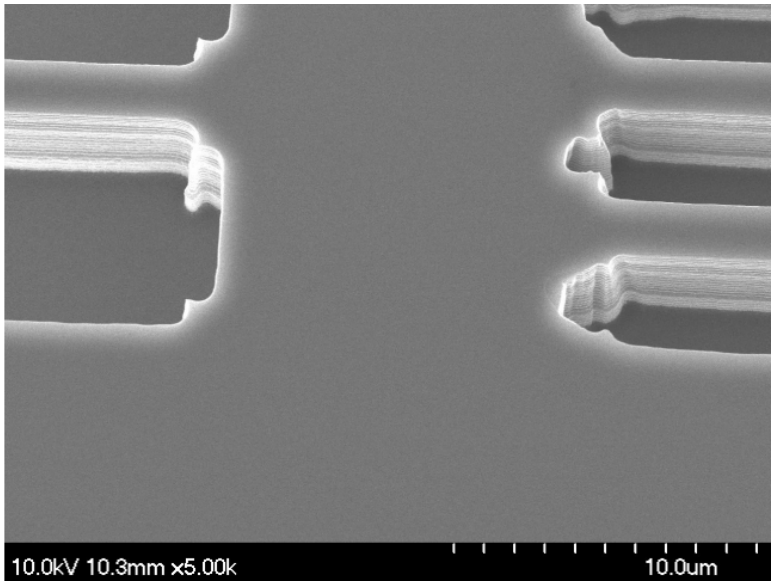

Figure 4.2: Image showing the trench sidewall angle.

A 100-nm insulating layer of silicon nitride is deposited by inductively-coupled plasma-enhanced chemical vapor deposition (STS MESC Multiplex CVD, SPTS Technologies Limited, Newport, United Kingdom) to isolate the bottom windings from the silicon substrate. The wafer is sputter-etched for 5 minutes, and an electroforming seed is deposited on the surface of the silicon nitride by RF sputtering with a 20-kV wafer bias (CVC 601, Consolidated Vacuum Corporation (was CVC, now VEECO), Plainview, New York, USA). Wafer

bias is necessary for adequate coverage over the 10-μm wafer topology. The seed layer consists of 30 nm of titanium to provide adhesion to the substrate, 300 nm of copper to carry the electroplating current and compatibility with copper electroplating, and 30 nm of titanium to protect the copper from oxidation. The exposed seed layer is etched to copper in 1% hydrofluoric acid and a 12-μm-thick copper film is electroplated from a phosphorized copper anode in a sulfate based solution (Technic Elevate copper 6320, Technic Inc., Rhode Island, USA). The film is polished back down to the silicon surface (PM5, Logitech Ltd., Glasgow, Scotland), yielding the bottom of the electromagnet winding pattern. Figure 4.3 shows devices after the bottom-winding-layer damascene process.

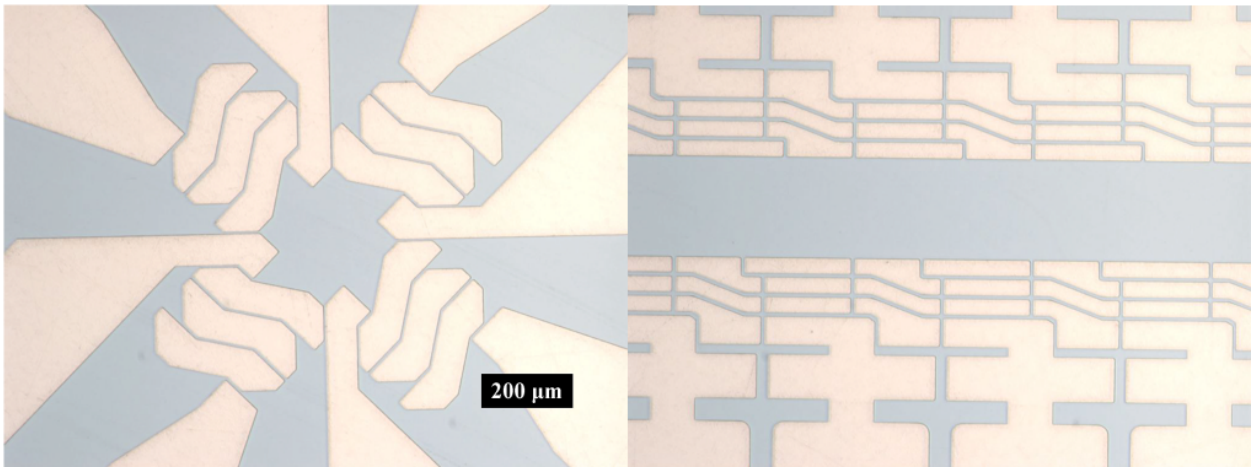

Figure 4.3: Image of a quadrupole electromagnet (left) and undulator (right) during the bottom winding layer step.

The thickness of the bottom metal layer cannot exceed 10 μm with this process due to non-uniform polishing with the CMP. Thickness could be increased by filling blank areas of the wafer with a pattern to normalize the down-force across the wafer.

A 300-nm insulating layer of silicon nitride is deposited by inductively-coupled plasma-enhanced chemical vapor deposition (STS MESC Multiplex CVD) to isolate the bottom windings from the conductive magnet yoke.

4.1.2 Magnet yoke

An electroforming seed is deposited by sputtering (CVC 601) on the surface of the silicon nitride. The seed layer consists of 30 nm of titanium to provide adhesion to the substrate, 300 nm of copper to carry the electroplating current and provide a surface compatible with magnetic alloy (NiFe, CoNiFe, or CoNiP) electroplating, and another 30 nm of titanium to protect the copper from oxidation before plating and to provide adhesion between the metal and the electroplating mold.

A 60-μm film of high sidewall-aspect-ratio negative-tone photoresist (KMPR 1025) is photolithographically patterned into the geometry of the magnet yoke. The exposed seed layer is etched to copper in 1% hydrofluoric acid, and the magnetic alloy that forms the electromagnet yoke is electroplated through the mold using the process detailed by Glickman *et al*. [GTH09]. The mold is removed by delamination after soaking 8 hours in heated organic photoresist stripper (ALEG-380, J.T. Baker, Phillipsburg, NJ, USA). The electroplating seed is stripped by consecutive immersions in 1% hydrofluoric acid, a mixture of 5% acetic acid and 15% hydrogen peroxide, and 1% hydrofluoric acid. Figure 4.4 shows devices after the magnet yoke electoplating mold is stripped.

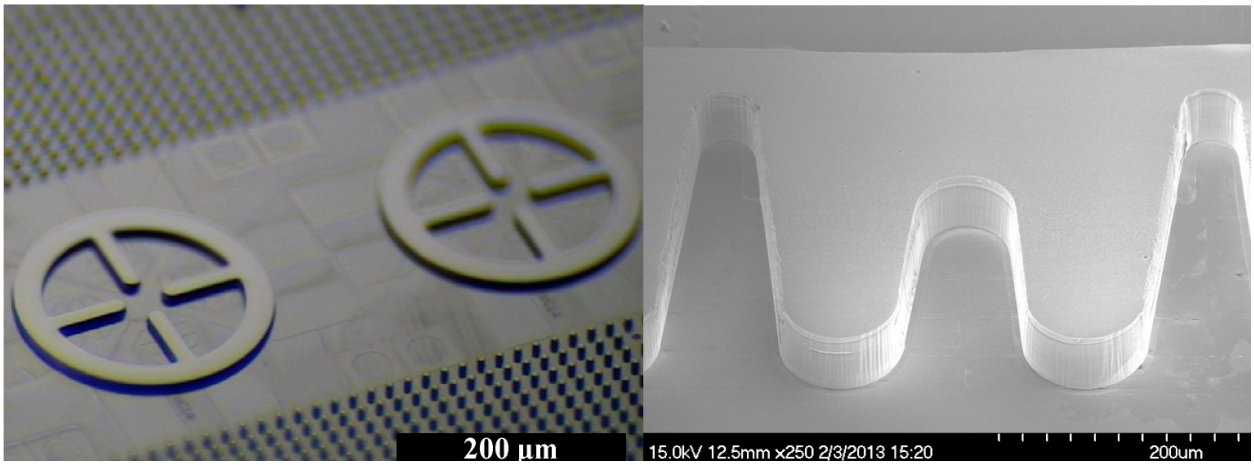

Figure 4.4: Image of a quadrupole electromagnet (left) and undulator (right) after the magnet yoke electroplating step.

4.1.3 Planarization layer

A 55-μm layer of structural photoresist (Microchem SU-8 2025) is spun on the wafer to isolate the conductive magnet yoke from the top layer of the coil windings. The photoresist is patterned using photolithography to define the coil winding interconnects and the electron beam path and annealed under vacuum for 8 hours at 230°C.

The silicon nitride covering the copper at the base of the vias is etched with an inductively coupled CF_4 plasma (STS MESC Multiplex AOE) to expose the bottom windings of the coil. Figure 4.5 shows devices after the planarization layer is polished.

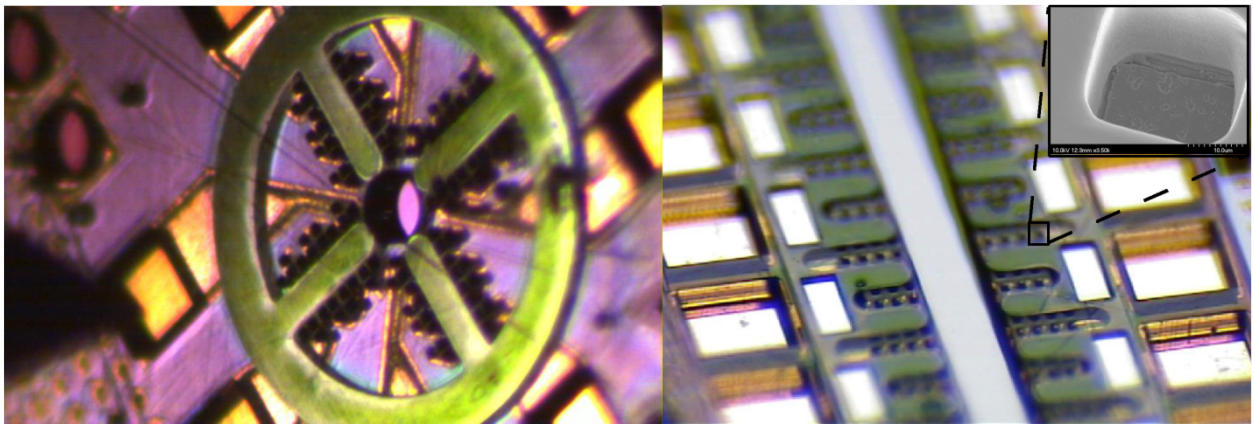

Figure 4.5: Image of a quadrupole electromagnet (left) and undulator (right) after the planarization-layer step. The inset figure shows a via with the oxide etched at the base.

A systematic manufacturing defect appeared at this step. Patterns in the negative tone planarizing photoresist in the center of concave features in the magnet yoke became cross-linked even when the magnet yoke was completely covered by the photomask. This is shown in Figure 4.6. This unwanted photoresist caused open-circuited windings in the undulator structure, resulting in reduced die yield. This problem was addressed in the next iteration of the fabrication process by electroplating via pillars through a pattern prior to the magnet yoke step.

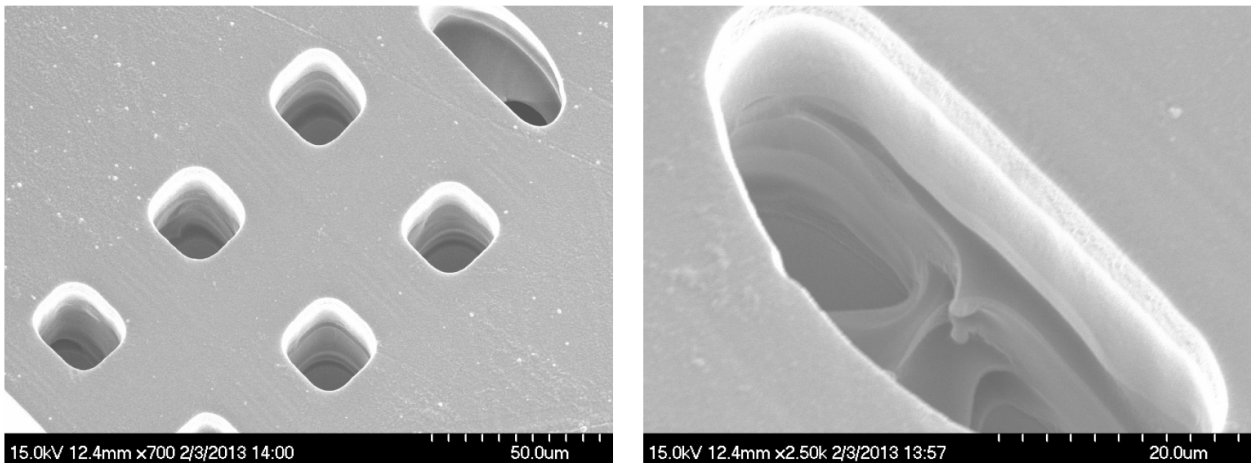

Figure 4.6: Image of a undulator via structure (left) and a close image of an undulator via at the center of the concave features defining the back of the undulator yoke (right). The via at the back of the yoke shows unwanted cross-linked photoresist in both cases.

4.1.4 Top winding layer

Another Ti/Cu/Ti electroforming seed is sputtered on the surface (CVC 601). To achieve coverage on the sidewalls of the high-aspect ratio vias, the copper sputtering step is split into 3 steps: 300 nm is RF-sputtered without wafer bias, 150 nm is sputtered with 20 kV wafer bias, and another 300 nm is sputtered without wafer bias. These steps anisotropically deposit copper on the surface of the wafer with little sidewall coverage, redeposit that metal on the sidewalls using the sputter-etching from the wafer bias, and then replenishes the copper thickness with a third coat. Figure 4.7 shows the metrology results from this sputter-coverage process.

A negative-tone photoresist electroplating mold (Microchem KMPR 1005) is patterned into the geometry of the top layer of the electromagnet coil windings. Gold is electroplated from a potassium aurocyanide bath (Technic HS434) heated to 55°C with strong agitation from a platinized titanium anode through the photo-patterned mold to complete the electromagnet coil windings. The mold and electroplating seed are stripped using the process described above, completing the undulator solenoids. Figure 4.8 shows devices after the top winding layer.

Electroplated gold can be seen peeling off the sidewalls of the inset wirebonding pads in

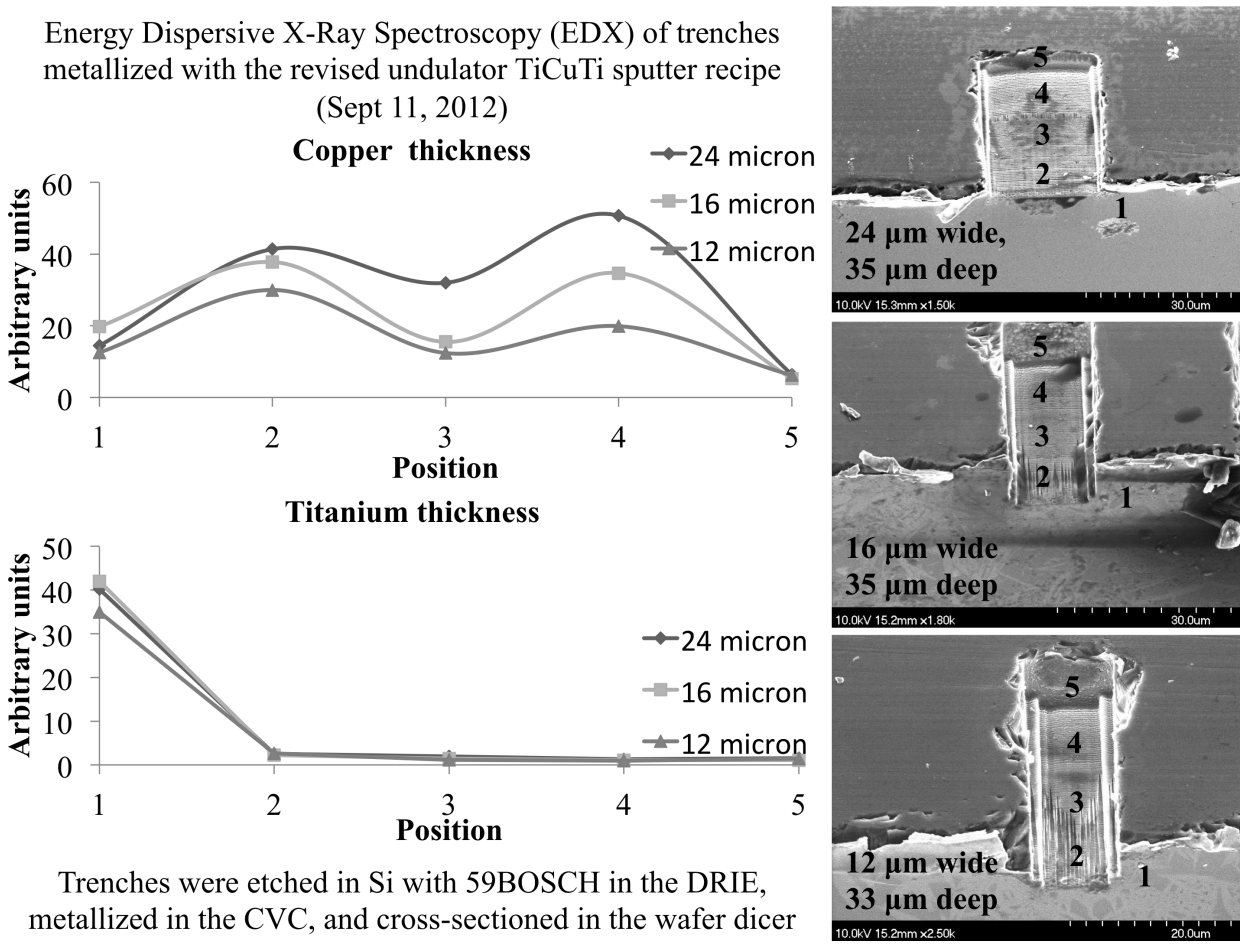

Figure 4.7: Via-coverage process development.

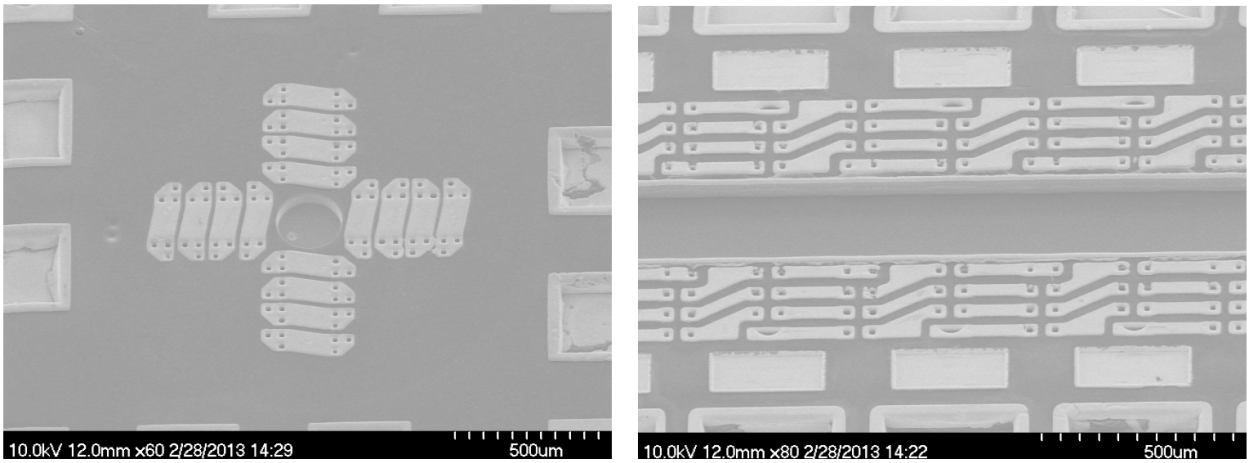

Figure 4.8: Image of a quadrupole electromagnet (left) and undulator (right) after the top winding layer step.

the quadrupole and undulator devices. This is due to a combination of internal stress in the deposited gold and poor adhesion of the seed layer due to poor titanium sidewall coverage, as shown by energy dispersive x-ray spectroscopy (EDX) metrology in Figure 4.7.

4.2 Multi-pole electromagnet process

The RF-switch process described was re-designed to address the specific challenges posed by thick-film multi-pole electromagnets [HPH14]. The new process is illustrated in Figure 4.9 and discussed below.

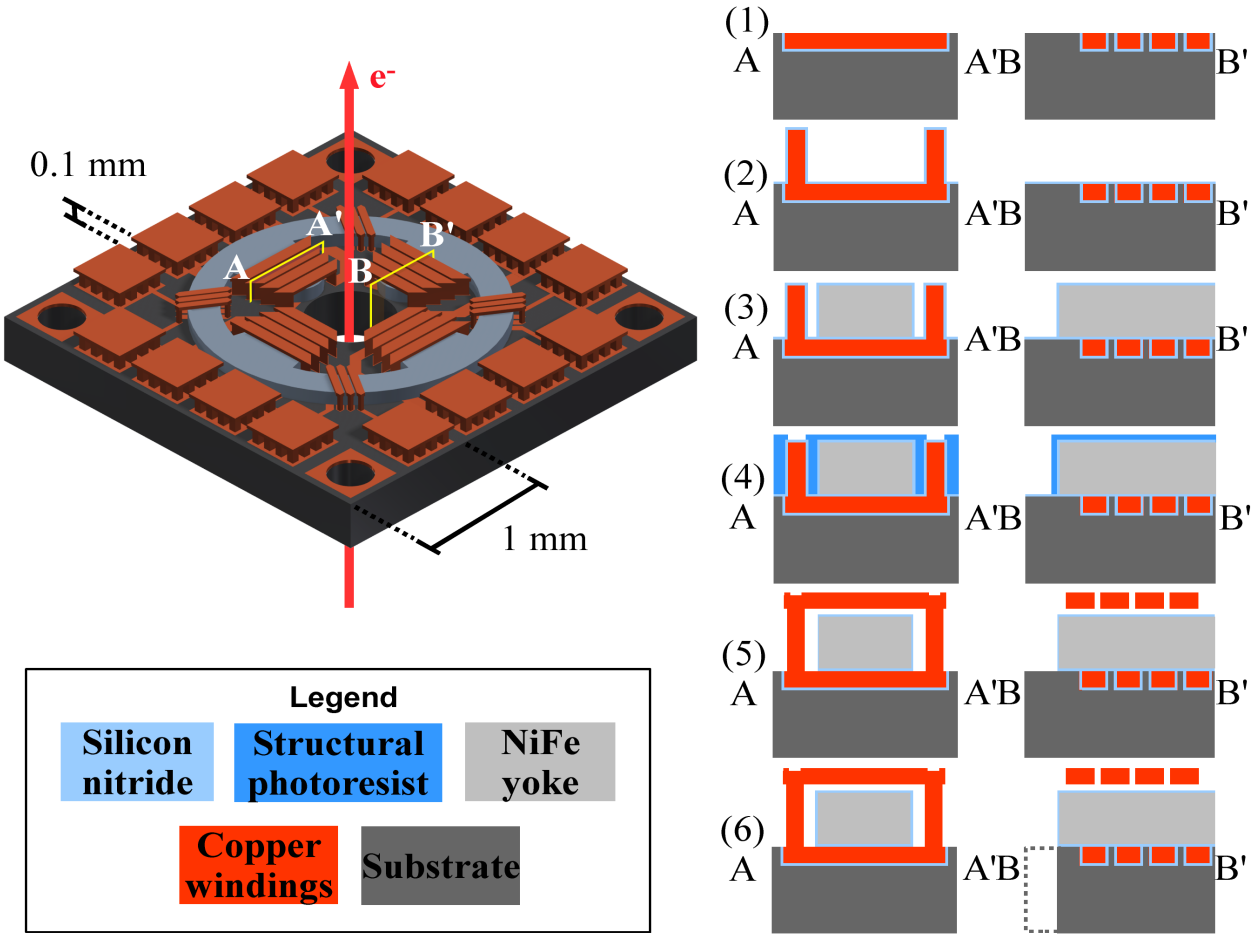

Figure 4.9: Illustration of the revised multi-pole electromagnet process.

Several changes were included throughout the process. The thickness of the bottom winding layer was increased to 20 μm with a deeper etch and a thicker deposit of copper. A

fill pattern was etched into blank areas of the wafer to improve down-force uniformity during the CMP step, producing a inset metal with better than 10% thickness uniformity across the wafer. Reliability of the top-to-bottom winding interconnection was improved by through-mold electroplating the vias rather than filling them from the top with a dual Damascene process. To ensure that there was no photolithographic defects due to diffraction from the mask and reflection off the yoke, the winding via step was inserted between the bottom winding layer process and the magnet yoke process. Bubbles from trapped gas during the spin coat of the planarization layer were removed before soft baking with a short vacuum step.

4.2.1 Bottom winding layer

The pattern for the bottom of the windings is photolithographically defined on a silicon wafer using 5-μm-thick photoresist (KMPR 1005). A regular hole array is patterned filling unused space to make the polishing down-pressure uniform in a later polishing step. Using this soft mask, 20-μm-deep trenches are etched in the silicon using a deep reactive ion etcher (Plasma-Therm SLR-770). The photoresist is stripped in ALEG-380 and 5:1 H_2SO_4:H_2O_2. A 500-nm SiO_2 film is grown by thermal oxidation (Mini 3600, Tystar Corp., Torrance, CA, USA) to isolate the bottom windings from the silicon. The wafer is sputter-etched for 5 minutes, and an electroforming seed is deposited on the SiO_2 by RF sputtering with 20-kV wafer bias (CVC 601). The seed-layer consists of 30-nm titanium for adhesion to the substrate and 300-nm copper to carry the electroplating current. Seed layer oxidation is etched in 1% hydrofluoric acid and a 25-μm copper film is electroplated from a phosphorized copper anode in a sulfate-based solution (Technic Elevate 6320) at 5 mA/cm^2. The wafer is polished down to silicon with chemical mechanical polishing, CMP, (Logitech PM5) using 100-nm alumina slurry, yielding the winding bottom layer inlayed in the substrate.

4.2.2 Winding vias

Another electroforming seed is sputter deposited, with an additional 30-nm layer of titanium for adhesion between the seed and an electroplating mold (i.e., titanium/copper/titanium layer). A 100-μm-thick high-aspect-ratio photoresist (KMPR 1025) film is patterned to define the interconnect geometry of the electromagnet windings. The titanium exposed by the photoresist pattern is etched back to copper in 1% hydrofluoric acid, and 100 μm of copper is electroplated through the mold. The interconnect height is planarized to within 1% uniformity variation across the wafer by CMP with the electroplating mold still on the wafer. The slurry is removed with a dip in 1% hydrofluoric acid.

The mold is removed by plasma etching with 4:1 O_2:CF_4 plasma (STS AOE) using 600-W coil and 50-W platen (capacitively coupled) power. Wet-stripping processes were not able to cleanly remove all of the electroplating mold, and finishing the strip with a long plasma etch resulted in non-uniform sputter-etching of structures on the wafer. The electroplating seed is stripped by increasing the platen power to 200 W and sputter etching the thin metal seed layer. The wafers are dipped in 5% $C_2H_4O_2$ and 1% hydrofluoric acid to ensure a clean surface, and a 2-μm-thick insulating Si_3N_4 film is deposited by plasma enhanced chemical vapor deposition, PECVD, (STS Multiplex CVD) to isolate the windings from the magnet yoke. Figure 4.10 shows devices after the winding-via step.

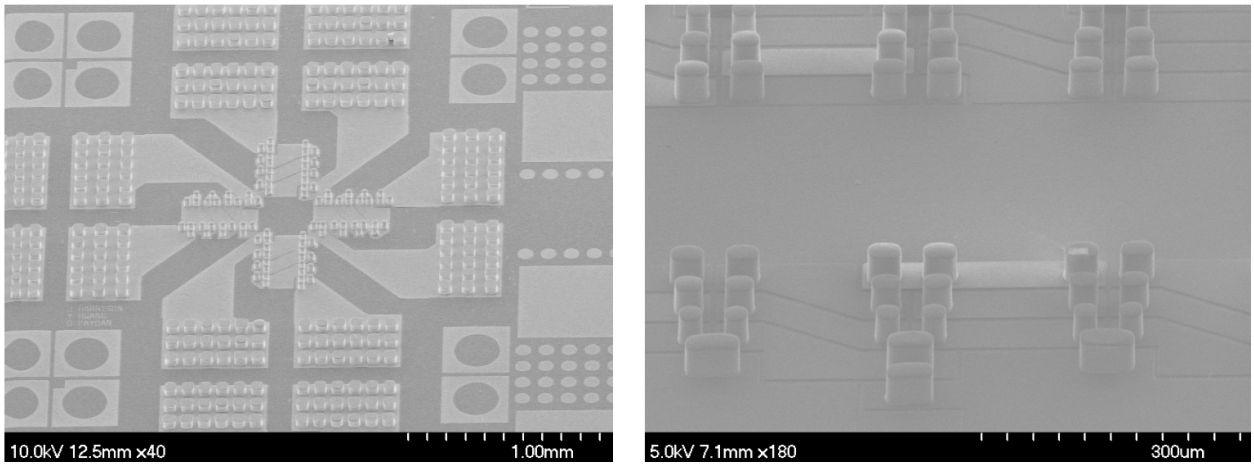

Figure 4.10: Image of a quadrupole electromagnet (left) and undulator (right) after the via-layer step.

4.2.3 Magnet yoke

An electroforming seed is deposited as described in the winding-via step. A 100-μm film of KMPR 1025 photoresist is patterned into the geometry of the magnet yoke. Between pouring the photoresist and spinning, the film is de-gassed in a vacuum oven at 30 Torr for 30 seconds. The exposed seed layer is etched to copper in 1% hydrofluoric acid, and a $Ni_{80}Fe_{20}$ electromagnet yoke (B_{sat} = 1.1 T, μ_r = 8000) is plated through the mold using the process detailed by Glickman et al. [GTH09]. Planarization, mold and seed stripping, and layer isolation proceed as described in the winding via step. Figure 4.11 shows an undulator yoke test structure that was not fully planarized. This planarization step is necessary to guarantee field uniformity locally and across the wafer. Figure 4.12 shows devices after the magnet yoke step.

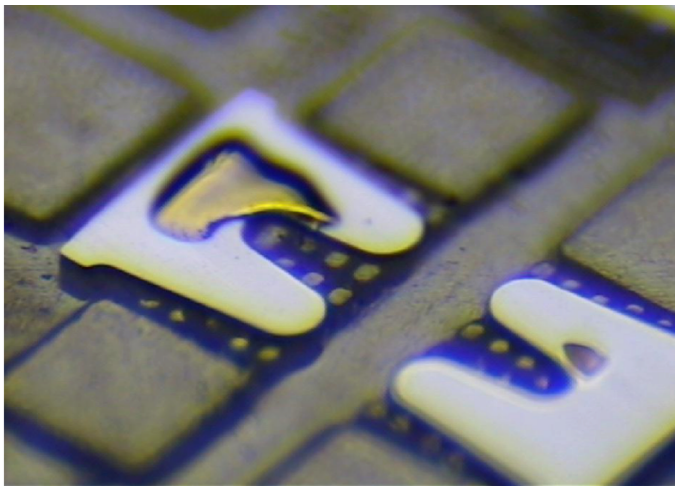

Figure 4.11: Image of an undulator yoke during planarization.

4.2.4 Planarization layer

A 100-μm-thick film of photoresist (SU-8 2025) is used to provide a planar surface for defining the top of the coil windings. The SU-8 is de-gassed in the same manner as KMPR in the previous step, patterned and baked to expose the winding vias, and planarized to 10 μm above the yoke before development to improve thickness uniformity. The film is then annealed in vacuum for 8 hours at 200°C. Figure 4.13 shows devices after the planarization-layer step.

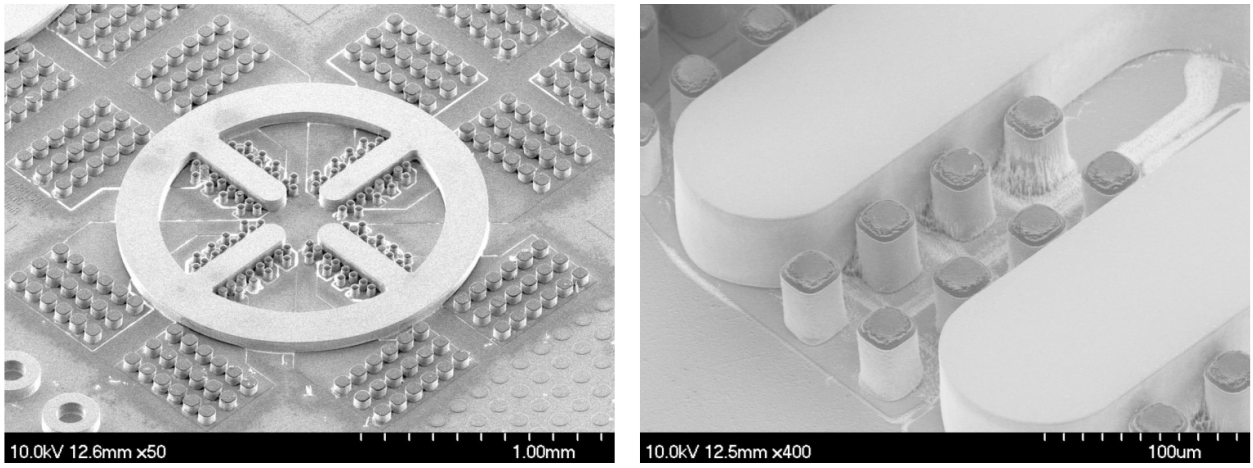

Figure 4.12: Image of a quadrupole electromagnet (left) and undulator (right) after the magnet-yoke step.

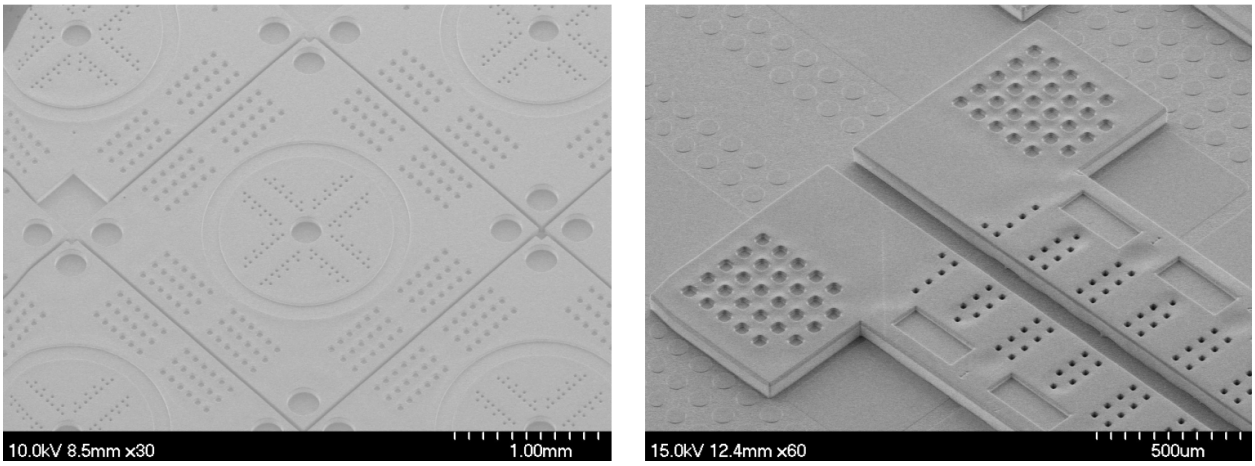

Figure 4.13: Image of a quadrupole electromagnet (left) and undulator (right) after the planarization-layer step.

4.2.5 Top winding layer

The copper in the vias is exposed by etching the Si_3N_4 with C_4F_8 plasma (STS AOE). A seed layer is sputtered on the surface as described in the winding-via step. A 25-μm-thick KMPR 1005 layer is patterned into the geometry of the top winding layer, and 20-μm copper is electroplated through the mold. The mold and seed are stripped using the process described in the winding via step, completing the multi-pole electromagnets. The SU-8 is etched using the mold stripping process described in the winding via step to avoid thermal expansion issues during operation. Figure 4.14 shows devices after the top winding step.

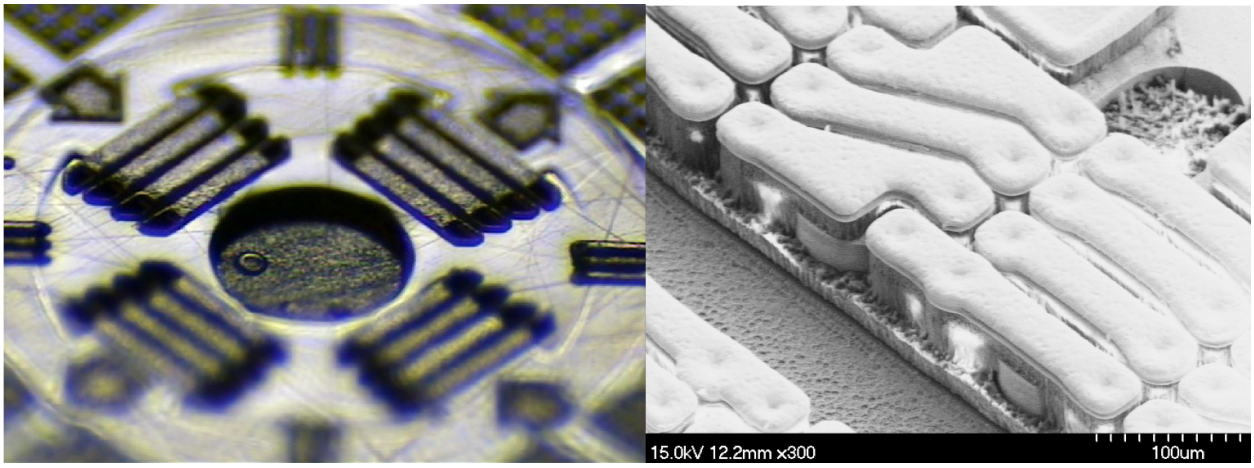

Figure 4.14: Images after the top winding layer step of a quadrupole electromagnet before etching back the planarizing photoresist layer (left) and undulator after etching back the planarizing photoresist layer (right).

Many devices failed after this step due to an insufficiently thick seed layer. The 300-nm-thick copper seed layer etches at ∼100 nm/min, and the titanium and SU-8 below etch rapidly once exposed to the plating solution. If the seed layer is broken through before deposition begins to add material, pits can form and be filled with metal, shorting the winding to the yoke, or the entire winding trace can be lost. Figure 4.15 shows a quadrupole electromagnet that failed completely due to this manufacturing defect. Occasional high-resistance shorts from the top metal layer to the electromagnet yoke that were due to this problem were correctable with a short current pulse.

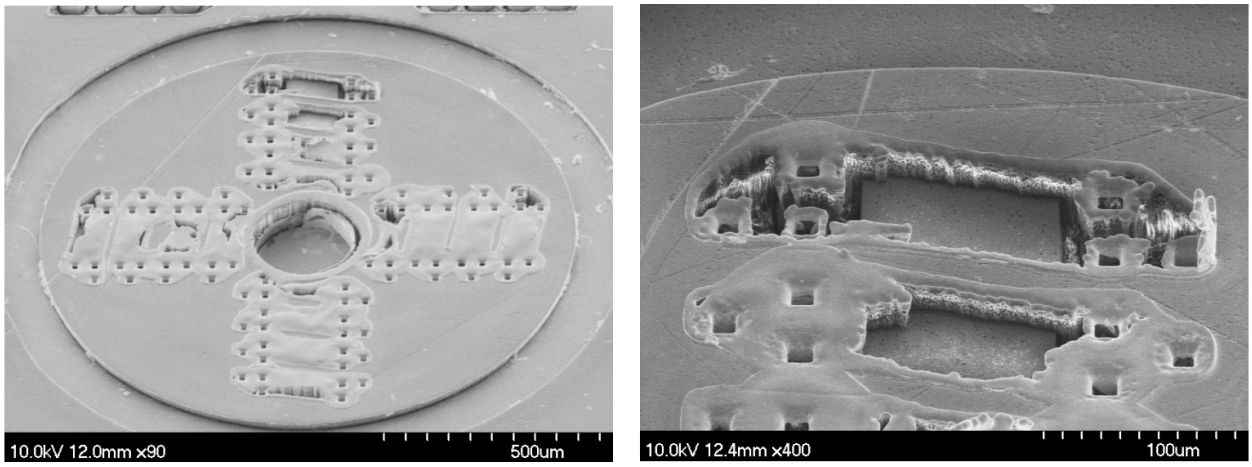

Figure 4.15: Image of a quadrupole electromagnet that failed due to the loss of the seed layer in the time between loading the electroplating tool and starting deposition.

4.2.6 Through-wafer etch

Through-wafer holes are desired in some applications, such as manipulation of charged particle beams. To achieve a through wafer particle path, an etch pattern is defined with KMPR 1005 photoresist on the back-side of the wafer and aligned to the front using a contact aligner. Holes and trenches are etched from the back of the substrate to the front, defining the electromagnet gap and singulating the devices using a post-process Bosch etch (Oerlikon FDSE II). Figure 4.16 shows devices after the through-wafer etch step.

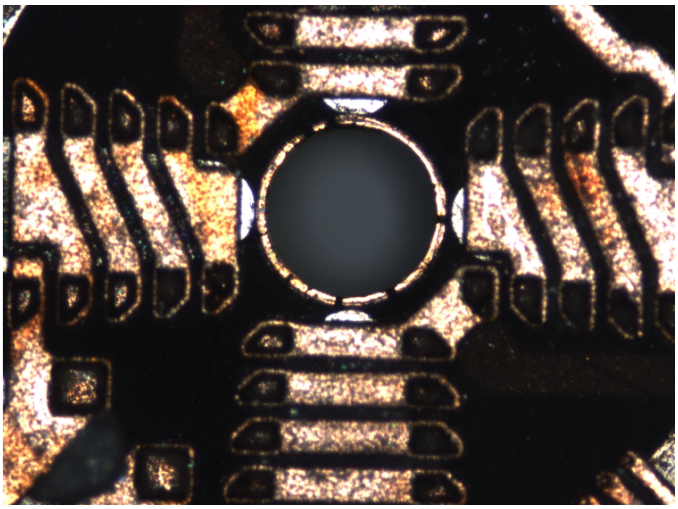

Figure 4.16: Image of a quadrupole electromagnet after through-wafer etching the electron beam path.

4.2.7 Packaging

Integrating microfabricated electromagnets inside a beamline pose challenges that are not typically encountered with macroscopic permanent-magnet, superconducting, or laser beam optics and undulators. The electromagnet transverse structure is sub-mm-size, and it must be placed inside the vacuum beamline, complicating alignment, electrical interconnects, and heat extraction. Spatial measurements of the actual magnetic field are complicated by the small undulator gap. Further, the proximity of the undulator surface to the electron bunch influences the beam characteristics.

Several steps were taken to address these issues. To increase the thermal mass of the

electromagnet, it is mounted in a 1-mm-thick conventionally machined oxygen-free high-conductivity (OFHC) copper fixture. Either a 610-μm or 50-μm hole is made in the fixture with a size 73 drill or laser mill to provide an aperture for the electron beam. To connect the macroscopic coaxial feedthroughs on the beam pipe to the MEMS electromagnet, a vacuum-compatible high-thermal-conductivity PCB (Duroid 6002, Rogers Corp., Rogers, CT, USA) is mechanically mounted on the copper fixture with 0-80 screws, connected to the feedthroughs with vacuum-compatible (PTFE coated) 16 AWG wires (5858 WH005, Alpha Wire, Elizabeth, NJ, USA), and connected to the electromagnet with 15-μm Al wirebonds. Figure 4.17 and 4.18 shows a packaged quadrupole electromagnet. The electromagnet die has withstood 70-A pulses on a probe station without failure, but the 20 15-μm diameter Al wirebonds in the package failed at 5.5 A. The development of a flip-chip bonding process between the electromagnet die and the package PCB would address wire bond failure and increase the tolerable average drive current.

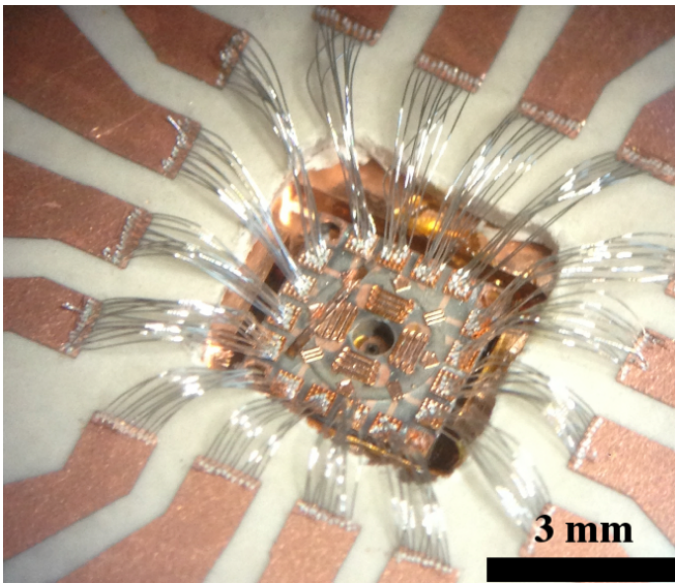

Figure 4.17: Image of a quadrupole electromagnet packaged in a copper beam testing fixture with a laser-machined 50-μm electron-beam aperture.

To produce a well-controlled beam for the experiments using the DC-photogun, three approaches were taken to manufacture an aperture for the electron beam upstream of the MEMS electromagnets: a mechanically drilled 610-μm-wide hole in the 1-mm-thick OFHC copper MEMS die fixture, a laser milled 50-μm-wide hole in the 1-mm-thick OFHC copper

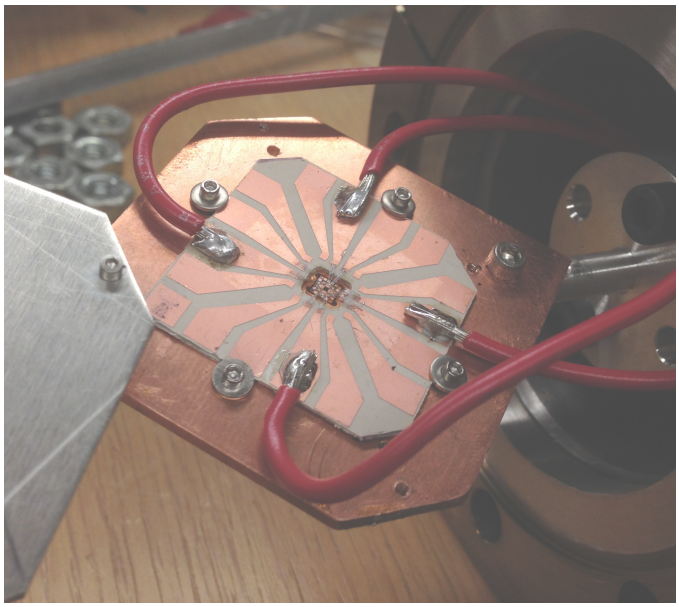

Figure 4.18: Image of a quadrupole electromagnet fixture mounted on a vacuum bellow before insertion into an experiment chamber. The aluminum shield visible on the side of the image bolts over the quadrupole, protecting it from handling damage.

MEMS die fixture, and a translatable aperture made from two orthogonal 20-μm-wide steel slits. The 610-μm-wide hole was machined using a drill press in the UCLA Center for High Frequency Electronics (CHFE). The 50-μm-wide hole, shown in Figure 4.19, was machined by Laserod Corp.

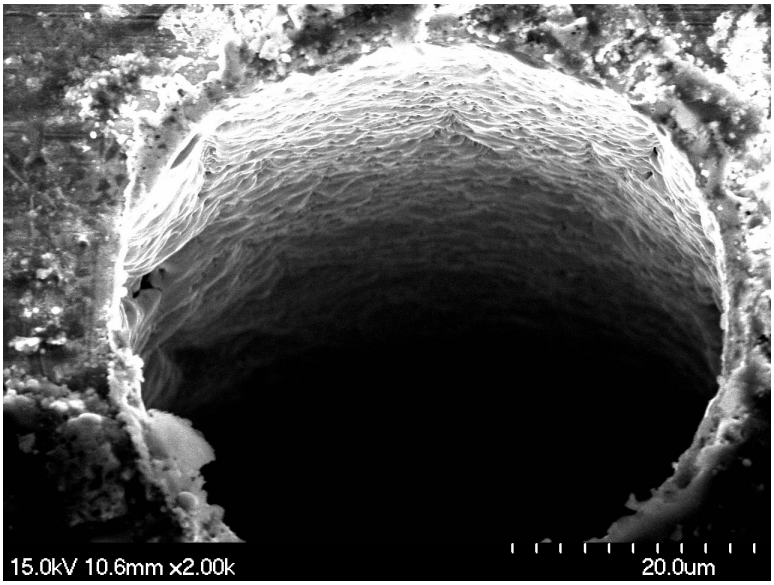

Figure 4.19: Image of the 50 μm wide copper aperture.

The orthogonal slit aperture, illustrated in Figure 4.20, is pair of Thorlabs S20R slits that were chemically stripped of the optical coatings to prevent charging by the electron beam. To clean the oil off the black oxide-coated stainless steel, the slits were soaked in acetone for 1 minute and rinsed in isopropanol. The slits were then soaked in 10% hydrochloric acid for 30 minutes to oxidize the ferrous oxide to ferrous chloride. Vigorous agitation in methanol was then used to dissolve the ferrous chloride. The slit surface was gently brushed with a kimwipe to clean off the remaining ferrous chloride. After thoroughly washing the slits in water, the slits were soaked in sodium hydroxide for 10 minutes to reduce the anodized aluminum surface to aluminum metal. The slits were then washed in water and gently brushed with a kimwipe. To ensure that the entirety of both slits were electrically conducting, 10 nm of gold germanium was sputtered on both sides in a Denton Desktop Sputter system.

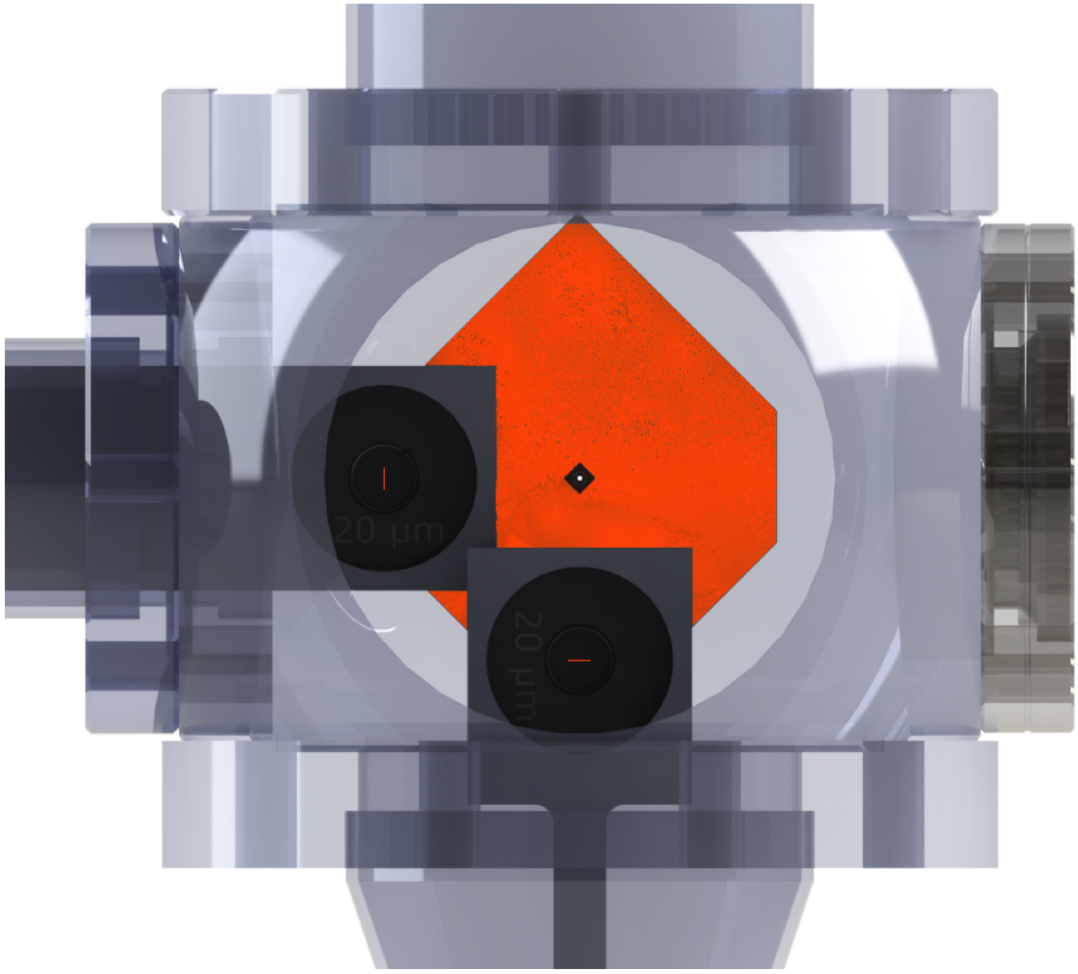

Figure 4.20: Illustration of the orthogonal slit-based aperture.

CHAPTER 5

Characterization

ELECTROMAGNET PERFORMANCE was investigated with impedance characterization before and after packaging and a series of electron beam experiments. Impedance analysis provided the circuit parameters of the device and frequency response, beam deflection and focusing experiments demonstrated the reconfigurability and performance of the device and beam-probe field-mapping of the electromagnet demonstrated the spatial distribution of the fields produced.

5.1 Impedance analysis

Each electromagnet was measured using an impedance analyzer (Agilent 4294A) with a set of coaxial probes (APT 740CJ) in a four-terminal pair configuration. Before packaging, electromagnet impedance measurements of the 600 μm gap quadrupoles showed 58.2$\pm$1.2-mΩ resistance and 30.4$\pm$1.9-nH inductance at 100 kHz. These measurements agree well with the 71-mΩ resistance and 32.2-nH inductance expected from 3-D FEM simulation. Figure 5.1 shows the electromagnet resistance and inductance for these devices before packaging and Figure 5.2 shows the electromagnet resistance and inductance after packaging.

There was insufficient yield among the undulator devices to measure the impedance of a complete 50-period (100-pole) undulator side. Measurements of individual periods, however, yielded measurements of 137$\pm$1.0-mΩ resistance and 17.0$\pm$2.0-nH inductance at 100 kHz. These measurement agree well with the 137-Ω resistance and 17.7-nH inductance expected from 3-D FEM simulation.

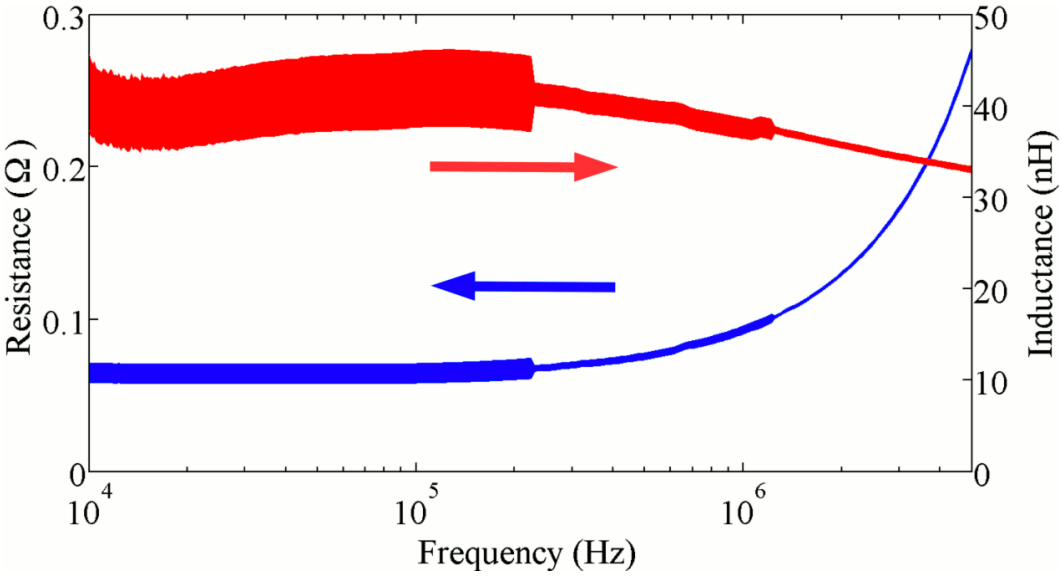

Figure 5.1: Measured resistance (blue) and inductance (red) of the 600-μm gap thick-film MEMS quadrupole between 10 kHz and 5 MHz before packaging (shown in Figure 4.17). Line thickness indicates measurement precision.

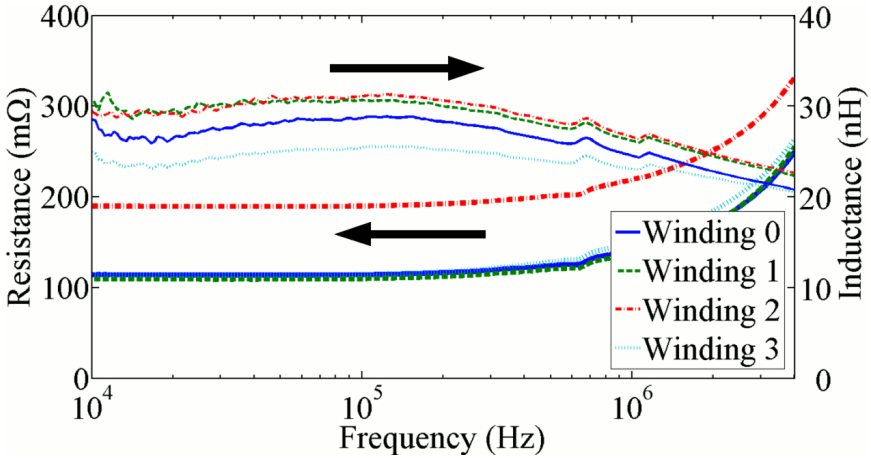

Figure 5.2: Measured resistance and inductance of the 4 electromagnets in the 600-μm gap thick-film MEMS quadrupole between 10 kHz and 4 MHz after packaging (shown in Figure 4.17). Measurement precision below 200 kHz is limited to 10%.

5.2 Beam experiments

To demonstrate beam steering and focusing, the MEMS quadrupole was mounted in the path of an electron beam and powered in dipole or quadrupole configuration (Figure 5.3). By varying the electrical current in individual coils, the beam was focused or deflected. The magnetic field or field gradient at the transverse location of the beam in the electromagnet

could then be calculated from the change in beam location or beam shape.

The electron beam used in these experiments was generated using a sub-ps UV laser pulse illuminating a photocathode embedded in a static electric field (DC photogun). A solenoid electromagnet adjusts the beam focus exiting the photocathode, and a set of steering electromagnets adjusts position and angle during an 835 mm drift length to an experiment chamber. The chamber houses the MEMS quadrupole behind a pair of micrometer-mounted orthogonal 20-μm slits (Thorlabs S20R) that have been stripped of anodizing and iron oxide coatings to form an electron beam aperture. After another 115 mm drift length, an imaging system composed of a Chevron micro-channel plate (MCP) intensifier, phosphor screen, and cooled CCD camera (Hamamatsu Flash 2.8) records the beam position and shape.

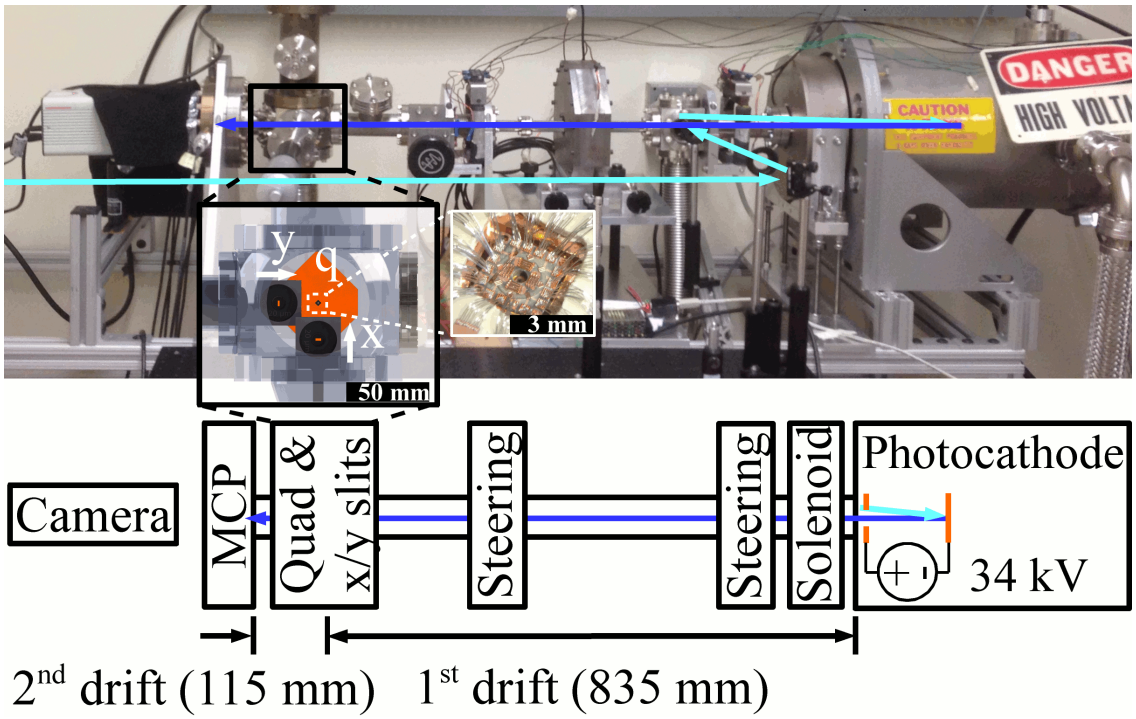

Figure 5.3: Photograph and illustration of the electron beam experiment. The black bordered inset illustration shows MEMS quadrupole fixture 'q' entering the chamber from above, vertical slit 'y' entering the chamber horizontally, and horizontal slit 'x' entering the chamber from below. The white bordered inset picture shows the MEMS quadrupole. Cyan arrows illustrate the UV laser path from left to right and blue arrows illustrate the electron beam path from right to left.

We acquired a background shot with the electron beam off for each image, which was subtracted from the data before calculating beam centroid and rms size. The experiment used

a slightly under-focused 34 keV sub-pC electron beam pulsed at 1 kHz repetition rate. The aperture was centered by switching the electromagnet on and off in quadrupole configuration and adjusting the position until the beam location did not change. Each measurement consisted of 25 images taken with 250 ms exposure time.

5.2.1 Electron beam transverse positioning

The transverse position of the electron beam in the electromagnet gap was controlled by two micrometer-mounted slits forming a 20 μm $\times$ 20 μm aperture. Before each experiment, the aperture was centered by switching the electromagnet on and off in quadrupole mode while adjusting the aperture position until there was no position change between the on and off state. This procedure is illustrated in Figure 5.4. Set up for experiments requiring a beam positioned off-axis started by centering the beam, then translating one slit of the electron beam aperture. Translating the aperture along the x-axis and y-axis is illustrated in Figure 5.5 and 5.6. Off-axis beam measurements recorded the beam position with the electromagnet off as the reference to avoid mechanical location uncertainty.

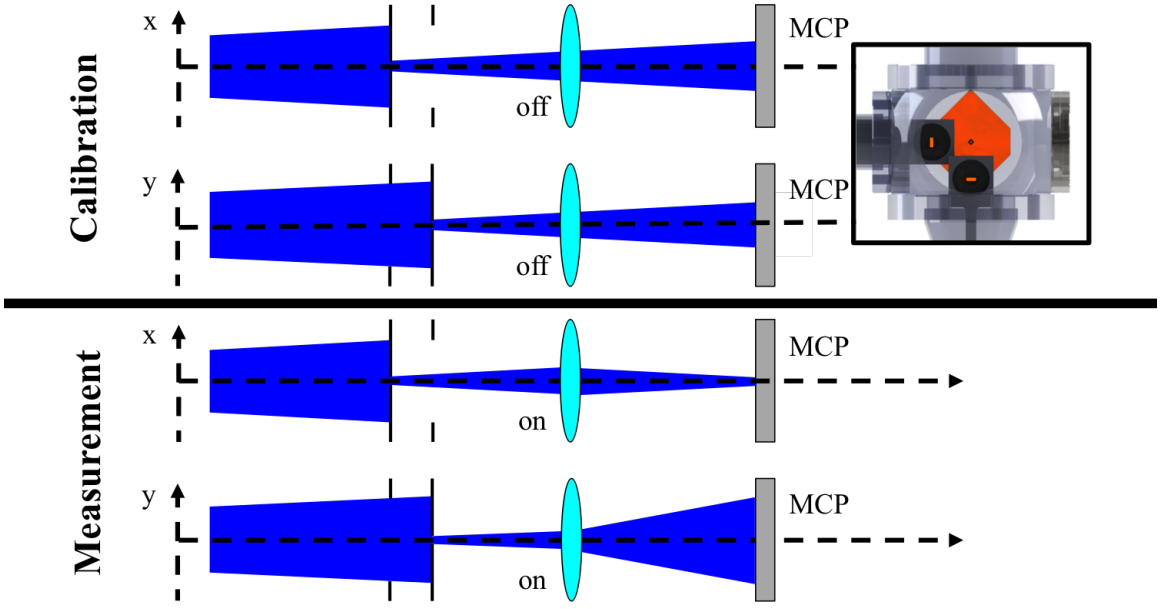

Figure 5.4: Illustration of the electron beam centering by translating the horizontal and vertical slits while switching the electromagnet on and off.

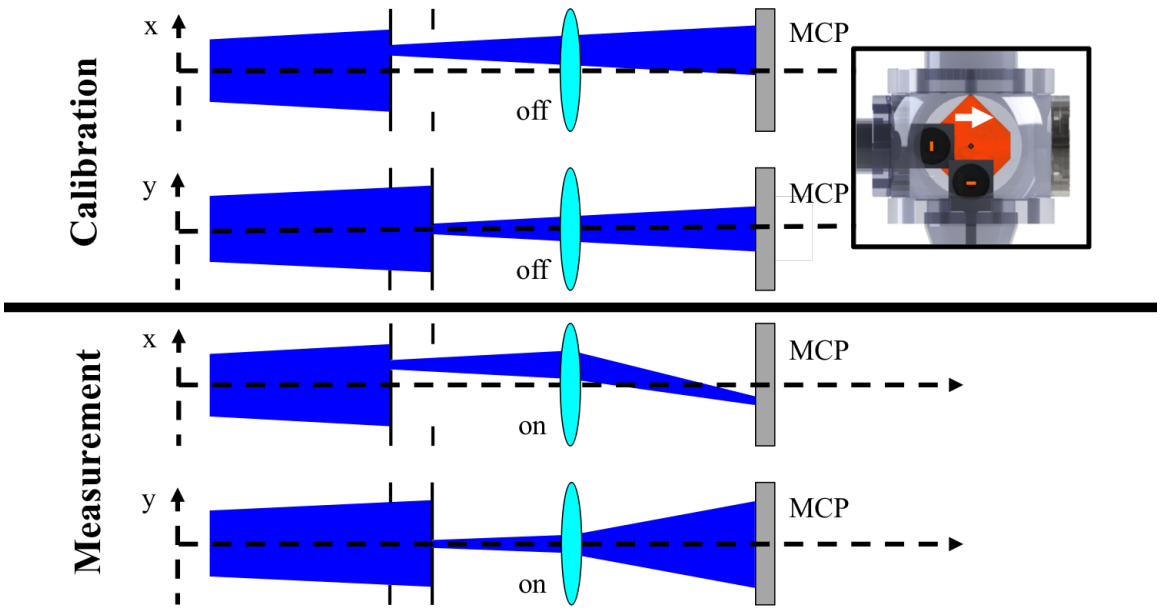

Figure 5.5: Illustration of the electron beam translated off-axis by moving the vertical slit along the x-axis.

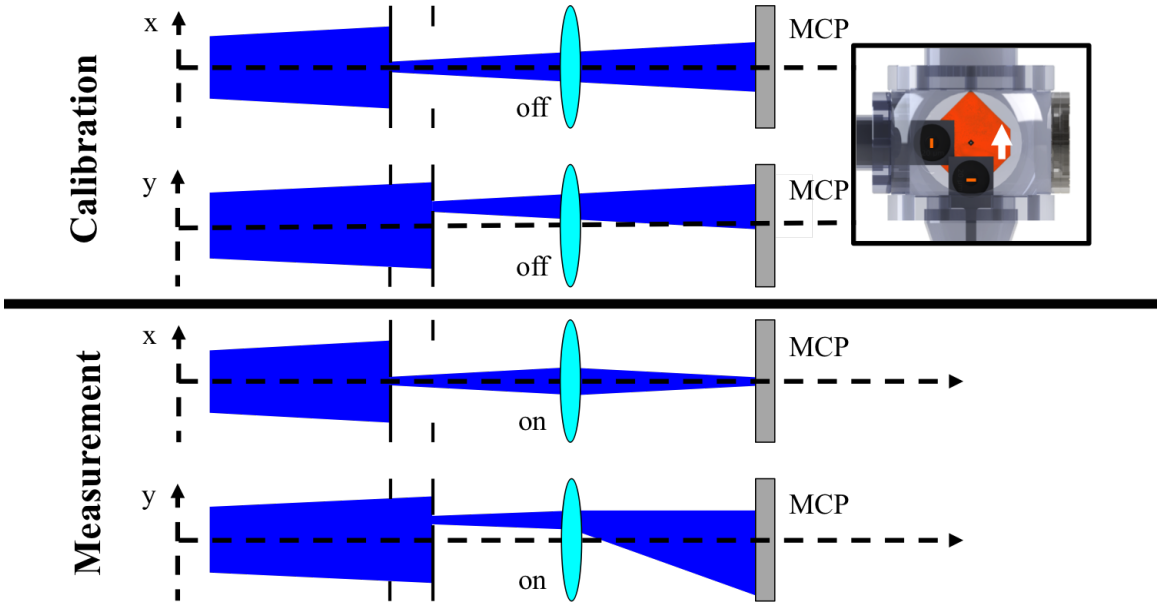

Figure 5.6: Illustration of the electron beam translated off-axis by moving the vertical slit along the y-axis.

5.2.2 Electron beam steering

To measure beam deflection performance, the electromagnet aperture was centered and current was stepped from -1.5 A to +1.5 A and back to -1.5 A in 0.5 A increments in an x-dipole field configuration and then repeated in a y-dipole configuration. Figure 5.7 shows the measured movement of the beam centroid with data from measurements back and forth along the x- and y-axis overlaid. The beam was deflected the same distance in each direction, indicating that the electromagnets were well matched. Less than 0.7% electromagnet hysteresis was measured, well within the experimental error, indicating that these electromagnets will not require compensation for their hysteresis during operation.

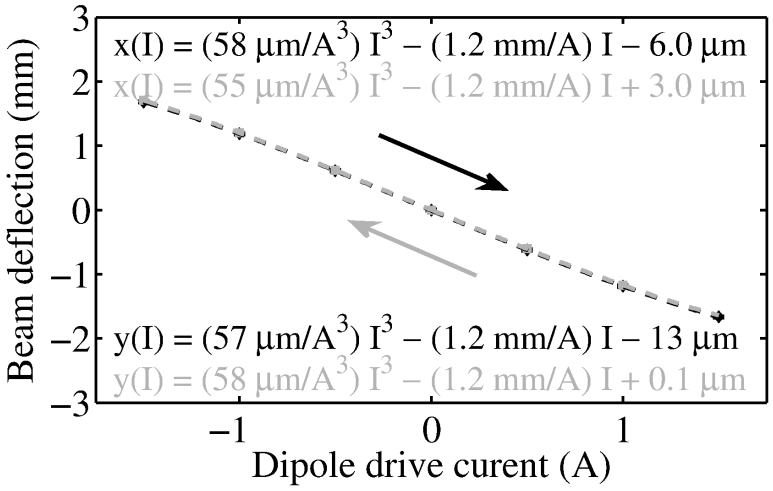

Figure 5.7: Measured beam deflection left, right, up and down across the MCP. Black deflection data was taken while increasing the current and grey data was taken while reducing the current. No hysteresis is visible from the measurements.

The experiment was repeated from -5.5 A to 5.5 A to explore electromagnet performance near saturation. Figure 5.8 shows the measured beam deflection and the field strength calculated from the measurements. Electromagnet saturation occurred between 2 A and 3 A drive current in dipole configuration and was expected at 2.35 A from simulation. The wirebonds in the electromagnet package failed at +5.5 A.

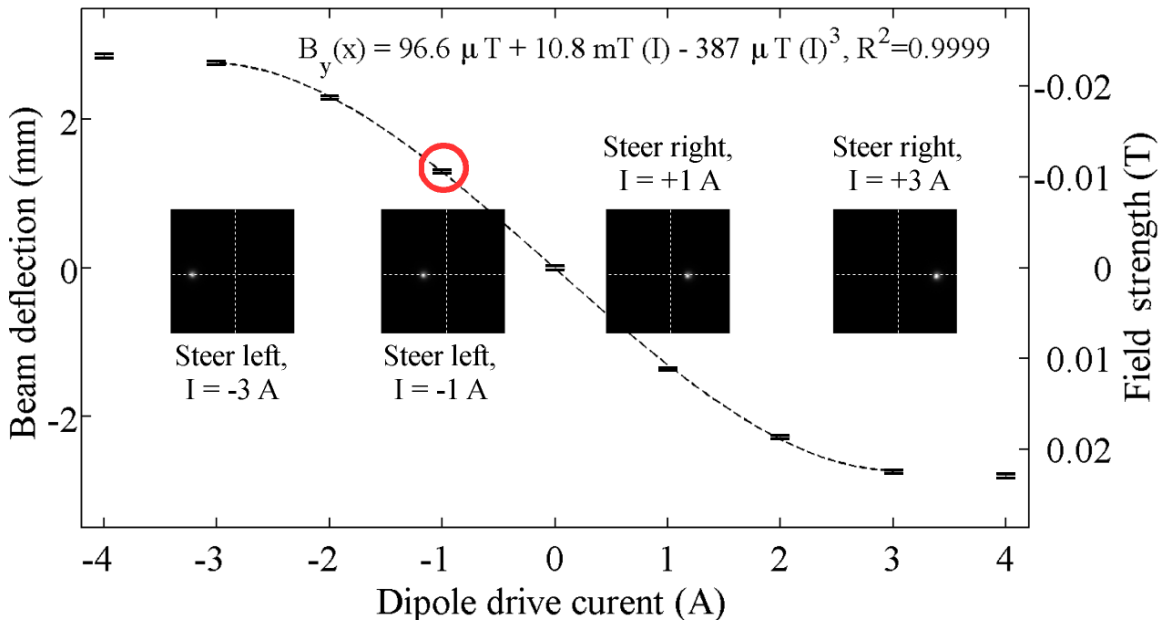

Figure 5.8: Electron beam steering experiment using a 4-pole electromagnet to deflect a 34-kV electron beam. Field strength assumes 686-μm magnetic length from FEM simulation at -1 A (the circled operating point). An equation fitting the field implied by the deflection data is shown.

5.2.3 Beam-probe field mapping

Field uniformity experiments were taken in quadrupole configuration from -1 A to 1 A current in 0.5 A increments. For each electromagnet current dataset, the aperture was stepped in equal intervals across the entire electromagnet bore in the horizontal direction and then in the vertical direction. The magnetic field was calculated from the measured electron beam deflection at each aperture position using Lorentz force and the normalized magnetic length from FEM simulation at -1 A quadrupole configuration drive current. Figure 5.9 and Figure 5.10 show the field calculated from beam deflection measurements across the horizontal and vertical transverse axis of the electromagnet.

The field gradient, shown in Figure 5.11, scales linearly and with hysteresis less than the measurement error. The difference between the horizontal and vertical field gradient could be due to poor control of the quadrupole electromagnet axis in the experiment chamber. The experiment setup obstructed observation of electromagnet orientation inside the chamber and the azimuth angle was hand-set to pass the beam. Simulations indicate that a 15° azimuth

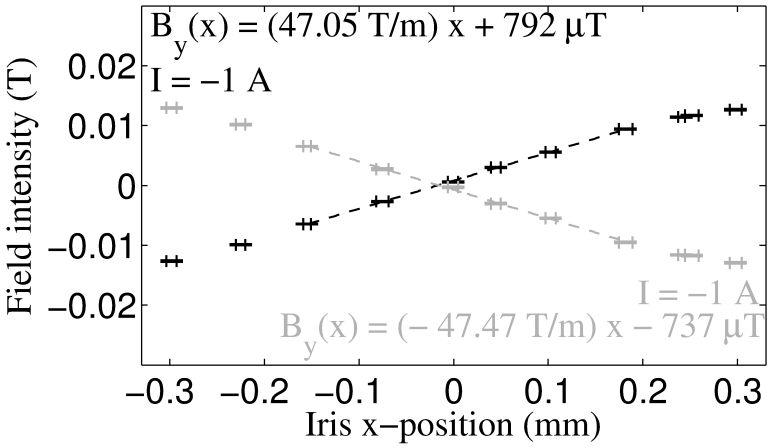

Figure 5.9: Measured x-axis transverse field profile measured with a 20 μm electron beam probe. Error bars and regression lines show the field across the center of the gap. 54 T/m gradients at 1 A are expected from FEM simulations.

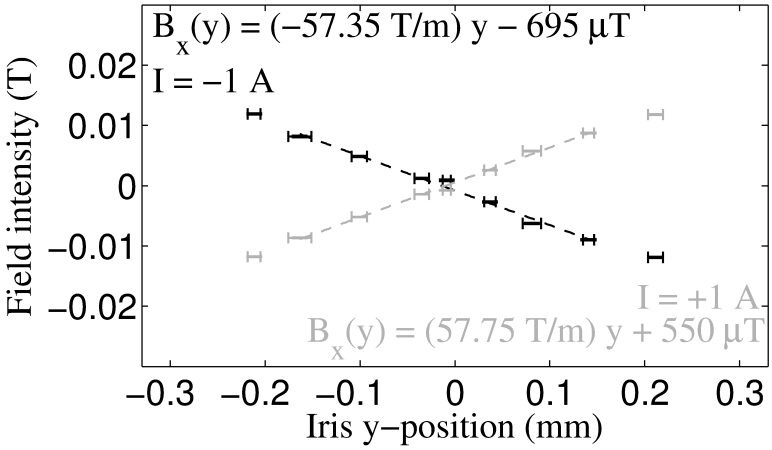

Figure 5.10: Measured y-axis transverse field profile measured with a 20 μm electron beam probe. Error bars and regression lines show the field across the center of the gap. 54 T/m gradients at 1 A are expected from FEM simulations.

angle error would reduce the field gradient shown in Figure 5.9 from the 54 T/m to the 47 T/m calculated from the beam deflection measurements across the horizontal axis of the electromagnet. The 57 T/m field gradient calculated from measurements across the vertical axis could have resulted from slight mis-centering of the aperture before the measurement started.

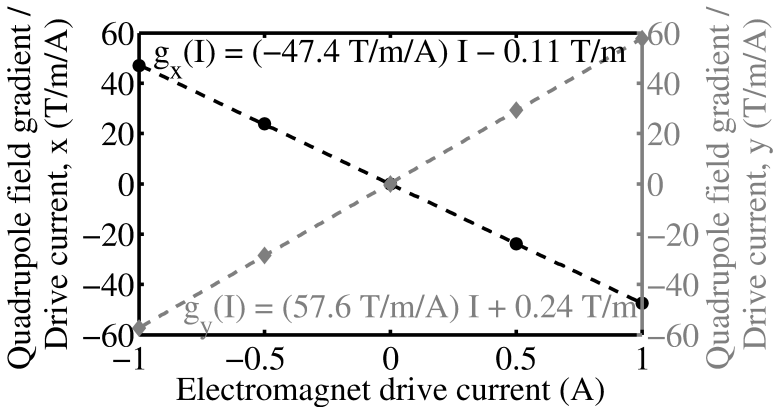

Figure 5.11: Transverse field gradient measured with a 20 μm electron beam probe. Gradient measured along the horizontal axis is black and measured along the vertical axis is gray.

5.2.4 Electron beam focusing

To measure the performance of the quadrupole focusing the beam, the electromagnet aperture was centered and the current was configured for quadrupole mode and stepped from -1.5 A to +1.5 A and back to -1.5 A in 0.1 A increments. The experiment setup is shown in Figure 5.12.

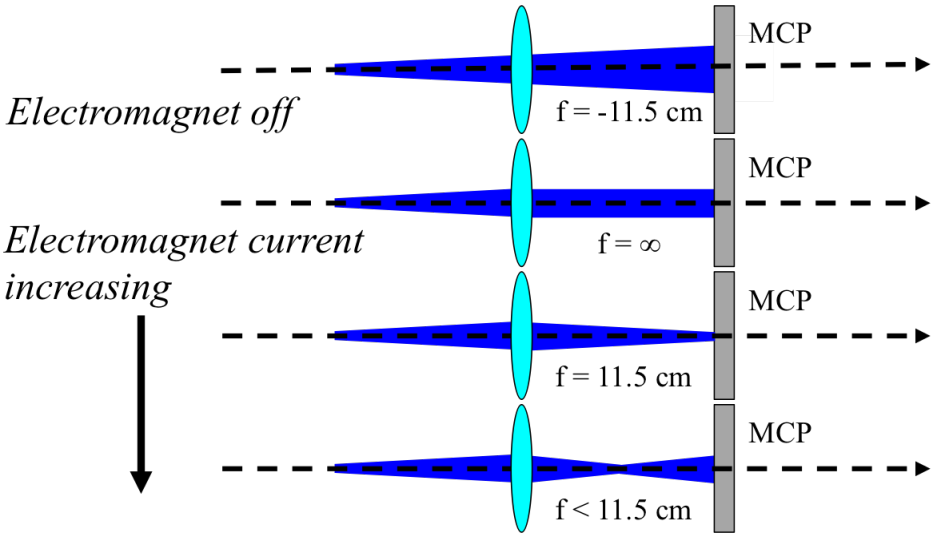

Figure 5.12: Illustration of the quadrupole focus sweep experiment.

The measured beam rms width is shown in Figure 5.13, and a focused beam waist is obtained at the MCP plane in the y-axis for I = 0.9 A and in the x-axis for I = -0.9 A. The

beam expands slightly between the first and second slit, resulting in the beam being slightly taller than wide at the quadrupole.

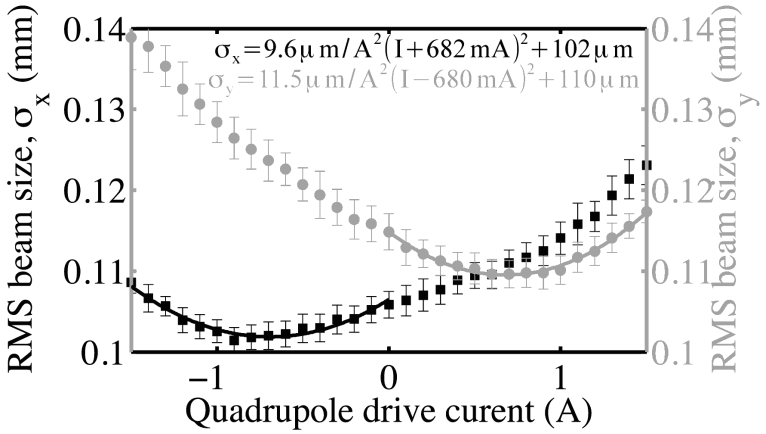

Figure 5.13: Beam width after focusing with the quadrupole electromagnet powered in quadrupole configuration. Horizontal rms width is black and vertical rms width is gray.

The field gradient plots can be used with the measured rms beam width at different focusing currents to show that the MEMS quadrupoles behave like regular beam optics and can be used for a quadrupole-scan measurement. Quadrupole-scan measurements are a method to extract the phase-space parameters of an electron beam at the quadrupole entrance from measurements at a fixed focal plane.

Using the transfer matrix of a thin quadrupole lens of focal distance f and drift length l_d between the quadrupole and MCP screen,

$$\begin{pmatrix} x \\ x' \end{pmatrix}_{\text{final}} = \begin{bmatrix} 1 & l_d \\ 0 & 1 \end{bmatrix} \begin{bmatrix} 1 & 0 \\ 1/f & 1 \end{bmatrix} \begin{pmatrix} x \\ x' \end{pmatrix}_{\text{initial}},$$

we can write for the final rms beam size $\sigma_x^2 = \text{var}(x_{\text{final}})$:

$$\sigma_{x,f}^2 = (1 - \frac{l_d}{f})^2 \sigma_{x,i}^2 + l_d^2 \sigma_{x',i}^2 + 2l_d(1 - \frac{l_d}{f})\sigma_{xx',i}.$$

The beam parameters at the quadrupole from the fit of the data yield $\sigma_x = 17$ μm, $\sigma_y = 21$ μm, $\sigma_{x'} = 0.9$ mrad, and $\sigma_{y'} = 1.0$ mrad in good agreement with the beam parameters

expected following the 20 μm aperture, validating our model for the MEMS quadrupole performance.

CHAPTER 6

Future work

MANY EXPERIMENTS demonstrating the unique performance of MEMS particle beam optics have not yet been carried out. Experiments using the Photoelectron Generated Amplified Spontaneous Radiation Source (PEGASUS) in the UCLA Particle Beam Physics Laboratory (PBPL), shown in Figure 6.1, rather than the 100 kV DC-photogun will enable state-of-the-art control of the electron beam in both time and phase-space for these experiments at the relativistic beam energies relevant to applications in electron-beam-based light sources.

6.1 High-speed focusing experiment

Experiments demonstrating the higher operating frequency or faster magnetic field response enabled by MEMS focusing and deflecting optics could lead to fast beam-dither stages for transmission electron microscopes or kicker beam extraction magnets in synchrotrons that minimally affect the circulating beam. A proof of principle experiment using the Pegasus accelerator in PBPL will reproduce the experimental conditions of the quadrupole demonstrated with the DC-photogun, but with 4 MeV electrons and controlled phase between the electron bunch and the MEMS quadrupole focusing current pulse. By stepping through 180° relative phase at pulse widths between 1 s and 1 μs, the frequency response of the quadrupole electromagnet will be experimentally demonstrated.

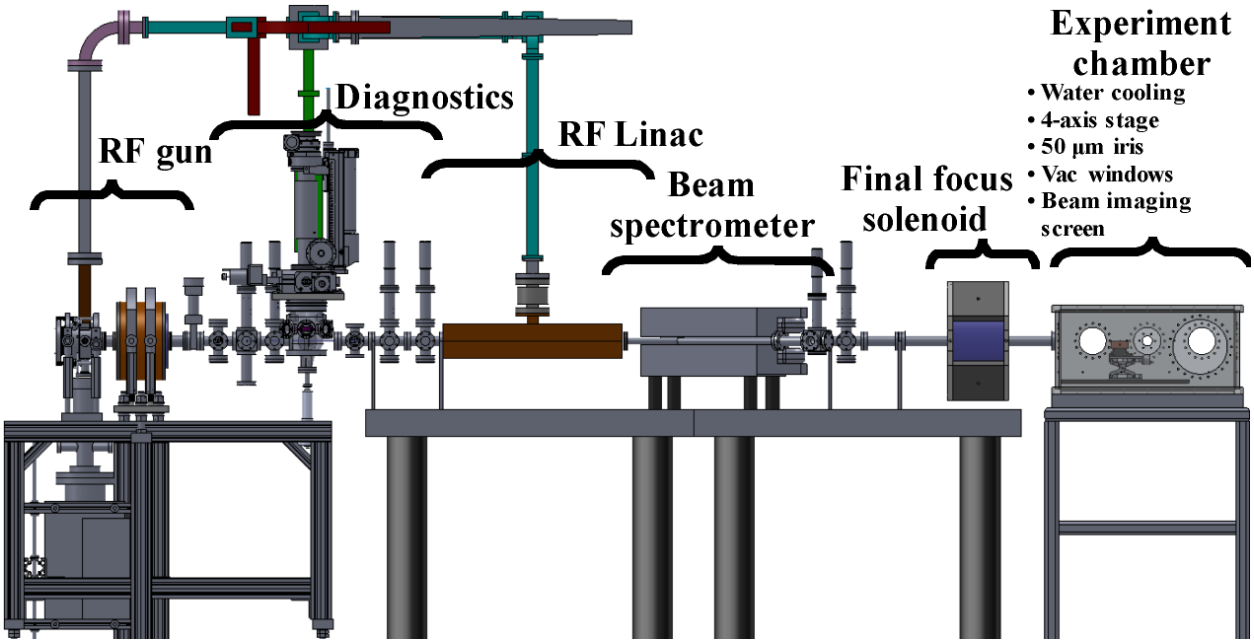

Figure 6.1: Illustration of the PEGASUS beamline and undulator radiation experiment.

6.2 Undulator radiation experiments

Several proof-of-principle experiment aimed at demonstrating the feasibility of coupling a high brightness electron beam in the small gap of a prototype surface-micromachined 100 μm period microundulator are possible using the Pegasus accelerator in PBPL. A 50 period undulator with 800 μm period length (4 cm total length) and 1 T_{peak} transverse magnetic field will be fabricated in the UCLA Nanoelectronics Research Facility and tested using the ultra-small emittance beam available at the Pegasus RF photoinjector. The Pegasus beamline is described elsewhere [MMG09].

The parameters of the beam are listed in Table 6.1. Preliminary tests show that the 4 MeV 10 pC electron beam can be focused down to a 18 μm spot size. With 0.1 mm-mrad normalized beam emittance, the beta function is 2.5 cm. The goal of the first experiments are detection of spontaneous undulator radiation at 863 nm from the MEMS fabricated undulator. This is a very convenient range in the electromagnetic spectrum, since diagnostics in the visible are very sensitive and easily available. Even though the energy estimated for spontaneous radiation in these conditions will be weak (only few thousands of visible/IR pho-

Table 6.1: Parameters of the microundulator experiment at the Pegasus beamline

E-beam energy	11 MeV
E-beam peak current	100 Amp
Beam emittance	0.1 mm-mrad
Undulator period	800 μm
Undulator gap	200 μm
Peak magnetic field	1 T
K (rms)	0.1
N_u	50
Undulator length	4 cm
λ_r	863 nm
E_r	1.43 eV

ton generated), we will be able to use intensified CCD cameras with single photon detection capabilities to characterize the radiation.

Another feasible experiment will be to use the 800 nm Ti:Sa laser system available in the Pegasus laboratory to microbunch the 4 MeV beam at 800 nm with a seed radiation pulse. This is an application for which microundulators might be uniquely suited. Currently, there is no way to efficiently couple a low energy electron beam and an optical or near infrared laser. The period of conventional undulator magnets is too long to tune at the resonance condition and harmonic coupling coefficients quickly decrease in amplitude with increasing harmonic number. This coupling can be used to diagnose and manipulate the longitudinal phase space of low energy beams at the optical scale. Coupling this scheme with recent ideas on longitudinal space charge amplification [SY10], which naturally works better at lower beam energy, might open a path towards a new kind of radiation source.

CHAPTER 7

Conclusion

THIS PROJECT demonstrated the first application of magnetic MEMS to focusing and steering electromagnets for charged particle beams. A 600-μm magnetic gap 4-pole electromagnet was designed, fabricated, and tested with a 34 keV electron beam, demonstrating digitally controlled steering and focusing.

The performance of these magnetic optics improves considerably as size is reduced into the micro-scale. Simple scaling of the prototype results presented in this work indicated that multi-kT/m gradients can be obtained using MEMS fabrication techniques. Such MEMS quadrupoles hold the potential to revolutionize the field of charged particle optics with a wide range of applications including electron microscopes and compact light sources.

Undulators with magnetic gap and undulator period in the range of 100 μm were designed and a compatible fabrication process was developed. This period range is presently not covered by other undulator technology and is very attractive since it bridges the gap between traditional permanent magnet undulators and laser undulators employed in inverse Compton scattering sources.

APPENDIX A

Experiment data processing scripts

Images of the MCP from the beam experiments were recorded with a matlab script that recorded the experimental parameters in the image filename. The images were sorted into directories corresponding to each experiment type (deflection, focusing, field characterization), and the quadImageProcess() script was run on the directory to extract measurement metadata from the images.

The plotQuadData() and plotDipoleData() scripts were run with the processed metadata input to plot the measurement results.

A.1 Beam data pre-processing MATLAB script

```
function [files] = quadImageProcess(directory)
% [files] = quadImageProcess(pwd())
%
% Old experiment is 133 microns / pixel
% Old experiment is 16.5 cm from the MCP
%
% New experiment is is 40 microns / pixel
%
% New MCP setup is closer to the quadrupole
%
% NOTE: Focusing statistics are only for changes to the x and y axis.
% Anything at a different angle, such as 2 electromagnets being driven, will
% not process unless rotateOn is set to 1 and the commented code is
% modified to accommodate the change at imrotate( ...
%
% cSum = [files.c1]+[files.c3];
% cDiff = [files.c1]-[files.c3];
% centroidX = [files.centroidX];
% centroidY = [files.centroidY];
```

```
% majorAxis = [files.majorAxis];
% minorAxis = [files.minorAxis];
% orientation = [files.orientation];
%
% New additions!
% uniformityTest = 0; processes the data with a fixed iris
% uniformityTest = 1; processes the data with to orthogonal moving slits.
% This adds two new double precision variables to the 'files' structure,
% irisX and irisY. irisX is the x-axis position (converted to meters) of
% the vertical slit and irisY is the y-axis position of the horizontal
% slit. The November26 experiment (data taken December 5 after stripping
% the insulating films off of the x and y iris) uses 20 micron slits. Slit
% 1 is 26 microns and is the x-moving vertical slit. Slit 2 is 23.5 microns
% and and is the y-moving horizontal slit.

%% Processing parameters
rotateOn = 0;
uniformityTest = 0;
%calibration data (meters/step) for the y-moving horizontal slit.
%Taken from StepperCalibration.xlsx
slit2Step = 286.3e-6/5000;

%% Parsing parameters
delimiter = '_';

%% Get file names
files = dir(directory);

%% Parse file names
fprintf(['Parsing file names in ' directory ' to metadata...']);
%list of position reference files with the form:[... ; X Y fileIndex ; ...]
posReferenceList = [];
for fileIndex = 1:length(files)
    delimiters = 0;
    for parseIndex = 1:length(files(fileIndex).name);
        if (strcmp(files(fileIndex).name(parseIndex),delimiter))
            delimiters = [delimiters parseIndex];
        end
    end
    if strcmp(files(fileIndex).name,'Background.bmp')
        files(fileIndex).isFile = 1;
        files(fileIndex).isBackground = 1;
    elseif length(delimiters)>3%First delimiter is set at 1.
        if exist('item')
            clear('item')
```

```
end
for delimiterIndex = 1:length(delimiters)-1
    item(delimiterIndex) = ...
        {files(fileIndex).name(delimiters(delimiterIndex)+...
        1:delimiters(delimiterIndex+1)-1)};
end
files(fileIndex).c0 = 0;
files(fileIndex).c1 = 0;
files(fileIndex).c2 = 0;
files(fileIndex).c3 = 0;
files(fileIndex).mc0 = 0;
files(fileIndex).mc1 = 0;
files(fileIndex).mc2 = 0;
files(fileIndex).mc3 = 0;
files(fileIndex).isFile = 1;
files(fileIndex).isBackground = 0;
files(fileIndex).isPosReference = 0;
files(fileIndex).offsetX = 0;
files(fileIndex).offsetY = 0;
files(fileIndex).slitX = 0;
files(fileIndex).slitY = 0;
files(fileIndex).exposureTime = .1;
files(fileIndex).MeasurementNumber = 1;
files(fileIndex).posReferenceIndex = 0;
files(fileIndex).posReferenceUsed = 0;
files(fileIndex).SNR = 0;
for itemIndex = 1:length(item)
    if strcmp(item{itemIndex},'c0')
        files(fileIndex).c0 = str2num(item{itemIndex+1});
    elseif strcmp(item{itemIndex},'c1')
        files(fileIndex).c1 = str2num(item{itemIndex+1});
    elseif strcmp(item{itemIndex},'c2')
        files(fileIndex).c2 = str2num(item{itemIndex+1});
    elseif strcmp(item{itemIndex},'c3')
        files(fileIndex).c3 = str2num(item{itemIndex+1});
    elseif strcmp(item{itemIndex},'mc0')
        files(fileIndex).mc0 = str2num(item{itemIndex+1});
    elseif strcmp(item{itemIndex},'mc1')
        files(fileIndex).mc1 = str2num(item{itemIndex+1});
    elseif strcmp(item{itemIndex},'mc2')
        files(fileIndex).mc2 = str2num(item{itemIndex+1});
    elseif strcmp(item{itemIndex},'mc3')
        files(fileIndex).mc3 = str2num(item{itemIndex+1});
    elseif strcmp(item{itemIndex},'beamOff') || ...
            strcmp(item{itemIndex},'BeamOff') || ...
```

```
                strcmp(item{itemIndex},'Off')
            files(fileIndex).isBackground = 1;
        elseif strcmp(item{itemIndex},'beamOn') || ...
                strcmp(item{itemIndex},'BeamOn') || ...
                strcmp(item{itemIndex},'On')
            files(fileIndex).isBackground = 0;
        elseif strcmp(item{itemIndex},'roi')
            files(fileIndex).offsetX = str2num(item{itemIndex+1});
            files(fileIndex).offsetY = str2num(item{itemIndex+2});
        elseif strcmp(item{itemIndex},'window')
            files(fileIndex).offsetX = str2num(item{itemIndex+1});
            files(fileIndex).offsetY = str2num(item{itemIndex+2});
        elseif strcmp(item{itemIndex},'slitX');
            files(fileIndex).slitX = str2num(item{itemIndex+1})/1e6;
        elseif strcmp(item{itemIndex},'slitY');
            files(fileIndex).slitY = str2num(item{itemIndex+1})/1e6;
            if ~files(fileIndex).c0 && ~files(fileIndex).c1 && ...
                    ~files(fileIndex).c2 && ~files(fileIndex).c3 && ...
                    ~files(fileIndex).isBackground
                files(fileIndex).isPosReference = 1;
                posReferenceList = [posReferenceList;...
                    [files(fileIndex).slitX,files(fileIndex).slitY,...
                    fileIndex]];
            end
        elseif strcmp(item{itemIndex},'exp')
            files(fileIndex).exposureTime = ...
                .001*str2num(item{itemIndex+1});
        elseif strcmp(item{itemIndex},'rep')
            files(fileIndex).MeasurementNumber = ...
                str2num(item{itemIndex+1});
        elseif strcmp(item{itemIndex},'Is')
            files(fileIndex).solenoidCurrent = ...
                str2num(item{itemIndex+1});
        end
    end
elseif length(delimiters)>2 && length(delimiters)<5
    for delimiterIndex = 1:length(delimiters)-1
        item(delimiterIndex) = ...
            {files(fileIndex).name(delimiters(delimiterIndex)+...
            1:delimiters(delimiterIndex+1)-1)};
    end
    files(fileIndex).isFile = 1;
    files(fileIndex).isBackground = 0;
    files(fileIndex).c1 = str2num(item{1});
    files(fileIndex).c3 = str2num(item{2});
```

```
    else
        files(fileIndex).isBackground = 0;
        files(fileIndex).isFile = 0;
    end
end
fprintf('\n');
referenceIndex = [];
deleteIndex = [];
fprintf('Parsing file metadata...\n');
for fileIndex = 1:length(files)
    if files(fileIndex).isFile
        info = imfinfo([directory '/' files(fileIndex).name]);
        try
            %NECESSARY for threshold processing
            files(fileIndex).depth = info.NumColorsUsed;
        catch
            files(fileIndex).depth = 2^(info.BitDepth);
        end
        if files(fileIndex).isBackground
            referenceIndex = [referenceIndex fileIndex];
        end
    else
        deleteIndex = [deleteIndex fileIndex];
    end
end

fprintf('Parsing background reference image metadata...\n');
index = 1;
for index = 1:length(referenceIndex)
    referenceImage(index).data = ...
        imread([directory '/' files(referenceIndex(index)).name]);
    referenceImage(index).sizeX = size(referenceImage(index).data,1);
    referenceImage(index).sizeY = size(referenceImage(index).data,2);
    referenceImage(index).offsetX = files(referenceIndex(index)).offsetX;
    referenceImage(index).offsetY = files(referenceIndex(index)).offsetY;
    referenceImage(index).exposureTime = ...
        files(referenceIndex(index)).exposureTime;
    index = index+1;
end
if uniformityTest == 1
    fprintf('Parsing position refence image metadata...\n');
    index=1;
    for index = setxor(1:length(files),posReferenceList(:,3))'
        if files(index).isFile
            for posIndex = posReferenceList(:,3)'
```

```
                if files(index).slitX == files(posIndex).slitX && ...
                        files(index).slitY == ...
                        files(posIndex).slitY && ...
                        ~files(index).posReferenceIndex && ...
                        ~(files(posIndex).posReferenceUsed== ...
                        files(index).c0)
                    %May need to be modified when there are multipole
                    %position references (passed 0 multiple times)
                    files(index).posReferenceIndex = posIndex;
                    %Files will be sorted in this list, so this should keep
                    %the same image from being used by multiple repitions
                    %of the same current.
                    files(posIndex).posReferenceUsed = files(index).c0;
                end
            end
            %What if it doesn't find a reference file? It'll return -0- for
            %.posReferenceIndex and cause a problem in plotQuadData2.
            if ~files(index).posReferenceIndex && files(index).c0
                fprintf([...
                    '   Error: no position reference found for file\n'...
                    '   ' files(index).name '\n'])
            end
        end
    end
end

clear('item','index','fileIndex','delimiters','delimiterIndex',...
    'delimiter','info','parseIndex','referenceImageIndex','posIndex');


%% Process the images for centroid location, minor axis, major axis,
%and ellipse orientation

% intensity ratio at **two** standard deviations from the centroid
% One standard deviation is pretty close to the centroid (couple pixels)
threshold(1) = exp(-1);
threshold(2) = exp(-4/2);
threshold(3) = exp(-9/3);
threshold(4) = exp(-16/4);

threshSelect = 2;% How many standard deviations for measurement?
threshMeasure = 1;

for fileIndex = 1:length(files)
    fprintf(['Processing ' files(fileIndex).name ', ' num2str(fileIndex)...
```

```
    ' of ' num2str(length(files)) '... \n']);
if files(fileIndex).isFile && ~files(fileIndex).isBackground
    % Remove background noise and damage to the MCP & CCD from the
    % image.
    files(fileIndex).image = ...
        imread([directory '/' files(fileIndex).name]);
    files(fileIndex).proc = files(fileIndex).image;
    usableReference = [];
    for referenceImageIndex = 1:length(referenceImage)
        if (size(files(fileIndex).proc,1) == ...
                referenceImage(referenceImageIndex).sizeX && ...
                size(files(fileIndex).proc,2) == ...
                referenceImage(referenceImageIndex).sizeY && ...
                files(fileIndex).offsetX == ...
                referenceImage(referenceImageIndex).offsetX && ...
                files(fileIndex).offsetY == ...
                referenceImage(referenceImageIndex).offsetY && ...
                files(fileIndex).exposureTime == ...
                referenceImage(referenceImageIndex).exposureTime)
            usableReference = [usableReference referenceImageIndex];
        end
    end
    try
        reference = ...
            single(zeros(referenceImage(usableReference(1)).sizeX,...
            referenceImage(usableReference(1)).sizeY));
    catch
        reference = single(zeros(size(files(fileIndex).proc,1),...
            size(files(fileIndex).proc,2)));
        files(fileIndex).noNormalization = 1;
    end
    for index = 1:length(usableReference)
        reference = reference + 1/length(usableReference)*...
            (single(referenceImage(usableReference(index)).data));
    end
    reference = uint16(reference);
    files(fileIndex).proc = files(fileIndex).proc - reference;
    files(fileIndex).threshSelect = im2bw(files(fileIndex).proc,...
        single(max(max(files(fileIndex).proc)))/...
        (files(fileIndex).depth-1)*threshold(threshSelect));
    [files(fileIndex).threshLabeled num]= ...
        bwlabel(files(fileIndex).threshSelect);
    stats = regionprops(files(fileIndex).threshLabeled,'centroid',...
        'MajorAxisLength','MinorAxisLength','Orientation','Area');
    [val,statIndex] = max([stats.Area]);
```

```
measureLocationX = round(stats(statIndex).Centroid(2));
measureLocationY = round(stats(statIndex).Centroid(1));
files(fileIndex).threshMeasure = im2bw(files(fileIndex).proc, ...
    single(max(max(files(fileIndex).proc(...
    measureLocationX,measureLocationY))))/ ...
    (files(fileIndex).depth-1)...
    *threshold(threshMeasure));
[files(fileIndex).threshLabeled num]= ...
    bwlabel(files(fileIndex).threshMeasure);
spotLocationX = stats(statIndex).Centroid(1);
spotLocationY = stats(statIndex).Centroid(2);
stats = regionprops(files(fileIndex).threshLabeled,'centroid',...
    'MajorAxisLength','MinorAxisLength','Orientation','Area');
statIndex = 0;
for index = 1:length(stats)
    if spotLocationX - 4 < stats(index).Centroid(1) && ...
        stats(index).Centroid(1) < spotLocationX + 4 && ...
        spotLocationY - 4 < stats(index).Centroid(2) && ...
        stats(index).Centroid(2) < spotLocationY + 4
    statIndex = index;
    end
end
if statIndex
    files(fileIndex).area = stats(statIndex).Area;
    files(fileIndex).centroidX = stats(statIndex).Centroid(1);
    files(fileIndex).centroidY = stats(statIndex).Centroid(2);
    files(fileIndex).majorAxis = stats(statIndex).MajorAxisLength;
    files(fileIndex).minorAxis = stats(statIndex).MinorAxisLength;
    %Angle coutnerclockwise from the x-axis
    files(fileIndex).orientation = stats(statIndex).Orientation;
    % Rotate image by stats.orientation and perform a gaussian fit
    beamSpotWindow = 20;%(20 makes 41x41, 25 makes 51x51)
    if round(files(fileIndex).centroidY-beamSpotWindow) < 1
        beamSpotWindow = round(files(fileIndex).centroidY)-1;
    end
    if round(files(fileIndex).centroidY+beamSpotWindow) > ...
            size(files(fileIndex).proc,1)
        beamSpotWindow = size(files(fileIndex).proc,1)-...
            round(files(fileIndex).centroidY)-1;
    end
    if round(files(fileIndex).centroidX-beamSpotWindow) < 1
        beamSpotWindow = round(files(fileIndex).centroidX)-1;
    end
    if round(files(fileIndex).centroidX+beamSpotWindow) > ...
            size(files(fileIndex).proc,2)
```

```
    beamSpotWindow = size(files(fileIndex).proc,2)-...
        round(files(fileIndex).centroidX)-1;
end
%Check again to make sure that it isn't in the corner.
if round(files(fileIndex).centroidY-beamSpotWindow) < 1
    beamSpotWindow = round(files(fileIndex).centroidY)-1;
end
if round(files(fileIndex).centroidY+beamSpotWindow) > ...
        size(files(fileIndex).proc,1)
    beamSpotWindow = size(files(fileIndex).proc,1)-...
        round(files(fileIndex).centroidY)-1;
end
if round(files(fileIndex).centroidX-beamSpotWindow) < 1
    beamSpotWindow = round(files(fileIndex).centroidX)-1;
end
if round(files(fileIndex).centroidX+beamSpotWindow) > ...
        size(files(fileIndex).proc,2)
    beamSpotWindow = size(files(fileIndex).proc,2)-...
        round(files(fileIndex).centroidX)-1;
end

edge1 = round(files(fileIndex).centroidY-beamSpotWindow);
files(fileIndex).edge1 = edge1;
edge2 = round(files(fileIndex).centroidY+beamSpotWindow);
files(fileIndex).edge2 = edge2;
edge3 = round(files(fileIndex).centroidX-beamSpotWindow);
files(fileIndex).edge3 = edge3;
edge4 = round(files(fileIndex).centroidX+beamSpotWindow);
files(fileIndex).edge4 = edge4;
if edge1 < 1 || edge3 < 1 || ...
        edge2 > size(files(fileIndex).proc,1) || ...
        edge4 > size(files(fileIndex).proc,2)
    deleteIndex = [deleteIndex fileIndex];
    fprintf(['   Dumping ' files(fileIndex).name ', ' ...
        num2str(fileIndex) ' of ' num2str(length(files)) ...
        ' (bounds:' num2str(edge1) ',' num2str(edge2) ',' ...
        num2str(edge3) ',' num2str(edge4) ')\n'])
else
    beamSpot =(files(fileIndex).proc(edge1:edge2,edge3:edge4));
    if rotateOn
        beamSpotProc = imrotate(beamSpot,...
            mod(90,files(fileIndex).orientation),...
            'bicubic','crop');
    else
        beamSpotProc = beamSpot;
```

```
            end
            beamSpotCSx = beamSpotProc(:,1+beamSpotWindow);
            files(fileIndex).beamSpotCSx = beamSpotCSx;
            beamSpotCSy = beamSpotProc(1+beamSpotWindow,:);
            files(fileIndex).beamSpotCSy = beamSpotCSy;
            %Integrate across image for increased SNR
            beamSpotIntX = sum(beamSpotProc,1);
            files(fileIndex).beamSpotIntX = beamSpotIntX;
            beamSpotIntY = sum(beamSpotProc,2);
            files(fileIndex).beamSpotIntY = beamSpotIntY;
            %Set up fitting initial parameters.
            minFx = min(beamSpotIntX);
            maxFx = max(beamSpotIntY);
            minFy = min(beamSpotIntX);maxFy = max(beamSpotIntY);
            ezfitFunX = ['y = a*exp(-((x-x_0)^2)/(2*sigma^2))+y0;a='...
                num2str(maxFx-minFx) ';x_0=' ...
                num2str(round(length(beamSpotIntX)/2)+1) ...
                ';sigma=3;y0=' num2str(minFx)];
            ezfitFunY = ['y = a*exp(-((x-x_0)^2)/(2*sigma^2))+y0;a='...
                num2str(maxFy-minFy) ';x_0=' ...
                num2str(round(length(beamSpotIntY)/2)+1) ...
                ';sigma=3;y0=' num2str(minFy)];
            %Fit offset gaussian to beam spot shape.
            Fx = ezfit(beamSpotIntX,ezfitFunX);
            Fy = ezfit(beamSpotIntY,ezfitFunY);
            files(fileIndex).fitIntX = Fx;
            files(fileIndex).fitIntY = Fy;
            if files(fileIndex).fitIntX.r < 0.95
                deleteIndex = [deleteIndex fileIndex];
                fprintf(['   Dumping ' files(fileIndex).name ', ' ...
                    num2str(fileIndex) ' of ' num2str(length(files))...
                    ' (fit R = ' num2str(files(fileIndex).fitIntX.r)...
                    ')\n']);
            elseif files(fileIndex).fitIntY.r < 0.95
                deleteIndex = [deleteIndex fileIndex];
                fprintf(['   Dumping ' files(fileIndex).name ', ' ...
                    num2str(fileIndex) ' of ' num2str(length(files))...
                    ' (fit R = ' num2str(files(fileIndex).fitIntX.r)...
                    ')\n']);
            end
            %Fit gaussian to beam spot shape.
            Fx = ezfit(single(beamSpotCSx),...
'y = a*exp(-((x-x_0)^2)/(2*sigma^2))+y0;a=500;x0=21;sigma=20;y0=50');
            Fy = ezfit(single(beamSpotCSy),...
'y = a*exp(-((x-x_0)^2)/(2*sigma^2))+y0;a=500;x0=21;sigma=20;y0=50');
```

```
                files(fileIndex).fitCSX = Fx;
                files(fileIndex).fitCSY = Fy;
                files(fileIndex).SNR = max(max(...
                    files(fileIndex).proc(edge1:edge2,edge3:edge4)))/ ...
                    mean(mean(files(fileIndex).proc([1:edge1 edge2:end],...
                    [1:edge3 edge4:end])));
            end
        else
            deleteIndex = [deleteIndex fileIndex];
            fprintf(['   Dumping ' files(fileIndex).name ', ' ...
                num2str(fileIndex) ' of ' num2str(length(files))...
                ' (centroid)\n'])
            files(fileIndex).area = NaN;
            files(fileIndex).centroidX = NaN;
            files(fileIndex).centroidY = NaN;
            files(fileIndex).majorAxis = NaN;
            files(fileIndex).minorAxis = NaN;
            files(fileIndex).orientation = NaN;
            if files(fileIndex).exposureTime ~= 0.001
                'stop temporarily and inspect';
            end
        end
    end
end

save([directory '/filesNew.mat'],'files');

deleteIncrement = 1;
deleteArray = unique([deleteIndex referenceIndex]);
if uniformityTest
    % Update index references to relative position files and delete.
    for index = deleteArray
        for index2 = index:length(files)
            files(index2).posReferenceIndex = ...
                files(index2).posReferenceIndex-1;
        end
    end
end
%clear this file from the array
files(unique([deleteIndex referenceIndex])) = [];
clear('lastfit');
save([directory '/filesNew.mat'],'files');
fprintf(['Finished ' directory '.\n']);
```

A.2 Beam-steering data processing MATLAB script

```
function [files] = plotQuadData2(files)
% [plotData,focusMajorMean,focusMajorStd,...
%     focusMinorMean,focusMinorStd,FocusMajorSubMinorMean,...
%     focusMajorSubMinorStd]

%% Data handling parameters

manualCheck     = 0;
automaticCheck  = 0;
uniformityTest  = 0;
imageCenteredOn = 0;
imageUncenteredOn= 1;

%% Fundamental parameters

%Electron properties
e0              = -1.60217646e-19;  %C
m0              = 9.10938188e-31;   %kg
Ebeam           = 34e3;
restmass        = 510998.93;%eV
%Fundamental constants
c               = 299792458;        %m/s
h               = 6.626068e-34;     %m^2*kg/s
eps0            = 8.85418782e-12;   %F/m;
mu0             = 1.25663706e-6;    %H/m
gamma           = Ebeam./restmass+1;%absolute
beta            = sqrt(1-1./gamma.^2);%absolute
%MCP Pixel Size (10/22/13)
pixelSize       = 57.15e-3/(1725-358); % From MCP_pixelsize.png
MCP_distance    = 11.5e-2;%From Evan
magLengthDipole = 686e-6;
magLengthQuad   = magLengthDipole;

%% Deflection statistics sorting
fprintf(['Drive current data: ' num2str(unique([files.c0])) '\n'])
focusCurrent = [-4000:1000:4000];
%slitXLoc = unique([files.slitX]);
%slitYLoc = unique([files.slitY]);
exposureTimeCheck = .05; % s
solenoidCurrentCheck = 2080; %mA
imageRep = [1];
roiXsel = [1070];
slitSel = unique([files.slitX]);
```

```
exemptionIndex = [5 0];
exemptionSelection = [2];
exemptionCounter = 1;

%Pick out the index of the dipole data
transportIndex = [];
transportIndexIndex = 0;
fprintf('Finding quadruple data');
if uniformityTest
    dataLength = length(slitSel);
    for dataIndex = 1:dataLength
        fprintf('.');
        tempIndex = find([files.c0]==focusCurrent);
        tempIndexSubset = find([files(tempIndex).exposureTime]==...
            exposureTimeCheck);
        tempIndexReplace = tempIndex(tempIndexSubset);
        tempIndex = []; tempIndex = tempIndexReplace;
        tempIndexSubset = find([files(tempIndex).solenoidCurrent]==...
            solenoidCurrentCheck);
        tempIndexReplace = tempIndex(tempIndexSubset);
        tempIndex = []; tempIndex = tempIndexReplace;
        tempIndexSubset = find([files(tempIndex).slitX]==...
            slitSel(dataIndex));
        tempIndexReplace = tempIndex(tempIndexSubset);
        tempIndex = []; tempIndex = tempIndexReplace;
        if ~isempty(imageRep)
            if ~isempty(exemptionIndex) && dataIndex == ...
                    exemptionIndex(exemptionCounter)
                tempIndexSubset = find(...
                    [files(tempIndex).MeasurementNumber]==...
                    exemptionSelection(exemptionCounter));
                exemptionCounter = exemptionCounter + 1;
            else
                tempIndexSubset = find(...
                    [files(tempIndex).MeasurementNumber]==imageRep);
            end
            tempIndexReplace = tempIndex(tempIndexSubset);
            tempIndex = []; tempIndex = tempIndexReplace;
        end
        if ~isempty(roiXsel)
            tempIndexSubset = find([files(tempIndex).offsetX]==roiXsel);
            tempIndexReplace = tempIndex(tempIndexSubset);
            tempIndex = []; tempIndex = tempIndexReplace;
        end
        plotIndex = 1;
```

```
        for plotIndex = 1:length(tempIndex)
            transportIndexIndex = transportIndexIndex + 1;
            transportIndex(transportIndexIndex) = tempIndex(plotIndex);
            data(dataIndex,plotIndex) = tempIndex(plotIndex);
            scale(dataIndex,plotIndex) = 1/2 * ...
                (files(tempIndex(plotIndex)).fitCSX.m(1) + ...
                files(tempIndex(plotIndex)).fitCSY.m(1));
        end
    end
    fprintf('.\n');
else
    dataLength = length(focusCurrent);
    for dataIndex = 1:dataLength
        fprintf('.');
        tempIndex = find([files.c0]==focusCurrent(dataIndex));
        tempIndexSubset = find([files(tempIndex).exposureTime]==...
            exposureTimeCheck);
        tempIndexReplace = tempIndex(tempIndexSubset);
        tempIndex = []; tempIndex = tempIndexReplace;
        tempIndexSubset = find([files(tempIndex).solenoidCurrent]==...
            solenoidCurrentCheck);
        tempIndexReplace = tempIndex(tempIndexSubset);
        tempIndex = []; tempIndex = tempIndexReplace;
        tempIndexSubset = find([files(tempIndex).slitX]==slitSel);
        tempIndexReplace = tempIndex(tempIndexSubset);
        tempIndex = []; tempIndex = tempIndexReplace;
        if ~isempty(imageRep)
            if ~isempty(exemptionIndex) && dataIndex == ...
                    exemptionIndex(exemptionCounter)
                tempIndexSubset = find(...
                    [files(tempIndex).MeasurementNumber]==...
                    exemptionSelection(exemptionCounter));
                exemptionCounter = exemptionCounter + 1;
            else
                tempIndexSubset = find(...
                    [files(tempIndex).MeasurementNumber]==imageRep);
            end
            tempIndexReplace = tempIndex(tempIndexSubset);
            tempIndex = []; tempIndex = tempIndexReplace;
        end
        if ~isempty(roiXsel)
            tempIndexSubset = find([files(tempIndex).offsetX]==roiXsel);
            tempIndexReplace = tempIndex(tempIndexSubset);
            tempIndex = []; tempIndex = tempIndexReplace;
        end
```

```
        plotIndex = 1;
        for plotIndex = 1:length(tempIndex)
            transportIndexIndex = transportIndexIndex + 1;
            transportIndex(transportIndexIndex) = tempIndex(plotIndex);
            data(dataIndex,plotIndex) = tempIndex(plotIndex);
            scale(dataIndex,plotIndex) = 1/2 * ...
                (files(tempIndex(plotIndex)).fitCSX.m(1) + ...
                files(tempIndex(plotIndex)).fitCSY.m(1));
        end
    end
    fprintf('.\n');
end


dataEnd = zeros(1,size(data,1));
exposureTime = zeros(1,size(data,1));
for dataIndex = 1:size(data,1)
    fprintf(['Processing data for ' num2str(data(dataIndex,1)) '.']);
    %Select the center of the spot and make an averaged and scaled image.
    for plotIndex = 1:length(data(dataIndex,:))
        fprintf('.');
        if plotIndex == 1 && data(dataIndex,plotIndex)
            imscale(dataIndex,plotIndex) = ...
                (65535/100)/scale(dataIndex,plotIndex);
            if imageCenteredOn
                beamSpotWindow = 3;
                edge1 = round(files(...
                    data(dataIndex,plotIndex)).centroidY-beamSpotWindow);
                edge2 = round(files(...
                    data(dataIndex,plotIndex)).centroidY+beamSpotWindow);
                edge3 = round(files(...
                    data(dataIndex,plotIndex)).centroidX-beamSpotWindow);
                edge4 = round(files(...
                    data(dataIndex,plotIndex)).centroidX+beamSpotWindow);
                plotData(:,:,dataIndex) = imscale(dataIndex,plotIndex)* ...
                    (files(data(dataIndex,plotIndex)).proc(...
                    edge1:edge2,edge3:edge4));
            elseif imageUncenteredOn
                plotData(:,:,dataIndex) = imscale(dataIndex,plotIndex * ...
                    (files(data(dataIndex,plotIndex)).proc);
            end
            exposureTime(dataIndex) = exposureTime(dataIndex) + ...
                files(data(dataIndex,plotIndex)).exposureTime;
        elseif data(dataIndex,plotIndex)
            imscale(dataIndex,plotIndex) = ...
```

```
            (65535/100)/scale(dataIndex,plotIndex);
        if imageCenteredOn
            beamSpotWindow = 3;
            edge1 = round(files(...
                data(dataIndex,plotIndex)).centroidY-beamSpotWindow);
            edge2 = round(files(...
                data(dataIndex,plotIndex)).centroidY+beamSpotWindow);
            edge3 = round(files(...
                data(dataIndex,plotIndex)).centroidX-beamSpotWindow);
            edge4 = round(files(...
                data(dataIndex,plotIndex)).centroidX+beamSpotWindow);
            plotData(:,:,dataIndex) = ...
                plotData(:,:,dataIndex) + ...
                imscale(dataIndex,plotIndex) * ...
                (files(data(dataIndex,plotIndex)).proc(...
                edge1:edge2,edge3:edge4));
        elseif imageUncenteredOn
            plotData(:,:,dataIndex) = plotData(:,:,dataIndex) + ...
                imscale(dataIndex,plotIndex) * ...
                (files(data(dataIndex,plotIndex)).proc);
        end
        exposureTime(dataIndex) = exposureTime(dataIndex) + ...
            files(data(dataIndex,plotIndex)).exposureTime;
    elseif ~dataEnd(dataIndex)
        dataEnd(dataIndex) = plotIndex-1;
        break
    end
end
if ~dataEnd(dataIndex)
    dataEnd(dataIndex) = length(data(dataIndex,:));
end

if automaticCheck
    fprintf('\n');
    %Check for likely MCP damage overlap
    centroidX(dataIndex) = mean([files(...
        data(dataIndex,1:dataEnd(dataIndex))).centroidX]);
    centroidY(dataIndex) = mean([files(...
        data(dataIndex,1:dataEnd(dataIndex))).centroidY]);
    cenotroidMismatchTol = 2.25;
    for plotIndex = 1:dataEnd(dataIndex)
        if files(data(dataIndex,plotIndex)).centroidX > ...
                centroidX(dataIndex)+cenotroidMismatchTol/2 || ...
                files(data(dataIndex,plotIndex)).centroidX < ...
                centroidX(dataIndex)-cenotroidMismatchTol/2
```

```
            deleteIndex = [deleteIndex data(dataIndex,plotIndex)];
            fprintf(['   Found centroid mismatch in data at index ' ...
                num2str(data(dataIndex,plotIndex)) '\n']);
            fprintf(['   X shifted ' ...
                num2str(files(data(dataIndex,plotIndex)).centroidX-...
                centroidX(dataIndex)) ' from mean ' ...
                num2str(centroidX(dataIndex)) '\n']);
         fprintf('   Please re-run with the returned file metadata\n');
        elseif files(data(dataIndex,plotIndex)).centroidY > ...
                centroidY(dataIndex)+cenotroidMismatchTol/2 || ...
                files(data(dataIndex,plotIndex)).centroidY < ...
                centroidY(dataIndex)-cenotroidMismatchTol/2
            deleteIndex = [deleteIndex data(dataIndex,plotIndex)];
            fprintf(['   Found centroid mismatch in data at index ' ...
                num2str(data(dataIndex,plotIndex)) '\n']);
            fprintf(['   Y shifted ' ...
                num2str(files(data(dataIndex,plotIndex)).centroidY- ...
                centroidY(dataIndex)) ' from mean ' ...
                num2str(centroidY(dataIndex)) '\n']);
         fprintf('   Please re-run with the returned file metadata\n');
        end
    end
end

if manualCheck
    centroidX = 115;
    centroidY = 146;
    for plotIndex = 1:dataEnd(dataIndex)
        figure(6);imshow(files(data(dataIndex,plotIndex)).proc*...
            ((65535/10)/scale(dataIndex,plotIndex)*99/...
            dataEnd(dataIndex)),'InitialMagnification', 'fit');
        fprintf(['Automatic centroid flag @ ' num2str(centroidX) ..
            'x, ' num2str(centroidY) 'y\n.']);
        fprintf(['\nX Centroid:' ...
            num2str(files(data(dataIndex,plotIndex)).centroidX) ...
            '\n']);
        fprintf(['Y Centroid:' ...
            num2str(files(data(dataIndex,plotIndex)).centroidY) ...
            '\n']);
        fprintf(['P Rotation:' ...
            num2str(files(data(dataIndex,plotIndex)).orientation) ...
            '\n']);
        fprintf(['X SigmaInt:' ...
            num2str(arrayfun(@(x) x.fitIntX.m(2), ...
            files(data(dataIndex,plotIndex)))) '\n']);
```

```
        fprintf(['Y SigmaInt:' num2str(arrayfun(@(x) ...
            x.fitIntY.m(2), files(data(dataIndex,plotIndex)))) '\n']);
        fprintf(['X SigmaCS: ' num2str(arrayfun(@(x) ...
            x.fitCSX.m(2), files(data(dataIndex,plotIndex)))) '\n']);
        fprintf(['Y SigmaCS: ' num2str(arrayfun(@(x) ...
            x.fitCSY.m(2), files(data(dataIndex,plotIndex)))) '\n']);
        fprintf(['X SigmaX/Y:' num2str(arrayfun(@(x) ...
            x.fitIntX.m(2), files(data(dataIndex,plotIndex))) ...
            ./ arrayfun(@(x) x.fitIntY.m(2), ...
            files(data(dataIndex,plotIndex)))) '\n']);
        deleteCurrent = input('1 to delete, 0 to keep: ');
        fprintf('\n');
        if (~deleteCurrent && ( files(...
                data(dataIndex,plotIndex)).centroidX<centroidX-10|| ...
                files(data(dataIndex,plotIndex)).centroidX > ...
                centroidX + 10 || ...
                files(data(dataIndex,plotIndex)).centroidY < ...
                centroidY - 10 || ...
                files(data(dataIndex,plotIndex)).centroidY > ...
                centroidY  + 10))
            %Track the centroid progress and ask for verification if
            %the mean centroid is far away from the present spot
            %centroid
            deleteCurrent = ...
                input(['Are you sure? Look at the centroid. ' ...
                '1 to delete, 0 to keep:']);
            fprintf('\n')
        end
        if deleteCurrent
            deleteIndex = [deleteIndex data(dataIndex,plotIndex)];
            fprintf(['   Labeled metadata at index ' ...
               num2str(data(dataIndex,plotIndex)) ' for deletion.\n']);
            fprintf(['      Metadata corresponds to I=' ...
                num2str(focusCurrent(dataIndex)) '\n\n']);
        else
            centroidX = mean([centroidX ...
                files(data(dataIndex,plotIndex)).centroidX]);
            centroidY = mean([centroidY ...
                files(data(dataIndex,plotIndex)).centroidY]);
        end
    end
end

%Calculate statistics
dataSet = data(dataIndex,1:dataEnd(dataIndex));
```

```
referenceDataSet = [files(data(dataIndex,...
    1:dataEnd(dataIndex))).posReferenceIndex];
%Quality parameter statistics
focusFitXRmean(dataIndex) = mean([arrayfun(@(x) x.fitIntX.r, ...
    files(dataSet))]);
focusFitYRmean(dataIndex) = std([arrayfun(@(x) x.fitIntY.r, ...
    files(dataSet))]);
focusFitXRstd(dataIndex) = std([arrayfun(@(x) x.fitIntX.r, ...
    files(dataSet))]);
focusFitYRstd(dataIndex) = std([arrayfun(@(x) x.fitIntY.r, ...
    files(dataSet))]);
focusFitXx0mean(dataIndex) = mean([arrayfun(@(x) x.fitIntX.m(3), ...
    files(dataSet))]);
focusFitYx0mean(dataIndex) = mean([arrayfun(@(x) x.fitIntY.m(3), ...
    files(dataSet))]);
focusFitXx0std(dataIndex) = std([arrayfun(@(x) x.fitIntX.m(3), ...
    files(dataSet))]);
focusFitYx0std(dataIndex) = std([arrayfun(@(x) x.fitIntY.m(3), ...
    files(dataSet))]);
focusSNRmean(dataIndex) = mean([files(dataSet).SNR]);
focusSNRstd(dataIndex) = mean([files(dataSet).SNR]);
%Data statistics
focusMajorMean(dataIndex) = mean([files(dataSet).majorAxis]);
focusFxMean(dataIndex) = mean([arrayfun(@(x) x.fitIntX.m(2), ...
    files(dataSet))]);
focusMajorStd(dataIndex) = std([files(dataSet).majorAxis]);
focusFxStd(dataIndex) = std([arrayfun(@(x) x.fitIntX.m(2), ...
    files(dataSet))]);
focusFx2Std(dataIndex) = std([arrayfun(@(x) x.fitIntX.m(2), ...
    files(dataSet))].^2);
focusMinorMean(dataIndex) = mean([files(dataSet).minorAxis]);
focusFyMean(dataIndex) = mean([arrayfun(@(x) x.fitIntY.m(2), ...
    files(dataSet))]);
focusMinorStd(dataIndex) = std([files(dataSet).minorAxis]);
focusFyStd(dataIndex) = std([arrayfun(@(x) x.fitIntY.m(2), ...
    files(dataSet))]);
focusFy2Std(dataIndex) = std([arrayfun(@(x) x.fitIntY.m(2), ...
    files(dataSet))].^2);
focusMajorSubMinorMean(dataIndex) = ...
    mean([files(dataSet).majorAxis] - [files(dataSet).minorAxis]);
focusMajorSubMinorStd(dataIndex) = ...
    std([files(dataSet).majorAxis] - [files(dataSet).minorAxis]);
focusMajorDivMinorMean(dataIndex) = ...
    mean([files(dataSet).majorAxis] ./ [files(dataSet).minorAxis]);
focusMajorDivMinorStd(dataIndex) = ...
```

```
        std([files(dataSet).majorAxis] ./ [files(dataSet).minorAxis]);
    focusOrientationMean(dataIndex) = mean([files(dataSet).orientation]);
    focusOrientationStd(dataIndex) = std([files(dataSet).orientation]);
    focusFxSubFyMean(dataIndex) = ...
        mean([arrayfun(@(x) x.fitIntX.m(2), files(dataSet))] - ...
        [arrayfun(@(x) x.fitIntY.m(2), files(dataSet))]);
    focusFxSubFyStd(dataIndex) = ...
        std([arrayfun(@(x) x.fitIntX.m(2), files(dataSet))] - ...
        [arrayfun(@(x) x.fitIntY.m(2), files(dataSet))]);
    focusFxDivFyMean(dataIndex) = ...
        mean([arrayfun(@(x) x.fitIntX.m(2), files(dataSet))] ./ ...
        [arrayfun(@(x) x.fitIntY.m(2), files(dataSet))]);
    focusFxDivFyStd(dataIndex) = ...
        std([arrayfun(@(x) x.fitIntX.m(2), files(dataSet))] ./ ...
        [arrayfun(@(x) x.fitIntY.m(2), files(dataSet))]);
    focusDeflectXmean(dataIndex) = mean([files(dataSet).centroidX]);
    focusDeflectXstd(dataIndex) = std([files(dataSet).centroidX]);
    focusDeflectYmean(dataIndex) = mean([files(dataSet).centroidY]);
    focusDeflectYstd(dataIndex) = std([files(dataSet).centroidY]);
    fprintf('.\n')
end

%% Deflection statistics plotting
coefficient = gamma*m0*beta*c/magLengthQuad/e0;
'hold'
% X Deflection
%for 11/26/13 and later datasets
figure(8);
errorbar(1e-3*focusCurrent,pixelSize*1e3*...
    (focusDeflectXmean-focusDeflectXmean(1)),...
    -pixelSize*1e3*focusDeflectXstd,1e3*pixelSize*focusDeflectXstd,'.k');
set(gca,'LineWidth',2,'FontSize',30,...
    'FontWeight','normal','FontName','Times');
xlabel('Dipole drive curent (A)','FontSize',40);
ylabel(['Beam deflection, x (mm)'],'FontSize',40);
title('20 \mum iris centered in 600 \mum gap quadrupole electromagnet',...
    'FontSize',40)
undofit;
fit08 = ezfit(1e-3*focusCurrent,pixelSize*1e3* ...
    (focusDeflectXmean-focusDeflectXmean(1)),'poly3');
undofit;
showfit(fit08);
axis([-1.75 1.75 -2 2]);
%for 10/22/13 dataset
figure(80);errorbar(1e-3*focusCurrent,pixelSize*1e3* ...
```

```
    (focusDeflectXmean-focusDeflectXmean(5)),...
    -pixelSize*1e3*focusDeflectXstd,1e3*pixelSize*focusDeflectXstd,'.k');
set(gca,'LineWidth',2,'FontSize',40, ...
    'FontWeight','normal','FontName','Times');
xlabel('Dipole drive curent (A)','FontSize',50);
ylabel(['Beam deflection (mm)'],'FontSize',50);
title('50 \mum iris centered in 600 \mum gap quadrupole electromagnet', ...
    'FontSize',40)
undofit;
fit80 = ezfit(1e-3*focusCurrent(2:end-1),...
  pixelSize*1e3*(focusDeflectXmean(2:end-1)-focusDeflectXmean(5)),'poly3');
undofit;
fout080 = showfit(fit80);
set(fout080.heqbox,'BackgroundColor','none');
set(fout080.heqbox,'FontSize',40);
set(fout080.heqbox,'LineStyle','n');
set(fout080.heqbox,'FontName','Times New Roman')
axis([-4.2 4.2 -3.5 3.5]);
figure(83);
errorbar(1e-3*focusCurrent,coefficient*tan(pixelSize* ...
    (focusDeflectXmean-focusDeflectXmean(5))/(MCP_distance)),...
    -coefficient*tan(pixelSize*focusDeflectXstd/(MCP_distance)), ...
    coefficient*tan(pixelSize*focusDeflectXstd/(MCP_distance)),'.k');
set(gca,'LineWidth',2,'FontSize',40,...
    'FontWeight','normal','FontName','Times');
xlabel('Dipole drive curent (A)','FontSize',50);
ylabel(['Field Strength (T)'],'FontSize',50);
title('50 \mum iris centered in 600 \mum gap quadrupole electromagnet', ...
    'FontSize',40)
undofit;
fit83 = ezfit(1e-3*focusCurrent(2:end-1),...
    coefficient*tan(pixelSize*(focusDeflectXmean(2:end-1)-...
    focusDeflectXmean(5))/MCP_distance),'poly3');
undofit;
fout083 = showfit(fit83);
set(fout083.heqbox,'BackgroundColor','none');
set(fout083.heqbox,'FontSize',40);
set(fout083.heqbox,'LineStyle','n');
set(fout083.heqbox,'FontName','Times New Roman')
axis([-4.2 4.2 -3.5*.022932/2.8092 3.5*.022932/2.8092]);
% Y Deflection
figure(9);
errorbar(1e-3*focusCurrent,1e3*pixelSize* ...
    (focusDeflectYmean-focusDeflectYmean(1)),...
    -1e3*pixelSize*focusDeflectYstd,1e3*pixelSize*focusDeflectYstd,'.k');
```

```
set(gca,'LineWidth',2,'FontSize',30, ...
    'FontWeight','normal','FontName','Times');
xlabel('Dipole drive curent (A)','FontSize',40);
ylabel(['Beam deflection, y (mm)'],'FontSize',40);
title('20 \mum iris centered in 600 \mum gap quadrupole electromagnet', ...
    'FontSize',40)
axis([-1.75 1.75 -2 2]);
undofit;
fit09 = ezfit(1e-3*focusCurrent,pixelSize*1e3* ...
    (focusDeflectYmean-focusDeflectYmean(1)),'poly3');
showfit(fit09);
% Beam shape
figure(6);
errorbar(1e-3*focusCurrent,pixelSize*1e3*focusFxMean, ...
    -pixelSize*1e3*focusFxStd,1e3*pixelSize*focusFxStd,'.k');
set(gca,'LineWidth',2,'FontSize',30, ...
    'FontWeight','normal','FontName','Times');
xlabel('Dipole drive curent (A)','FontSize',40);
ylabel(['Beam RMS envelope, x (mm)'],'FontSize',40);
title('20 \mum iris centered in 600 \mum gap quadrupole electromagnet', ...
    'FontSize',40)
axis([-1.75 1.75 0.05 0.145]);
figure(7);
errorbar(1e-3*focusCurrent,1e3*pixelSize*focusFyMean, ...
    -1e3*pixelSize*focusFyStd,1e3*pixelSize*focusFyStd,'.k');
set(gca,'LineWidth',2,'FontSize',30, ...
    'FontWeight','normal','FontName','Times');
xlabel('Dipole drive curent (A)','FontSize',40);
ylabel(['Beam RMS envelope, y (mm)'],'FontSize',40);
title('20 \mum iris centered in 600 \mum gap quadrupole electromagnet', ...
    'FontSize',40)
axis([-1.75 1.75 0.05 0.145]);
%for 10/22/13 dataset
figure(80);
errorbar(1e-3*focusCurrent,...
    pixelSize*1e3*(focusDeflectYmean-focusDeflectYmean(5)),...
    -pixelSize*1e3*focusDeflectXstd,1e3*pixelSize*focusDeflectXstd,'.k');
set(gca,'LineWidth',2,'FontSize',40, ...
    'FontWeight','normal','FontName','Times');
xlabel('Dipole drive curent (A)','FontSize',50);
ylabel(['Beam deflection (mm)'],'FontSize',50);
title('50 \mum iris centered in 600 \mum gap quadrupole electromagnet', ...
    'FontSize',40)
undofit;
fit80 = ezfit(1e-3*focusCurrent(2:end-1),...
```

```
  pixelSize*1e3*(focusDeflectYmean(2:end-1)-focusDeflectYmean(5)),'poly3');
undofit;
fout080 = showfit(fit80);
set(fout080.heqbox,'BackgroundColor','none');
set(fout080.heqbox,'FontSize',40);
set(fout080.heqbox,'LineStyle','n');
set(fout080.heqbox,'FontName','Times New Roman')
axis([-4.2 4.2 -3.5 3.5]);
figure(83);errorbar(1e-3*focusCurrent,...
    coefficient*tan(pixelSize*...
    (focusDeflectYmean-focusDeflectYmean(5))/(MCP_distance)),...
    -coefficient*tan(pixelSize*focusDeflectXstd/(MCP_distance)), ...
    coefficient*tan(pixelSize*focusDeflectXstd/(MCP_distance)),'.k');
set(gca,'LineWidth',2,'FontSize',40, ...
    'FontWeight','normal','FontName','Times');
xlabel('Dipole drive curent (A)','FontSize',50);
ylabel(['Field Strength (T)'],'FontSize',50);
title('50 \mum iris centered in 600 \mum gap quadrupole electromagnet', ...
    'FontSize',40)
undofit;
fit83 = ezfit(1e-3*focusCurrent(2:end-1), ...
    coefficient*tan(pixelSize*(focusDeflectYmean(2:end-1)- ...
    focusDeflectYmean(5))/MCP_distance),'poly3');
undofit;
fout083 = showfit(fit83);
set(fout083.heqbox,'BackgroundColor','none');
set(fout083.heqbox,'FontSize',40);
set(fout083.heqbox,'LineStyle','n');
set(fout083.heqbox,'FontName','Times New Roman')
axis([-4.2 4.2 -3.5*.041658/2.8092 3.5*.041658/2.8092]);
% Combined X Deflection (Blue is the first dataset, connects at +1.5A)
figure(10);
errorbar(1e-3*focusCurrent,...
    pixelSize*1e3*(focusDeflectXmean-focusDeflectXmean(1)),...
    -pixelSize*1e3*focusDeflectXstd,1e3*pixelSize*focusDeflectXstd,'.b');
set(gca,'LineWidth',2,'FontSize',30, ...
    'FontWeight','normal','FontName','Times');
xlabel('Dipole drive curent (A)','FontSize',40);
ylabel(['Beam Deflection, x (mm)'],'FontSize',40);
title('20 \mum iris centered in 600 \mum gap quadrupole electromagnet', ...
    'FontSize',40)
hold on;
figure(10);
errorbar(1e-3*focusCurrent2, ...
    pixelSize*1e3*(focusDeflectXmean2-focusDeflectXmean2(1)),...
```

```
    -pixelSize*1e3*focusDeflectXstd2,1e3*pixelSize*focusDeflectXstd2,'.r');
set(gca,'LineWidth',2,'FontSize',30, ...
    'FontWeight','normal','FontName','Times');
xlabel('Dipole drive curent (A)','FontSize',40);
ylabel(['Beam Deflection, x (mm)'],'FontSize',40);
title('20 \mum iris centered in 600 \mum gap quadrupole electromagnet', ...
    'FontSize',40)
hold off;
undofit;
fit081 = ezfit(1e-3*focusCurrent, ...
    pixelSize*1e3*(focusDeflectXmean-focusDeflectXmean(1)),'poly3');
showfit(fit081);
fit082 = ezfit(1e-3*[focusCurrent2 focusCurrent(end)], ...
    pixelSize*1e3*([focusDeflectXmean2 focusDeflectXmean(end)]- ...
    focusDeflectXmean2(1)),'poly3');
showfit(fit082);
axis([-1.75 1.75 -2 2]);
% Combined Y Deflection
% (Blue is the first dataset (lower Rep#, connects at -1.5A)
figure(10);
errorbar(1e-3*focusCurrent, ...
    pixelSize*1e3*(focusDeflectYmean-focusDeflectYmean(1)),...
    -pixelSize*1e3*focusDeflectYstd,1e3*pixelSize*focusDeflectYstd,'.r');
set(gca,'LineWidth',2,'FontSize',30, ...
    'FontWeight','normal','FontName','Times');
xlabel('Dipole drive curent (A)','FontSize',40);
ylabel(['Beam deflection, y (mm)'],'FontSize',40);
title('20 \mum iris centered in 600 \mum gap quadrupole electromagnet', ...
    'FontSize',40)
axis([-1.75 1.75 -2 2]);
hold on;
figure(10);
errorbar(1e-3*focusCurrent2, ...
    pixelSize*1e3*(focusDeflectYmean2-focusDeflectYmean2(1)),...
    -pixelSize*1e3*focusDeflectYstd2,1e3*pixelSize*focusDeflectYstd2,'.b');
set(gca,'LineWidth',2,'FontSize',30, ...
    'FontWeight','normal','FontName','Times');
xlabel('Dipole drive curent (A)','FontSize',40);
ylabel(['Beam deflection, y (mm)'],'FontSize',40);
title('20 \mum iris centered in 600 \mum gap quadrupole electromagnet', ...
    'FontSize',40)
axis([-1.75 1.75 -2 2]);
hold off;
undofit;
fit081 = ezfit(1e-3*focusCurrent, ...
```

```
    pixelSize*1e3*(focusDeflectYmean-focusDeflectYmean(1)),'poly3');
showfit(fit081);
fit082 = ezfit(1e-3*focusCurrent2, ...
    pixelSize*1e3*(focusDeflectYmean2-focusDeflectYmean2(1)),'poly3');
showfit(fit082);
axis([-1.75 1.75 -2 2]);

figure(1);plot(1,1); %images of average beam at each current point
subplotSize = ceil(sqrt(length(focusCurrent)));
for dataIndex = 1+2:2:length(focusCurrent)-2
    subplot(1,length(1+2:2:length(focusCurrent)-2),(dataIndex-1)/2);
    dataScaleAbs = 65535/max(max(max(plotData(:,:,:))));
    dataScaleTime = 100/exposureTime(dataIndex);
    dataScaleEnd = 1/dataEnd(dataIndex);
    dataScale = 99/dataEnd(dataIndex);
    imshow(plotData(:,:,dataIndex)*dataScale);
    set(gca,'LineWidth',2,'FontSize',30,...
        'FontWeight','normal','FontName','Times');
    title(['I = ' num2str(focusCurrent(dataIndex)) ' mA'],...
        'FontSize',30,'FontWeight','normal','FontName','Times');
end
figure(2);plot(1,1); %images of average beam at each current point
subplotSize = ceil(sqrt(length(focusCurrent)));
for dataIndex = 1:length(focusCurrent)
    subplot(subplotSize,subplotSize,dataIndex);
    dataScaleAbs = 65535/max(max(max(plotData(:,:,:))));
    dataScaleTime = 100/exposureTime(dataIndex);
    dataScaleEnd = 1/dataEnd(dataIndex);
    dataScale = 99/dataEnd(dataIndex);
    imshow(plotData(:,:,dataIndex)*dataScale);
    set(gca,'LineWidth',2,'FontSize',30,...
        'FontWeight','normal','FontName','Times');
    title(['I = ' num2str(focusCurrent(dataIndex)) ' mA'],...
        'FontSize',30,'FontWeight','normal','FontName','Times');
end
%% Data cleaning
if ~isempty(unique(deleteIndex))
    fprintf(['Found centroid mismatch in data. Deleted ' ...
        num2str(length(unique(deleteIndex))) ' metadata entries.' ]);
    fprintf('Please rerun with new metadata.\n');
    files(unique([deleteIndex])) = [];
end
'hold';
```

A.3 Beam-focusing data processing MATLAB script

```
function [files] = plotQuadData(files)
% [plotData,focusMajorMean,focusMajorStd,...
%     focusMinorMean,focusMinorStd,FocusMajorSubMinorMean,...
%     focusMajorSubMinorStd]

manualCheck = 0;
automaticCheck = 0;

%Dataset 10/22/2013 doesn't have focusing data for c0=2000mA.
focusCurrent = [-1500:100:1400];
imageRep = 2;
%focusCurrent = 0;
exposureTimeCheck = .25; % s
solenoidCurrentCheck = 1870; %mA

%Pick out the index of the focusing data
transportIndex = [];
transportIndexIndex = 0;
fprintf('Finding quadruple data');
for dataIndex = 1:length(focusCurrent)
    fprintf('.');
    tempIndex = find([files.c0]==focusCurrent(dataIndex));
    tempIndexSubset =find([files(tempIndex).c1]==-focusCurrent(dataIndex));
    tempIndexReplace = tempIndex(tempIndexSubset);
    tempIndex = []; tempIndex = tempIndexReplace;
    tempIndexSubset = find([files(tempIndex).c2]==focusCurrent(dataIndex));
    tempIndexReplace = tempIndex(tempIndexSubset);
    tempIndex = []; tempIndex = tempIndexReplace;
    tempIndexSubset =find([files(tempIndex).c3]==-focusCurrent(dataIndex));
    tempIndexReplace = tempIndex(tempIndexSubset);
    tempIndex = []; tempIndex = tempIndexReplace;
    %Select the datasets for long enough exposure times.
    %if abs(focusCurrent(dataIndex)) <= 5000
    tempIndexSubset = find([files(tempIndex).exposureTime]==...
        exposureTimeCheck);
    tempIndexReplace = tempIndex(tempIndexSubset);
    tempIndex = []; tempIndex = tempIndexReplace;
    tempIndexSubset = find([files(tempIndex).solenoidCurrent]==...
        solenoidCurrentCheck);
    tempIndexReplace = tempIndex(tempIndexSubset);
    tempIndex = []; tempIndex = tempIndexReplace;
    %end
    if ~isempty(imageRep)
```

```
        tempIndexSubset = find([files(tempIndex).MeasurementNumber]==...
            imageRep);
        tempIndexReplace = tempIndex(tempIndexSubset);
        tempIndex = []; tempIndex = tempIndexReplace;
    end

    plotIndex = 1;
    for plotIndex = 1:length(tempIndex)
        transportIndexIndex = transportIndexIndex + 1;
        transportIndex(transportIndexIndex) = tempIndex(plotIndex);
        data(dataIndex,plotIndex) = tempIndex(plotIndex);
        scale(dataIndex,plotIndex) = 1/2 * ...
            (files(tempIndex(plotIndex)).fitCSX.m(1) + ...
            files(tempIndex(plotIndex)).fitCSY.m(1));
    end
end
fprintf('.\n');

deleteIndex = [];

dataEnd = zeros(1,length(focusCurrent));
exposureTime = zeros(1,length(focusCurrent));
for dataIndex = 1:length(focusCurrent)
    fprintf(['Processing data for ' num2str(focusCurrent(dataIndex)) ...
        ' mA quadrupole current ']);
    %Select the center of the spot and make an averaged and scaled image.
    for plotIndex = 1:length(data(dataIndex,:))
        fprintf('.');
        if plotIndex == 1 && data(dataIndex,plotIndex)
            edge1 = round(files(data(dataIndex,plotIndex)).centroidY-20);
            edge2 = round(files(data(dataIndex,plotIndex)).centroidY+20);
            edge3 = round(files(data(dataIndex,plotIndex)).centroidX-20);
            edge4 = round(files(data(dataIndex,plotIndex)).centroidX+20);
            imscale(dataIndex,plotIndex) = ...
                (2^16/100)/scale(dataIndex,plotIndex);
            plotData(:,:,dataIndex) = imscale(dataIndex,plotIndex) * ...
                (files(data(dataIndex,plotIndex)).proc(...
                edge1:edge2,edge3:edge4));
            exposureTime(dataIndex) = exposureTime(dataIndex) + ...
                files(data(dataIndex,plotIndex)).exposureTime;
        elseif data(dataIndex,plotIndex)
            edge1 = round(files(data(dataIndex,plotIndex)).centroidY-20);
            edge2 = round(files(data(dataIndex,plotIndex)).centroidY+20);
            edge3 = round(files(data(dataIndex,plotIndex)).centroidX-20);
            edge4 = round(files(data(dataIndex,plotIndex)).centroidX+20);
```

```
        imscale(dataIndex,plotIndex) = ...
            (2^16/100)/scale(dataIndex,plotIndex);
        plotData(:,:,dataIndex) = plotData(:,:,dataIndex) + ...
            imscale(dataIndex,plotIndex) * ...
            (files(data(dataIndex,plotIndex)).proc(...
            edge1:edge2,edge3:edge4));
        exposureTime(dataIndex) = exposureTime(dataIndex) + ...
            files(data(dataIndex,plotIndex)).exposureTime;
    elseif ~dataEnd(dataIndex)
        dataEnd(dataIndex) = plotIndex-1;
        break
    end
end
if ~dataEnd(dataIndex)
    dataEnd(dataIndex) = length(data(dataIndex,:));
end

if automaticCheck
    fprintf('\n');
    %Check for MCP damage overlap w/ the beam spot
    centroidX(dataIndex) = ...
        mean([files(data(dataIndex,1:dataEnd(dataIndex))).centroidX]);
    centroidY(dataIndex) = ...
        mean([files(data(dataIndex,1:dataEnd(dataIndex))).centroidY]);
    cenotroidMismatchTol = 2.25;
    for plotIndex = 1:dataEnd(dataIndex)
        if files(data(dataIndex,plotIndex)).centroidX > ...
                centroidX(dataIndex)+cenotroidMismatchTol/2 || ...
                files(data(dataIndex,plotIndex)).centroidX < ...
                centroidX(dataIndex)-cenotroidMismatchTol/2
            deleteIndex = [deleteIndex data(dataIndex,plotIndex)];
            fprintf(['   Found centroid mismatch in data at index ' ...
                num2str(data(dataIndex,plotIndex)) '\n']);
            fprintf(['   X shifted ' ...
                num2str(files(data(dataIndex,plotIndex)).centroidX- ...
                centroidX(dataIndex)) ' from mean ' ...
                num2str(centroidX(dataIndex)) '\n']);
         fprintf('   Please re-run with the returned file metadata\n');
        elseif files(data(dataIndex,plotIndex)).centroidY > ...
                centroidY(dataIndex)+cenotroidMismatchTol/2 || ...
                files(data(dataIndex,plotIndex)).centroidY < ...
                centroidY(dataIndex)-cenotroidMismatchTol/2
            deleteIndex = [deleteIndex data(dataIndex,plotIndex)];
            fprintf(['   Found centroid mismatch in data at index ' ...
                num2str(data(dataIndex,plotIndex)) '\n']);
```

```
            fprintf(['   Y shifted ' ...
                num2str(files(data(dataIndex,plotIndex)).centroidY- ...
                centroidY(dataIndex)) ' from mean ' ...
                num2str(centroidY(dataIndex)) '\n']);
         fprintf('   Please re-run with the returned file metadata\n');
        end
    end
end

if manualCheck
    centroidX = 115;
    centroidY = 146;
    for plotIndex = 1:dataEnd(dataIndex)
        figure(6);imshow(files(data(dataIndex,plotIndex)).proc* ...
            ((2^16/10)/scale(dataIndex,plotIndex)* ...
            99/dataEnd(dataIndex)),'InitialMagnification', 'fit');
        fprintf(['Automatic centroid flag @ ' num2str(centroidX) ...
            'x, ' num2str(centroidY) 'y\n.']);
        fprintf(['\nX Centroid:' ...
            num2str(files(data(dataIndex,plotIndex)).centroidX) '\n']);
        fprintf(['Y Centroid:' ...
            num2str(files(data(dataIndex,plotIndex)).centroidY) '\n']);
        fprintf(['P Rotation:' ...
          num2str(files(data(dataIndex,plotIndex)).orientation) '\n']);
        fprintf(['X SigmaInt:' num2str(arrayfun(@(x) ...
            x.fitIntX.m(2), files(data(dataIndex,plotIndex)))) '\n']);
        fprintf(['Y SigmaInt:' num2str(arrayfun(@(x) ...
            x.fitIntY.m(2), files(data(dataIndex,plotIndex)))) '\n']);
        fprintf(['X SigmaCS: ' num2str(arrayfun(@(x) ...
            x.fitCSX.m(2), files(data(dataIndex,plotIndex)))) '\n']);
        fprintf(['Y SigmaCS: ' num2str(arrayfun(@(x) ...
            x.fitCSY.m(2), files(data(dataIndex,plotIndex)))) '\n']);
        fprintf(['X SigmaX/Y:' num2str(arrayfun(@(x) ...
            x.fitIntX.m(2), files(data(dataIndex,plotIndex))) ./ ...
            arrayfun(@(x) x.fitIntY.m(2), ...
            files(data(dataIndex,plotIndex)))) '\n']);
        deleteCurrent = input('1 to delete, 0 to keep: ');
        fprintf('\n');
        if (~deleteCurrent && ...
                ( files(data(dataIndex,plotIndex)).centroidX < ...
                centroidX - 10 || ...
                files(data(dataIndex,plotIndex)).centroidX > ...
                centroidX + 10 || ...
                files(data(dataIndex,plotIndex)).centroidY < ...
                centroidY - 10 || ...
```

```
                files(data(dataIndex,plotIndex)).centroidY > ...
                centroidY  + 10))
            %Track the centroid progress and ask for verification if
            %the mean centroid is far away from the present spot
            %centroid
            deleteCurrent = input(['Are you sure? ' ...
                'Look at the centroid. 1 to delete, 0 to keep:']);
            fprintf('\n')
        end
        if deleteCurrent
            deleteIndex = [deleteIndex data(dataIndex,plotIndex)];
            fprintf(['   Labeled metadata at index ' ...
                num2str(data(dataIndex,plotIndex)) ...
                ' for deletion.\n']);
            fprintf(['      Metadata corresponds to I=' ...
                num2str(focusCurrent(dataIndex)) '\n\n']);
        else
            centroidX = mean([centroidX ...
                files(data(dataIndex,plotIndex)).centroidX]);
            centroidY = mean([centroidY ...
                files(data(dataIndex,plotIndex)).centroidY]);
        end
    end
end

%Calculate statistics
dataSet = data(dataIndex,1:dataEnd(dataIndex));
referenceDataSet = ...
    [files(data(dataIndex,1:dataEnd(dataIndex))).posReferenceIndex];
%Quality parameter statistics
focusFitXRmean(dataIndex) = ...
    mean([arrayfun(@(x) x.fitIntX.r, files(dataSet))]);
focusFitYRmean(dataIndex) = ...
    std([arrayfun(@(x) x.fitIntY.r, files(dataSet))]);
focusFitXRstd(dataIndex) = ...
    std([arrayfun(@(x) x.fitIntX.r, files(dataSet))]);
focusFitYRstd(dataIndex) = ...
    std([arrayfun(@(x) x.fitIntY.r, files(dataSet))]);
focusFitXx0mean(dataIndex) = ...
    mean([arrayfun(@(x) x.fitIntX.m(3), files(dataSet))]);
focusFitYx0mean(dataIndex) = ...
    mean([arrayfun(@(x) x.fitIntY.m(3), files(dataSet))]);
focusFitXx0std(dataIndex) = ...
    std([arrayfun(@(x) x.fitIntX.m(3), files(dataSet))]);
focusFitYx0std(dataIndex) = ...
```

```
    std([arrayfun(@(x) x.fitIntY.m(3), files(dataSet))]);
focusSNRmean(dataIndex) = mean([files(dataSet).SNR]);
focusSNRstd(dataIndex) = mean([files(dataSet).SNR]);
%Data statistics
focusMajorMean(dataIndex) = mean([files(dataSet).majorAxis]);
focusFxMean(dataIndex) = ...
    mean([arrayfun(@(x) x.fitIntX.m(2), files(dataSet))]);
focusMajorStd(dataIndex) = std([files(dataSet).majorAxis]);
focusFxStd(dataIndex) = ...
    std([arrayfun(@(x) x.fitIntX.m(2), files(dataSet))]);
focusFx2Std(dataIndex) = ...
    std([arrayfun(@(x) x.fitIntX.m(2), files(dataSet))].^2);
focusMinorMean(dataIndex) = mean([files(dataSet).minorAxis]);
focusFyMean(dataIndex) = ...
    mean([arrayfun(@(x) x.fitIntY.m(2), files(dataSet))]);
focusMinorStd(dataIndex) = std([files(dataSet).minorAxis]);
focusFyStd(dataIndex) = ...
    std([arrayfun(@(x) x.fitIntY.m(2), files(dataSet))]);
focusFy2Std(dataIndex) = ...
    std([arrayfun(@(x) x.fitIntY.m(2), files(dataSet))].^2);
focusMajorSubMinorMean(dataIndex) = ...
    mean([files(dataSet).majorAxis] - [files(dataSet).minorAxis]);
focusMajorSubMinorStd(dataIndex) = ...
    std([files(dataSet).majorAxis] - [files(dataSet).minorAxis]);
focusMajorDivMinorMean(dataIndex) = ...
    mean([files(dataSet).majorAxis] ./ [files(dataSet).minorAxis]);
focusMajorDivMinorStd(dataIndex) = ...
    std([files(dataSet).majorAxis] ./ [files(dataSet).minorAxis]);
focusOrientationMean(dataIndex) = mean([files(dataSet).orientation]);
focusOrientationStd(dataIndex) = std([files(dataSet).orientation]);
focusFxSubFyMean(dataIndex) = ...
    mean([arrayfun(@(x) x.fitIntX.m(2), files(dataSet))] - ...
    [arrayfun(@(x) x.fitIntY.m(2), files(dataSet))]);
focusFxSubFyStd(dataIndex) = ...
    std([arrayfun(@(x) x.fitIntX.m(2), files(dataSet))] - ...
    [arrayfun(@(x) x.fitIntY.m(2), files(dataSet))]);
focusFxDivFyMean(dataIndex) = ...
    mean([arrayfun(@(x) x.fitIntX.m(2), files(dataSet))] ./ ...
    [arrayfun(@(x) x.fitIntY.m(2), files(dataSet))]);
focusFxDivFyStd(dataIndex) = ...
    std([arrayfun(@(x) x.fitIntX.m(2), files(dataSet))] ./ ...
    [arrayfun(@(x) x.fitIntY.m(2), files(dataSet))]);
focusDeflectXmean(dataIndex) = mean([files(dataSet).centroidX]);
focusDeflectXstd(dataIndex) = std([files(dataSet).centroidX]);
focusDeflectYmean(dataIndex) = mean([files(dataSet).centroidY]);
```

```
    focusDeflectYstd(dataIndex) = std([files(dataSet).centroidY]);
    fprintf('.\n')
end

%% Least squares fit beam parameters
%Electron properties
e0  = -1.60217646e-19;  %C
m0  = 9.10938188e-31;   %kg
Ebeam = 34e3;
restmass    = 510998.93;%eV
%Fundamental constants
c       = 299792458;        %m/s
h       = 6.626068e-34;     %m^2*kg/s
eps0    = 8.85418782e-12;   %F/m;
mu0     = 1.25663706e-6;    %H/m
gamma   = Ebeam./restmass+1;%absolute
beta    = sqrt(1-1./gamma.^2);%absolute
%Quadrupole constants -- I added a mT/m to keep f from hitting inf @ I = 0
Bgrad   = focusCurrent*39.8e-3;%39.8 Tesla/m @ 1000 mA
quadL   = 371e-6;
MCP_distance        = 11.5e-2;%From Evan
magLengthQuad       = 370.7e-6;%From simulation
magLengthDipole     = 686e-6;
Kappa = (e0*Bgrad)/(gamma*m0*beta*c);
f=1./(Kappa*quadL);
%Drift constants
% Distance between the MCP and the quadrupole. 10/22/13
driftL  = 12.1e-2;
%MCP Pixel Size (10/22/13)
pixelSize = 57.15e-3/(1725-358); % From MCP_pixelsize.png
transportIndex = 0;
dataCurrent = [];
for dataIndex = 1:length(focusCurrent)
    for plotIndex = 1:dataEnd(dataIndex)
        %Don't put anything higher than this in this loop
        transportIndex = transportIndex + 1;
        dataCurrent(transportIndex) = focusCurrent(dataIndex);
        sigmaX(transportIndex) = ...
            (pixelSize*arrayfun(@(x) x.fitIntX.m(2), ...
            files(data(dataIndex,plotIndex))));
        sigmaY(transportIndex) = ...
            (pixelSize*arrayfun(@(x) x.fitIntY.m(2), ...
            files(data(dataIndex,plotIndex))));
        T1(transportIndex,:)=[1 -2*driftL*(focusCurrent(dataIndex)*1e-3)...
            driftL^2*(focusCurrent(dataIndex)*1e-3)^2 driftL^2 ...
```

```
            2*driftL -2*driftL^2*(focusCurrent(dataIndex)*1e-3)];
        T2(transportIndex,:)=[1 -2*driftL*(focusCurrent(dataIndex)*1e-3)...
            driftL^2*(focusCurrent(dataIndex)*1e-3)^2 driftL^2 ...
            2*driftL -2*driftL^2*(focusCurrent(dataIndex)*1e-3)];
    end
end
transportParamX = sigmaX.^2'\T1;
transportParamY = sigmaY.^2'\T2;

%% Plot data
fprintf('Plotting data\n')

figure(1);plot(1,1); %images of average beam at each current point
subplotSize = ceil(sqrt(length(focusCurrent)));
for dataIndex = 1+2:2:length(focusCurrent)-2
    subplot(1,length(1+2:2:length(focusCurrent)-2),(dataIndex-1)/2);
    dataScaleAbs = 65535/max(max(max(plotData(:,:,:))));
    dataScaleTime = 100/exposureTime(dataIndex);
    dataScaleEnd = 1/dataEnd(dataIndex);
    dataScale = 99/dataEnd(dataIndex);
    imshow(plotData(:,:,dataIndex)*dataScale);
    set(gca,'LineWidth',2,'FontSize',12,...
        'FontWeight','normal','FontName','Times');
    title(['I = ' num2str(focusCurrent(dataIndex)) ' mA'],...
        'FontSize',14,'FontWeight','normal','FontName','Times');
end

figure(2);plot(1,1); %images of average beam at each current point
subplotSize = ceil(sqrt(length(focusCurrent)));
for dataIndex = 1:length(focusCurrent)
    subplot(subplotSize,subplotSize,dataIndex);
    dataScaleAbs = 65535/max(max(max(plotData(:,:,:))));
    dataScaleTime = 100/exposureTime(dataIndex);
    dataScaleEnd = 1/dataEnd(dataIndex);
    dataScale = 99/dataEnd(dataIndex);
    imshow(plotData(:,:,dataIndex)*dataScale);
    set(gca,'LineWidth',2,'FontSize',30,...
        'FontWeight','normal','FontName','Times');
    title(['I = ' num2str(focusCurrent(dataIndex)) ' mA'],...
        'FontSize',30,'FontWeight','normal','FontName','Times');
end

% Ratio of beam shape
figure(3);
errorbar(focusCurrent,focusFxDivFyMean,...
```

```
    -focusFxDivFyStd,focusFxDivFyStd,'.');
set(gca,'LineWidth',2,'FontSize',22,...
    'FontWeight','normal','FontName','Times');
xlabel('Quadruople drive curent (mA)','FontSize',30);
ylabel(['Electron beam shape' 10 ...
    '(x-axis width / y-axis width)'],'FontSize',30);
axis([-5500 5500 0.5 1.5]);

%plot average beam width at each current point
figure(6);
errorbar(1e-3*focusCurrent,pixelSize*1e3*focusFxMean,...
    -pixelSize*1e3*focusFxStd,1e3*pixelSize*focusFxStd,'.k');
set(gca,'LineWidth',2,'FontSize',30,...
    'FontWeight','normal','FontName','Times');
xlabel('Quadruople drive curent (A)','FontSize',40);
ylabel(['Beam RMS envelope, x (mm)'],'FontSize',40);
title('20 \mum iris centered in 600 \mum gap quadrupole electromagnet',...
    'FontSize',40)
axis([-1.75 1.75 0.095 0.145]);
undofit;
fit6 = ezfit(1e-3*focusCurrent(1:15),pixelSize*1e3*focusFxMean(1:15),...
    'poly2');
showfit(fit6);
figure(7);errorbar(1e-3*focusCurrent,1e3*pixelSize*focusFyMean,...
    -1e3*pixelSize*focusFyStd,1e3*pixelSize*focusFyStd,'.k');
set(gca,'LineWidth',2,'FontSize',30,...
    'FontWeight','normal','FontName','Times');
xlabel('Quadruople drive curent (A)','FontSize',40);
ylabel(['Beam RMS envelope, y (mm)'],'FontSize',40);
title('20 \mum iris centered in 600 \mum gap quadrupole electromagnet',...
    'FontSize',40)
axis([-1.75 1.75 0.095 0.145]);
undofit;
fit7 = ezfit(1e-3*focusCurrent(end-15:end),...
    1e3*pixelSize*focusFyMean(end-15:end),'poly2');
showfit(fit7);
%plotting each fit
figure(4);plot(1,1);
set(gca,'FontSize',12,'FontWeight','normal','FontName','Times')
subplotSize = ceil(sqrt(length(focusCurrent)));
for dataIndex = 1:length(focusCurrent)
    subplot(subplotSize,subplotSize,dataIndex);
    hold on;
    for plotIndex = 1:dataEnd(dataIndex)
        fitIntX = files(data(dataIndex,plotIndex)).fitIntX;
```

```
        fitIntX.x = 40e-3*fitIntX.x;
        fitIntX.m(3) = 40e-3*fitIntX.m(3);
        fitIntX.m(2) = 40e-3*fitIntX.m(2);
        showfit(fitIntX,'fitcolor','blue','fitlinewidth',1);
        title(['     I = ' num2str(focusCurrent(dataIndex)) ' mA'],...
            'FontSize',14,'FontWeight','normal','FontName','Times');
        %       xlabel('Y-position (mm)');
        %       ylabel('Image intensity (counts)');
        axis([40e-3*[0 41] 0 max([arrayfun(@(x) x.fitIntY.m(1), ...
            files(data(dataIndex,1:dataEnd(dataIndex))))])])
    end
end
hold off;
%plotting each fit
figure(5);plot(1,1);
set(gca,'FontSize',12,'FontWeight','normal','FontName','Times')
subplotSize = ceil(sqrt(length(focusCurrent)));
for dataIndex = 1:length(focusCurrent)
    subplot(subplotSize,subplotSize,dataIndex);
    hold on;
    for plotIndex = 1:dataEnd(dataIndex)
        fitIntY = files(data(dataIndex,plotIndex)).fitIntY;
        fitIntY.x = 40e-3*fitIntY.x;
        fitIntY.m(3) = 40e-3*fitIntY.m(3);
        fitIntY.m(2) = 40e-3*fitIntY.m(2);
        showfit(fitIntY,'fitcolor','red','fitlinewidth',1);
        title(['     I = ' num2str(focusCurrent(dataIndex)) ' mA'],...
            'FontSize',14,'FontWeight','normal','FontName','Times');
        %       xlabel('Y-position (mm)');
        %       ylabel('Image intensity (counts)');
        axis([40e-3*[0 41] 0 max([arrayfun(@(x) x.fitIntY.m(1), ...
            files(data(dataIndex,1:dataEnd(dataIndex))))])])
    end
end
hold off;

if ~isempty(unique(deleteIndex))
    fprintf(['Found centroid mismatch in data. Deleted ' ...
        num2str(length(unique(deleteIndex))) ' metadata entries.' ]);
    fprintf('Please rerun with new metadata.\n');
    files(unique([deleteIndex])) = [];
end
'hold';
```

APPENDIX B

Free electron laser simulation scripts

The simulation scripts used to calculate the radiation from the MEMS undulators are provided below. The simulation software can be downloaded from the UCLA PBPL website.

B.1 GENESIS FEL simulation script of a $\lambda_r = 1$ nm FEL using a $\lambda_u = 400$ μm undulator

```
$newrun
aw0    =  0.02641E-00
xkx    =  5.00000E-01
xky    =  5.00000E-01
wcoefz =  0.00000E+00 0.00000E+00 0.00000E+00
xlamd  =  4.00000E-04
fbess0 =  0.00000E+00
delaw  =  9.30000E-07
iertyp =  2
iwityp =  0
awd    =  0.02641E-00
iseed  =  -1
npart  =  1024
gamma0 =  4.10960E+02
delgam =  4.11000E-03
rxbeam =  1.2000E-05
rybeam =  1.2000E-05
alphax =  0.00000E-00
alphay =  0.00000E-00
emitx  =  0.05000E-06
emity  =  0.05000E-06
xbeam  =  0.00000E+00
ybeam  =  0.00000E+00
pxbeam =  0.00000E+00
pybeam =  0.00000E+00
```

```
isravg =  0
isrsig =  0
cuttail=  -1.00000E+00
xlamds =  1.1850723E-09
prad0  =  1.00000E+00
zrayl  =  1.20000E+00
zwaist =  0.10000E-00
ncar   =  121
lbc    =  0
rmax0  =  0.00000E+00
dgrid  =  4.00000E-04
nscr   =  1
nscz   =  1
nptr   =  40
nwig   =  19800
zsep   =  4.00000E+00
delz   =  2.00000E+00
nsec   =  1
iorb   =  1
zstop  =  -1.00000E+00
magin  =  1
magout =  1
ildgam =  5
ildpsi =  7
ildx   =  1
ildy   =  2
ildpx  =  3
ildpy  =  4
itgaus =  0
nbins  =  8
lout   =  1 1 1 1 1 0 1 1 1 1 1 1 1 1 0 0 0 0 0 0 0 0 0 0
iphsty =  1
ishsty =  1
ippart =  100
ispart =  100
ipradi =  0
isradi =  0
idump  =  0
iotail =  1
idmpfld=  0
idmppar=  0
nharm  =  1
ntail  =  0
nslice =  408
shotnoise =  0.00000E+00
```

```
 ipseed =  -1
 iall   =  0
 itdp   =  0
 iscan  =  23
 nscan  =  3
 svar   =  5.00000E-05
 ilog   =  0
 filetype  =  'ORIGINAL'
 beamfile  =  '1nm_400um.beam'
 maginfile =  '1nm_400um.lat'
 magoutfile=  '1nm_400um.line'
 outputfile=  '1nm_400um.dat'
 $end
```

B.2 GENWAKE wakefield energy modulation script for a 750 A, 100 pC, gaussian beam in a 400 μm wide aluminum waveguide

```
radius = 100e-6
roundpipe = 0
h_rough = 0e-9
l_rough = 50e-9
sigma = 5.96e7
tau = 8.09e-06
current = 750
profile = gauss
bunchlength = 1.6e-5
outputfile = 1nm_400um100um100pCCu.beam
comploss = 100
```

APPENDIX C

Fabrication Traveler

	Microundulator fabrication process	v.3.0	3/11/2013		STL
Step	Process name	Tool	Recipe	Time	Description
0.00	Measure wafers	Tool	Recipe	0:30:00	MEASURE WAFERS
0.01	Measure resistivity	resmap		0:10:00	Measure wafer resistivity
0.02	Measure thickness	caliper		0:10:00	Measure wafer thickness
0.03	Measure wafer bow	flexus		0:10:00	Characterize wafer bow
1.00	MET1 process	Tool	Recipe	16:25:40	WINDING BOTTOM METAL PROCESS
1.01	MET1 fill - Lithography dehydration bake	hotplate	150 C	0:10:00	
1.02	MET1 fill - Lithography adhesion	HMDS		0:10:00	
1.03	MET1 fill - Lithography spin	spinner	5um KMPR1005	0:01:00	500RPM 10sec, 4000RPM 30sec, 500RPM 10sec- (5um)
1.04	MET1 fill - Lithography soft bake	hotplate	100 C	0:02:30	
1.05	MET1 fill - Lithography exposure	344.020 - KS_MA6	180 mJ MU3MET1v1	0:00:21	
1.06	MET1 fill - Lithography post exposure bake	hotplate	100 C	0:02:00	
1.07	MET1 fill - Lithography develop		MF26-A	0:02:00	
1.08	MET1 fill - Descum	Tegal or Matrix	500 mTorr 200 W or 3.45Torr 100C 80W	0:02:00	
1.09	MET1 fill - Measure DRIE etch rate	UNAXIS_DRIE	b59_jh	0:02:00	Measure modified bosch 59 etch rate (typically between 1869 and 2374 nm/min) on unoxidized Si (might need an HF dip)
1.10	MET1 fill - Etch MET1 trench in Si	UNAXIS_DRIE	b59_jh	0:05:21	Etch 15 um trench for MET1 fill into clean unoxidized Si (might need an HF dip)
1.11	MET1 fill - Strip PR	NMP (ALEG355)	80 C	0:30:00	Strip photoresist with wafer upside down in cassette
1.12	MET1 fill - Descum	Tegal or Matrix	500 mTorr 200 W or 3.45Torr 100C 80W	0:02:00	
1.13	MET1 fill - Oxide deposition	131.011 - Furnace	500 nm	4:00:00	Deposit 500 nm SiO2 insulation
1.14	MET1 fill - Seed layer deposition	CVC	Seed TiCuTi	6:00:00	2 min 800 W suptter etch, deposit 30 nm Ti (8 min w/ 65W bias), 300 nm Cu (55min w/out bias + 55min w/ 65W bias + 55min w/out bias), and 30 nm Ti (8 min w/ 65 W bias). If wafer bias power supply reflected power rises, then breaker 2 on the RF matching network has tripped and needs to be reset (push button inside the back of the rack)
1.15	MET1 fill - Ti etch	1% HF beaker		0:00:10	Etch until Cu visible. Quench with DI
1.16	MET1 fill - Copper fill electroplating	Cu plating tank	318 mA	3:46:18	Deposit 25 microns Cu, w/ agitaion, 3in anode aperture
1.17	MET1 fill - Measure wafer bow	Flexus or Dektek		0:10:00	Characterize wafer bow for compensation
1.18	MET1 fill - Stress compensation	Carbolite Oven	95C with high N2 flow	0:30:00	Wafer bow should be <5 micron
1.19	MET1 fill - Copper planarization	Logitech_CDP	CU_cmp	0:40:00	95%ALUMTX100 / 5%EVERFLO, 15mL/min, 5psi, 40RPM. Check at 30min. Don't overpolish
1.20	MET1 fill - Measure resistance test structure	probestation		0:10:00	
2.00	VIA process	Tool	Recipe	14:25:37	INDUCTOR VIA FILL PROCESS
2.01	VIA - Seed layer deposition	CVC	Seed TiCuTi	6:00:00	2 min 700 W suptter etch, deposit 60 nm Ti (8 min w/ 65W bias), 300 nm Cu (120 min w/ no bias), and 60 nm Ti (8 min w/ 65W bias).
2.02	VIA - Measure seed thickness	Dektek		0:10:00	measure thickness from dummy wafer
2.03	VIA - If new bottle, degas KMPR1025 in bottle	hotplate	HP to 55 C	0:30:00	Degas photoresist (reduces SB bubbles). Then cool back to room temp
2.04	VIA - Lithography dehydration bake	hotplate	150 C	0:10:00	

	Microundulator fabrication process	v.3.0	3/11/2013		STL
Step	Process name	Tool	Recipe	Time	Description
2.05	VIA - Lithography adhesion	HMDS		0:10:00	
2.06	VIA - Vacuum desiccation	YES oven	30 C 40 Torr	0:01:00	**Pull bubbles out from features. Tape foil down in oven. Use a VERY big PR puddle**
2.07	VIA - Lithography spin	spinner	**75 um KMPR1025**	0:05:00	**500RPM 20sec, 1100RPM 30 sec (75um)**
2.08	VIA - Lithography rest	spinner	rest 5 min	0:05:00	rest on spinner 5 minutes to level
2.09	VIA - Lithography clean	acetone + wipe	clean 1mm from edge	0:01:00	Clean edge bead, then 500rpm for 10s
2.10	VIA - Lithography soft bake	hotplate	65 C on Al plate	0:05:00	degas resist
2.11	VIA - Lithography soft bake	hotplate	100 C on Al plate	0:25:00	set HP to ~105 (CNSI)
2.12	VIA - Lithography rest		> 1 hour rest	2:00:00	Reduce stress
2.13	VIA - Lithography exposure	344.020 - KS_MA6	**749 mJ MU3VIAv1 w/Filter**	0:01:06	Wafer might stick to mask. Use a blade.
2.14	VIA - Lithography post exposure bake	hotplate	100 C on Al plate	0:06:00	set HP to ~105 (CNSI)
2.15	VIA - Lithography rest		15 min rest	0:15:00	Reduce stress (nitrogen)
2.16	VIA - Lithography develop		SU-8 developer	0:08:00	vigorous agitation- use the stirring hotplate with the X stirbar rotating at 900 RPM and the wafer upside down in a cassette. When finished, rinse with SU8 developer, then IPA, then water.
2.17	VIA - Descum	Matrix	3.75 Torr, 80 W, 100C	0:03:00	descum
2.18	VIA - Check edge passivation				If oxide is gone from wafer edge due to CMP, rub some AZ5214 from a cleanwipe onto the wafer edge and bake it in the Carbolite oven at 100 C for 10 minutes.
2.19	VIA - Ti etch	1%-5% HF beaker		0:00:10	Etch until Cu visible. Wait another minute- copper should become visible in all the vias. Quench with DI
2.20	VIA - CU Via electroplating	Cu plating tank	18mA	4:55:21	Deposit 65um
2.21	VIA - Polish flat	Logitech CDP	1 PSI, 100nm Alumina	0:20:00	Polish rate is about 1um/min. Stop when metal looks flat.
2.22	VIA - Strip PR & Seed	STS_AOE	KMPRISO1	0:50:00	**Dry etch of PR and seed. Finish with KMPRISO2 if there is seed remaining in areas with a high density of vias.**
2.23	VIA - Measure VIA height	Dektek		0:05:00	Measure thickness of structure across wafer
2.24	VIA - Clean PECVD chamber	STSMESC	etchdep	2:30:00	Run a standard etch + deposition on the chamber
2.25	VIA - Measure PECVD nitride dep rate	STSMESC	ltlfsinstj	0:10:00	Mesure low frequency nitride dep rate on a dummy (~44. 4nm/min)
2.26	VIA - Measure PECVD oxide dep rate	STSMESC	ltlfsiostj	0:10:00	Mesure low frequency oxide dep rate on a dummy (~36.7 nm/min, has issues starting deposition)
2.27	VIA - Nitride deposition	STSMESC	ltlfsinstj	0:15:00	deposit 540 nm Nitride
2.28	VIA - Oxide deposition	STSMESC	ltlfsiostj	0:10:00	deposit 500 nm Oxide
2.29	VIA - Nitride deposition	STSMESC	ltlfsinstj	0:15:00	deposit 450 nm Nitride
2.30	VIA - Measure thicknese	Filmtek & SEM		0:30:00	Measure thickness and inspect coverage at edge of MET1. Repeat PECVD if inadequate coverage.
3.00	**MAG process**	**Tool**	**Recipe**	**30:12:53**	**INDUCTOR YOKE & POLE PROCESS**
3.01	MAG - Seed layer deposition	CVC	Seed TiCuTi	6:00:00	4 min 700 W suptter etch, deposit 60 nm Ti (8 min w/ 65W bias), 300 nm Cu (120 min w/ no bias), and 60 nm Ti (8 min w/ 65W bias).
3.02	MAG - Lithography dehydration bake	hotplate	150 C	0:10:00	
3.03	MAG - Lithography adhesion	HMDS		0:10:00	

	Microundulator fabrication process	v.3.0	3/11/2013		STL
Step	Process name	Tool	Recipe	Time	Description
3.04	MAG - Vacuum desiccation	YES oven	30 C 40 Torr	0:01:00	**Pull bubbles out from features. Tape foil down in oven. Use a VERY big PR puddle**
3.05	MAG - Lithography spin	spinner	**70 um KMPR1025**	0:05:00	**500RPM 20sec, 1100RPM 30 sec (120um)**
3.06	MAG - Lithography rest	spinner	rest 5 min	0:05:00	rest on spinner 5 minutes to level
3.07	MAG - Lithography clean	acetone + wipe	clean 1mm from edge	0:01:00	Clean edge bead, then 500rpm for 10s
3.08	MAG - Lithography soft bake	hotplate	65 C on Al plate	0:05:00	degas resist
3.09	MAG - Lithography soft bake	hotplate	100 C on Al plate	0:30:00	set HP to ~105 (CNSI)
3.10	MAG - Lithography rest		> 1 hour rest	2:00:00	Reduce stress
3.11	MAG - Lithography exposure	344.020 - KS_MA6	**1000 mJ MU3MAGv2 w/Filter**	0:01:23	Wafer might stick to mask. Use a blade. Extra dose to make up for shadowing
3.12	MAG - Lithography post exposure bake	hotplate	100 C on Al plate	0:04:00	set HP to ~100 (CNSI)
3.13	MAG - Lithography rest		15 min rest	0:15:00	Reduce stress (nitrogen)
3.14	MAG - Lithography develop		SU-8 developer	0:12:00	vigorous agitation- use the stirring hotplate with the X stirbar rotating at 700 RPM and the wafer upside down in a cassette. When finished, rinse with SU8 developer, then IPA, then water.
3.15	MAG - Descum	Matrix	3.75 Torr, 80 W, 100C	0:03:00	descum
3.16	MAG - Check edge passivation				If oxide is gone from wafer edge due to CMP, rub some AZ5214 from a cleanwipe onto the wafer edge and bake it in the Carbolite oven at 100 C for 10 minutes.
3.17	MAG - Ti etch	1%-5% HF beaker		0:00:10	Etch until Cu visible in the VSM circles. Wait another minute- copper should become visible in all the small 'fill' holes. Quench with DI
3.18	MAG - Magnetic alloy electroplating	Alloy plating tank	10 mA	15:00:00	Deposit 50um at 5mA/cm^2, 30RPM agitation, 3.0 pH
3.19	MAG - Measure alloy concentration	EDX in the SEM		0:45:00	Measure atomic concentration
3.20	MAG - Polish flat	Logitech CDP	1 PSI, 100nm Alumina	0:20:00	Polish rate is about 1um/min. Stop when metal looks flat.
3.21	MAG - Strip PR	STS_AOE	KMPRISO1	0:50:00	**Dry etch of PR and seed. Finish with KMPRISO2 if Cu is not exposed**
3.22	MAG - Strip seed Cu	5% acetic 15% H2O2		0:00:10	Etch until Ti visible. Overetch 15 sec. Quench with DI
3.23	MAG - Strip seed Ti	1% HF beaker		0:00:10	Etch until no visible metal. Overetch 15 sec.Quench with DI
3.24	MAG - Measure magnet thickness	Dektek		0:30:00	Measure thickness of structure across wafer
3.25	MAG - Clean PECVD chamber	STSMESC	etchdep	2:30:00	
3.26	MAG - Measure PECVD nitride dep rate	STSMESC	ltlfsinstj	0:05:00	Mesure standard low temperature nitride dep rate (typically around 30 nm/min)
3.27	MAG - Nitride deposition	STSMESC	ltlfsinstj	0:30:00	deposit 900 nm low temperature nitride
4.00	**SU-8 process**	**Tool**	**Recipe**	**15:16:19**	**WINDING INTERCONNECT PROCESS**
4.01	SU8 - Degas photoresist	hotplate	55 C	0:30:00	Degas photoresist (eliminates SB bubbles)
4.02	SU8 - Lithography dehydration bake	hotplate	150 C	0:10:00	No HMDS for permanent SU-8 on oxide
4.03	SU8 - Vacuum desiccation	YES oven	35 C 40 Torr	0:01:00	**Pull bubbles out from features. Tape foil down in oven.**
4.04	SU8 - Lithography spin	spinner	**85 um SU-8 2025**	0:02:00	**500RPM 20sec, 1450RPM 30sec, then EBR**
4.05	SU8 - Lithography soft bake	hotplate	65 C	0:03:00	If you have to rework before post exposure bake, Dissolve in SU8 developer
4.06	SU8 - Lithography soft bake	hotplate	95 C	0:06:00	If you have to rework after PEB, ramp ALEG temperature. It still probably will not survive.

	Microundulator fabrication process	v.3.0	3/11/2013		STL
Step	Process name	Tool	Recipe	Time	Description
4.07	SU8 - Lithography rest		1 hour rest	2:00:00	Reduce stress
4.08	SU8 - Lithography exposure	344.020 - KS_MA6	**300 mJ MU3SU8v1 w/ Filter**	0:00:19	use UV filter - extra dose to make up for shadow
4.09	SU8 - Lithography post exposure bake	hotplate	65 C	0:03:00	
4.10	SU8 - Lithography post exposure bake	hotplate	95 C	0:06:00	
4.11	SU8 - Lithography rest		1 hour rest	2:00:00	Reduce stress (nitrogen)
4.12	SU8 - Polish flat	Logitech CDP	1 PSI, 50nm Silica	0:08:00	Polish rate is about 1 um/min. Stop before hitting the metal
4.13	SU8 - Lithography develop		SU-8 developer	0:04:00	vigorous agitation- use the stirring hotplate with the X stirbar rotating at 900 RPM and the wafer upside down in a cassette. When finished, rinse with SU8 developer, then IPA, then water.
4.14	SU8 - Descum	Matrix	3.75Torr, 80W, 100C	0:03:00	Repeat until VIA is clear
4.15	SU8 - Vacuum bake	YES oven	180 C	10:00:00	Permenant hard bake (2 hour ramp up, 4 hour bake, and 4 hour ramp down)
5.00	**MET2 process**	**Tool**	**Recipe**	**12:19:49**	**WINDING TOP METAL PROCESS**
5.01	MET2 - Oxide etch	STS_AOE	ljydboxj	0:02:00	Inspect for cleared oxide
5.02	MET2 - Measure capacitance test structures	probestation		0:10:00	
5.03	MET2 - Seed layer deposition	CVC	Seed TiCuTi	6:00:00	2 min 800 W suptter etch, deposit 30 nm Ti (8 min w/ 65 W bias), 300 nm Cu (55 min with no bias, 55min w/ 65 W bias, 55min without bias), and 30 nm Ti (8 min w/ 65 W bias).
5.04	MET2 - Lithography dehydration bake	hotplate	150 C on Al plate	0:15:00	**Use Al plate!**
5.05	MET2 - Lithography adhesion	HMDS		0:10:00	
5.06	MET2 - Vacuum dessicate	YES oven	35 C 40 Torr	0:01:00	**Pour very large puddle-- bigger than all features. Pull bubbles out from features. Tape foil down in oven.**
5.07	MET2 - Lithography spin	spinner	20 um KMPR1025	0:01:00	500 RPM 10 sec 100 RPM/s, 1500 RPM 10 sec 300 RPM/s, 4000 RPM 30 sec 300 RPM/s
5.08	MET2 - Lithography soft bake	hotplate	100 C covered	0:10:00	cover with beaker to bake
5.09	MET2 - Lithography exposure	344.020 - KS_MA6	500 mJ mu3MET2v1	0:00:41	w/ UV filter
5.10	MET2 - Lithography post exposure bake	hotplate	100 C covered on Al plate	0:05:00	cover with beaker to bake
5.11	MET2 - Lithography develop		SU-8 developer	0:04:00	vigorous agitation- use the stirring hotplate with the X stirbar rotating at 900 RPM and the wafer upside down in a cassette. When finished, rinse with SU8 developer, then IPA, then water.
5.12	MET2 - Descum	Matrix	3.75 Torr, 80 W, 50C	0:03:00	cannot be any rest steps in this lithography
5.13	MET2 - Ti etch	1% HF beaker		0:00:10	Etch until Cu visible. Quench with DI
5.14	MET2 - Cu electroplating	Cu plating tank	18 mA	1:29:24	Deposit 10um at 5mA/cm^2, agitation, 0.5in anode aperture
5.15	MET2 - Gold electroplating	Gold CN plating tank	18 mA	0:03:04	Deposit 1um at 5mA/cm^2, 300RPM agitation, 55C temp
5.16	MET2 - Strip PR	NMP (ALEG355)	80 C	2:00:00	Strip photoresist upside down in half cassette
5.17	MET2 - Strip PR	STS_AOE	KMPRISO1	0:10:00	**Dry etch of PR and seed. Finish with KMPRISO2 if Cu is not exposed**
5.18	MET2 - Inspect strip			0:05:00	All PR must be gone before seed strip. Pay attentiaon to the edge at the gap. Repeat strip process if necessary.
5.19	MET2 - Strip seed Ti	1% HF beaker		0:00:10	Etch until Cu visible. Overetch 15 sec. Quench with DI
5.20	MET2 - Strip seed Cu	5% acetic 15% H2O2		0:00:10	Etch until Ti visible. Overetch 15 sec. Quench with DI

	Microundulator fabrication process	v.3.0	3/11/2013		STL
Step	**Process name**	**Tool**	**Recipe**	**Time**	**Description**
5.21	MET2 - Strip seed Ti	1% HF beaker		0:00:10	Etch until no visible metal. Overetch 15 sec. Quench with DI
5.22	MET2 - Measure resistance test structures	probestation		0:10:00	
5.23	MET2 - Measure capacitance test structures	probestation		0:10:00	
5.24	MET2 - Measure impedance test structures	probestation		0:10:00	
5.25	MET2 - Etch SU8 off	STS AOE	KMPRISO1	1:00:00	Thick film negative photoresist etch. ~50 microns / hour
6.00	**Die Preperation**	**Tool**	**Recipe**	**5:16:14**	**DRIE THROUGH WAFER FOR BEAM HOLES AND DICING**
6.01	DRIE - Lithography dehydration bake	hotplate	150 C on Al plate	0:15:00	
6.02	DRIE - Lithography adhesion	HMDS		0:10:00	
6.03	DRIE - Lithography spin	spinner	10 um KMPR1005	0:01:00	500 RPM 10 sec, 1000 RPM 30 sec, 500 RPM 10sec
6.04	DRIE - Lithography soft bake	hotplate	100 C covered	0:03:00	
6.05	DRIE - Lithography exposure	344.020 - KS_MA6	180mJ mu3DRIv1	0:00:14	Backside alignment
6.06	DRIE - Lithography post exposure bake	hotplate	100 C covered	0:02:00	
6.07	DRIE - Lithography develop		SU-8 developer	0:02:00	
6.08	DRIE - Descum	Matrix	3.75 Torr, 80 W, 100C	0:01:00	
6.09	DRIE - Etch backside oxide	STS AOE	ljydbox	0:02:00	Check to make sure it is down to bare silicon
6.10	DRIE - Backside tech	FDRIE	UCLA FAST NANO 5x10min	2:00:00	examine at 50 minutes and calculate the remaining etch time
6.11	DRIE - Clean	wet bench	acetone/methanol/IPA	0:10:00	
6.12	DRIE - Sort singulated dies			0:30:00	
6.13	DRIE - Measure VSM circle	VSM		2:00:00	Measure MH curve of magnetic alloy
Total numbe of steps:				**Total Process Time**	
133				94:26:32	

References

[AAB09] A Anghel, F Atchison, B Blau, B Van den Brandt, M Daum, R Doelling, M Dubs, P-A Duperrex, A Fuchs, D George, et al. "The PSI ultra-cold neutron source." *Nuclear Instruments and Methods in Physics Research Section A: Accelerators, Spectrometers, Detectors and Associated Equipment*, **611**(2):272–275, 2009.

[AAG11] F Albert, SG Anderson, DJ Gibson, RA Marsh, SS Wu, CW Siders, CPJ Barty, and FV Hartemann. "Design of narrow-band Compton scattering sources for nuclear resonance fluorescence." *Physical Review Special Topics - Accelerators and Beams*, **14**(5):050703, 2011.

[ABS13] K Achterhold, M Bech, S Schleede, G Potdevin, R Ruth, R Loewen, and F Pfeiffer. "Monochromatic computed tomography with a compact laser-driven X-ray source." *Nature Scientific Reports*, **3**, 2013.

[ADD05] D Anicic, M Daum, G Dzieglewski, D George, M Horvat, G Janser, F Jenni, I Jirousek, K Kirch, T Korhonen, et al. "A fast kicker magnet for the PSI 600 MeV proton beam to the PSI ultra-cold neutron source." *Nuclear Instruments and Methods in Physics Research Section A: Accelerators, Spectrometers, Detectors and Associated Equipment*, **541**(3):598–609, 2005.

[AW09] DP Arnold and N Wang. "Permanent magnets for MEMS." *Journal of Microelectromechanical Systems*, **18**(6):1255 –1266, dec. 2009.

[Ban07] KLF Bane. "Wakefields of sub-picosecond electron bunches." In *Proceedings of the 46th Workshop of the INFN ELOISATRON Project: Erice, Italy, 9-14 October 2005*, volume 28, p. 46. World Scientific Pub. Co. Inc., Singapore, 2007.

[BCD07] MJ Barnes, F Caspers, L Ducimetière, N Garrel, and T Kroyer. "An improved beam screen for the LHC injection kickers." In *Proceedings of the 2007 Particle Accelerator Conference*, pp. 1574–1576. IEEE, 2007.

[BEH86] EW Becker, W Ehrfeld, P Hagmann, A Maner, and D Münchmeyer. "Fabrication of microstructures with high aspect ratios and great structural heights by synchrotron radiation lithography, galvanoforming, and plastic moulding (LIGA process)." *Microelectronic engineering*, **4**(1):35–56, 1986.

[BGL99] MBH Breese, GW Grime, W Linford, and M Harold. "An extended magnetic quadrupole lens for a high-resolution nuclear microprobe." *Nuclear Instruments and Methods in Physics Research Section B: Beam Interactions with Materials and Atoms*, **158**(1):48–52, 1999.

[BKJ01] MBH Breese, DG de Kerckhove, C Jeynes, RMA Peel, and CW Murray. "An electrostatic beam rocking system on the Surrey nuclear microprobe." *Nuclear Instruments and Methods in Physics Research Section B: Beam Interactions with Materials and Atoms*, **181**(1):54–59, 2001.

[BNC97] KLF Bane, CK Ng, and AW Chao. "Estimate of the impedance due to wall surface roughness." In *Proceedings of the 1997 Particle Accelerator Conference, Vancouver, Canada*, volume 2, pp. 1738–1740. IEEE, New York, 1997.

[BNN11] CC Boehme, MP Nicol, P Nabeta, JS Michael, E Gotuzzo, et al. "Feasibility, diagnostic accuracy, and effectiveness of decentralised use of the Xpert MTB/RIF test for diagnosis of tuberculosis and multidrug resistance: a multicentre implementation study." *The lancet*, **377**(9776):1495–1505, 2011.

[BPN84] R Bonifacio, C Pellegrini, and LM Narducci. "Collective instabilities and high-gain regime in a free electron laser." *Optics Communications*, **50**(6):373–378, 1984.

[BS96] KLF Bane and M Sands. "The short-range resistive wall wakefields." In *AIP Conference Proceedings*, volume 367, p. 131, 1996.

[BS03] KLF Bane and G Stupakov. "Impedance of a rectangular beam tube with small corrugations." *Physical Review Special Topics - Accelerators and Beams*, **6**(2), 2003.

[BS05] KLF Bane and G Stupakov. "Resistive wall wakefield in the LCLS undulator." Technical report, United States Department of Energy, Washington, DC, 2005.

[BVS01] AA Bettiol, JA Van Kan, TC Sum, and F Watt. "A LabVIEW-based scanning and control system for proton beam micromachining." *Nuclear Instruments and Methods in Physics Research Section B: Beam Interactions with Materials and Atoms*, **181**(1):49–53, 2001.

[CAP10] M-C Chen, P Arpin, T Popmintchev, M Gerrity, B Zhang, M Seaberg, D Popmintchev, MM Murnane, and HC Kapteyn. "Bright, coherent, ultrafast soft x-ray harmonics spanning the water window from a tabletop light source." *Physical Review Letters*, **105**(17):173901, 2010.

[CCD10] BP Chaudhri, F Ceyssens, P De Moor, C Van Hoof, and R Puers. "A high aspect ratio SU-8 fabrication technique for hollow microneedles for transdermal drug delivery and blood extraction." *Journal of Micromechanics and Microengineering*, **20**:064006, 2010.

[CDF09] S Caspi, DR Dietderich, H Felice, P Ferracin, R Hafalia, CR Hannaford, AF Lietzke, J Lizarazo, G Sabbi, XR Wang, et al. "Test results of LARP quadrupole magnets using a shell-based support structure (TQS)." *IEEE Transactions on Applied Superconductivity*, **19**(3):1221–1225, 2009.

[Cen14] Stanford Linear Accelerator Center. "LCLS parameters.", January 2014.

[Cha93] A Chao. *Physics of collective beam instabilities in high energy accelerators*. Wiley, 1993.

[CIE11] S Cipiccia, MR Islam, B Ersfeld, RP Shanks, E Brunetti, G Vieux, X Yang, RC Issac, SM Wiggins, GH Welsh, et al. "Gamma-rays from harmonically resonant betatron oscillations in a plasma wake." *Nature Physics*, **7**(11):867–871, 2011.

[CKS13] S Chatrchyan, V Khachatryan, AM Sirunyan, A Tumasyan, W Adam, et al. "Study of the mass and spin-parity of the Higgs boson candidate via its decays to Z boson pairs." *Physical Review Letters*, **110**(8):081803, 2013.

[Cla04] JA Clarke. *The science and technology of undulators and wigglers*, volume 4. Oxford University Press, USA, 2004.

[CPG13] S Chen, ND Powers, I Ghebregziabher, CM Maharjan, C Liu, G Golovin, S Banerjee, J Zhang, N Cunningham, A Moorti, et al. "MeV-energy X-rays from inverse Compton scattering with laser-wakefield accelerated electrons." *Physical Review Letters*, **110**(15):155003, 2013.

[Dan14a] Danfysik. "ALBA Storage Ring Dipoles.", 2014.

[Dan14b] Danfysik. "Green Magnets.", April 2014.

[Dan14c] Danfysik. "Rutherford-ISIS Slow Kicker Systems.", April 2014.

[DBD09] Y Ding, A Brachmann, FJ Decker, D Dowell, P Emma, J Frisch, S Gilevich, G Hays, P Hering, Z Huang, et al. "Measurements and simulations of ultralow emittance and ultrashort electron beams in the linac coherent light source." *Physical Review Letters*, **102**(25):254801, 2009.

[DCS95] BM Dunham, LS Cardman, and CK Sinclair. "Emittance measurements for the Illinois/CEBAF polarized electron source." In *Proceedings of the 1995 Particle Accelerator Conference*, volume 2, pp. 1030–1032. IEEE, 1995.

[DKG03] L Daudin, H Khodja, and JP Gallien. "Development of position–charge–time tagged spectrometry for ion beam microanalysis." *Nuclear Instruments and Methods in Physics Research Section B: Beam Interactions with Materials and Atoms*, **210**:153–158, 2003.

[Dow10] D Dowell. "Classes of electron guns and injectors [Lecture notes].", June 2010.

[DSB07] BM Dunham, CK Sinclair, IV Bazarov, Y Li, X Liu, and KW Smolenski. "Performance of a very high voltage photoemission electron gun for a high brightness, high average current ERL injector." In *Proceedings of the 2007 Particle Accelerator Conference*, pp. 1224–1226. IEEE, 2007.

[EGB07] T Eichner, F Grüner, S Becker, M Fuchs, D Habs, R Weingartner, U Schramm, H Backe, P Kunz, and W Lauth. "Miniature magnetic devices for laser-based, table-top free-electron lasers." *Physical Review Special Topics - Accelerators and Beams*, **10**:082401, Aug 2007.

[Ele14a] Deutsches Elektronen-Synchrotron. "The European X-ray laser project XFEL.", April 2014.

[Ele14b] Deutsches Elektronen-Synchrotron. "Free-electron laser FLASH.", April 2014.

[ELM03] E Efstathiadis, YY Lee, JL Mi, C Pai, JM Paley, BL Roberts, RT Sanders, YK Semertzidis, and DS Warburton. "A fast non-ferric kicker for the muon (<i >g </ i >- 2) experiment." *Nuclear Instruments and Methods in Physics Research Section A: Accelerators, Spectrometers, Detectors and Associated Equipment*, **496**(1):8–25, 2003.

[FHW04] LE Felton, N Hablutzel, WA Webster, and KP Harney. "Chip scale packaging of a MEMS accelerometer." In *Proceedings of the 54th Electronic Components and Technology Conference, 2004.*, volume 1, pp. 869–873. IEEE, 2004.

[FMS12] K Fan, H Matsumoto, T Sugimoto, S Fukuoka, H Someya, T Toyama, K Ishii, et al. "Design and test of injection kickers for JPARC main ring." In *Proceedings of 2012 International Particle Accelerator Conference, New Orleans, USA*, 2012.

[FWP09] M Fuchs, R Weingartner, A Popp, Z Major, S Becker, J Osterhoff, I Cortrie, B Zeitler, R Hörlein, GD Tsakiris, U Schramm, TP Rowlands-Rees, SM Hooker, D Habs, F Krausz, S Karsch, and F Grüner. "Laser-driven soft-X-ray undulator source." *Nature Physics*, **5**:826–829, November 2009.

[FWT99] W Flack, S White, and B Todd. "Process characterization of one hundred micron thick photoresist films." In *Proceedings of Advances in Resist Technology and Processing XVI*, pp. 474–490. SPIE, Bellingham, WA, 1999.

[GAA10] DJ Gibson, F Albert, SG Anderson, SM Betts, MJ Messerly, et al. "Design and operation of a tunable MeV-level Compton-scattering-based γ-ray source." *Physical Review Special Topics-Accelerators and Beams*, **13**(7):070703, 2010.

[GDM85] VL Granatstein, WW Destler, and ID Mayergoyz. "Small-period electromagnet wigglers for free-electron lasers." *Applied Physics Letters*, **47**(6):643–645, 1985.

[GHN10] M Glickman, J Harrison, T Niblock, P Tseng, and JW Judy. "High Permeability Permalloy for MEMS." In *Hilton Head 2010, A Solid-State Sensors, Actuators and Microsystems Workshop*, pp. 328–331. Transducer Research Foundation, Inc., San Diego, CA, 2010.

[GKP10] J Grutters, A Kessels, M Pijls-Johannesma, D De Ruysscher, MA Joore, and P Lambin. "Comparison of the effectiveness of radiotherapy with photons, protons and carbon-ions for non-small cell lung cancer: a meta-analysis." *Radiotherapy and Oncology*, **95**(1):32–40, 2010.

[GNP08] CGR Geddes, K Nakamura, GR Plateau, C Toth, E Cormier-Michel, E Esarey, CB Schroeder, JR Cary, and WP Leemans. "Plasma-density-gradient injection of low absolute-momentum-spread electron bunches." *Physical Review Letters*, **100**(21):215004, 2008.

[Gol76] E Goldstein. "Vorläufige Mittheilungen über electrishe Entladungen in Verdünnten Gasen." *Berlin Akd. Monatsber*, **279**, 1876.

[GPR97] BI Grishanov, FV Podgorny, J Ruemmler, and VD Shiltsev. "Very fast kicker with high repetition rate for accelerator applications." *Nuclear Instruments and Methods in Physics Research Section A: Accelerators, Spectrometers, Detectors and Associated Equipment*, **396**(1):28–34, 1997.

[GTH09] M Glickman, P Tseng, J Harrison, IB Goldberg, P Johnson, P Smeys, T Niblock, and JW Judy. "CMOS-compatible back-end process for in-plane actuating ferromagnetic MEMS." In *Proceedings of the 15th International Conference on Solid-State Sensors, Actuators Microsystems (Transducers 2009), Denver, CO*, pp. 248 –251. IEEE, IEEE, June 2009.

[GTH11] M Glickman, P Tseng, J Harrison, T Niblock, IB Goldberg, and JW Judy. "High-Performance Lateral-Actuating Magnetic MEMS Switch." *Journal of Microelectromechanical Systems*, **20**(4):842 –851, aug. 2011.

[GTV04] CGR Geddes, C. Toth, J. Van Tilborg, E. Esarey, CB Schroeder, D. Bruhwiler, C. Nieter, J. Cary, and WP Leemans. "High-quality electron beams from a laser wakefield accelerator using plasma-channel guiding." *Nature*, **431**(7008):538–541, 2004.

[HJH14] J Harrison, A Joshi, Y Hwang, O Paydar, L Lake, P Musumeci, and RN Candler. "Surface-micromachined electromagnets for 100 μm-scale undulators and focusing optics." In *Physics and Applications of High Brightness Beams Workshop, HBEB 2013*. Elsevier, 2014.

[HJL12] J Harrison, A Joshi, J Lake, RN Candler, and P Musumeci. "Surface-micromachined magnetic undulator with period length between 10 μm and 1 mm for advanced light sources." *Physical Review Special Topics - Accelerators and Beams*, **16**:070703, 2012.

[HK07] Z Huang and KJ Kim. "Review of x-ray free-electron laser theory." *Physical Review Special Topics - Accelerators and Beams*, **10**(3), 2007.

[HKM98] T Hezel, B Krevet, HO Moser, JA Rossmanith, R Rossmanith, and Th Schneider. "A superconductive undulator with period length of 3.8 mm." *Journal of Synchrotron Radiation*, **5**:448–450, 1998.

[Hor97] LJ Hornbeck et al. "Digital light processing^{TM} for high-brightness, high-resolution applications." In *Proceedings of the SPIE*, volume 3013, pp. 27–40, 1997.

[HPH14] J Harrison, O Paydar, Y Hwang, J Wu, E Threlkeld, P Musumeci, and RN Candler. "Fabrication process for thick-film micromachined multi-pole electromagnets." *JMEMS Letters*, **23**(3), 2014.

[Ins14] Japan Synchrotron Radiation Research Institute. "Spring-8 Web Site.", April 2014.

[JSG07] I Jovanovic, M Shverdin, D Gibson, and C Brown. "High-power laser pulse recirculation for inverse Compton scattering-produced γ-rays." *Nuclear Instruments and Methods in Physics Research Section A: Accelerators, Spectrometers, Detectors and Associated Equipment*, **578**(1):160–171, 2007.

[KAC09] VVS Kashikhin, N Andreev, G Chlachidze, J DiMarco, VV Kashikhin, MJ Lamm, ML Lopes, M Tartaglia, JC Tompkins, G Velev, et al. "Test results of a superconducting quadrupole model designed for linear accelerator applications." *IEEE Transactions on Applied Superconductivity*, **19**(3):1176–1181, 2009.

[KAK12] VS Kashikhin, N Andreev, J Kerby, Y Orlov, N Solyak, M Tartaglia, and G Velev. "Superconducting splittable quadrupole magnet for linear accelerators." *IEEE Transactions on Applied Superconductivity*, **22**(3):4002904–4002904, 2012.

[KBC12] SK Kim, DR Burris, H Chang, J Bryant-Genevier, and ET Zellers. "Microfabricated gas chromatograph for on-site determination of trichloroethylene in indoor air arising from vapor intrusion. 1. Field evaluation." *Environmental science & technology*, **46**(11):6065–6072, 2012.

[KBH98] R Klein, J Bahrdt, D Herzog, and G Ulm. "The PTB electromagnetic undulator for BESSY II." *Journal of Synchrotron Radiation*, **5**(3):451–452, 1998.

[KM14] K Koseki and H Matsumoto. "The fast extraction kicker for J-PARC with a novel pulse compression system." *Nuclear Instruments and Methods in Physics Research Section A: Accelerators, Spectrometers, Detectors and Associated Equipment*, **739**:63–67, 2014.

[KMM10] S Kneip, C McGuffey, JL Martins, SF Martins, C Bellei, V Chvykov, F Dollar, R Fonseca, C Huntington, G Kalintchenko, A Maksimchuk, SPD. Mangles, T Matsuoka, SR Nagel, CAJ Palmer, J Schreiber, KT Phuoc, AGR Thomas, V Yanovsky, LO Silva, K Krushelnick, and Z Najmudin. "Bright spatially coherent synchrotron X-rays from a table-top source." *Nature Physics*, **6**:980–983, 2010.

[KR32] M Knoll and E Ruska. "Das elektronenmikroskop." *Zeitschrift für Physik*, **78**(5-6):318–339, 1932.

[KSS04] S Knappe, V Shah, P Schwindt, L Hollberg, J Kitching, L Liew, and J Moreland. "A microfabricated atomic clock." *Applied Physics Letters*, **85**(9):1460–1462, 2004.

[KTK06] J Kamiya, T Takayanagi, T Kawakubo, S Murasugi, and E Nakamura. "Kicker Magnet System of the RCS in J-PARC." *IEEE Transactions on Applied Superconductivity*, **16**(2):168–171, 2006.

[Lab14] Lawrene Berkeley National Laboratory. "ALS Beamlines Directory.", April 2014.

[LCC99] S Lebed, M Cholewa, Z Cioch, B Cleff, P Golonka, DN Jamieson, GJF Legge, S Łazarski, A Potempa, C Sarnecki, et al. "Design and first results of the nuclear microprobe in Cracow." *Nuclear Instruments and Methods in Physics Research Section B: Beam Interactions with Materials and Atoms*, **158**(1):44–47, 1999.

[Leb99] S Lebed. "Optimization of the ion-optical components for the new Cracow scanning nuclear microprobe." *Nuclear Instruments and Methods in Physics Research Section B: Beam Interactions with Materials and Atoms*, **155**(3):322–325, 1999.

[Lee04] SY Lee. *Accelerator physics*. World Scientific, 2004.

[Lee12] SC Leemann. "Injection with a single dipole kicker into the MAX IV storage rings." *Nuclear Instruments and Methods in Physics Research Section A: Accelerators, Spectrometers, Detectors and Associated Equipment*, **693**:117–129, 2012.

[LFT05] J Lim, P Frigola, G Travish, and JB Rosenzweig. "Adjustable, short focal length permanent-magnet quadrupole based electron beam final focus system." *Physical Review Special Topics - Accelerators and Beams*, **8**(7), 2005.

[LHR98] W Lou, D Hartill, D Rice, D Rubin, and J Welch. "Stability considerations of permanent magnet quadrupoles for CESR phase-III upgrade." *Physical Review Special Topics - Accelerators and Beams*, **1**(2):022401, 1998.

[LJ08] CH Lee and K Jiang. "Fabrication of thick electroforming micro mould using a KMPR negative tone photoresist." *Journal of Micromechanics and Microengineering*, **18**:055032, 2008.

[LS96] F Laermer and A Schilp. "Method of anisotropically etching silicon.", March 26 1996. US Patent 5,501,893.

[LSC01] S Lebed, Z Stachura, M Cholewa, GJF Legge, J Lekki, S Maranda, A Potempa, C Sarnecki, Z Szklarz, J Styczen, et al. "The new Cracow scanning nuclear microprobe." *Nuclear Instruments and Methods in Physics Research Section B: Beam Interactions with Materials and Atoms*, **181**(1):95–98, 2001.

[Mac07] CA Mack. *Fundamental principles of optical lithography: the science of microfabrication*. Wiley-Interscience, Chichester, West Sussex, England, 2007.

[Mad02] MJ Madou. *Fundamentals of microfabrication: the science of miniaturization*. CRC Press, LLC, Boca Raton, FL, 2002.

[MH10] CE Mayes and GH Hoffstaetter. "Cornell energy recovery linac lattice and layout." In *Proceedings of the 1998 International Particle Accelerator Conference, Kyoto, Japan.*, volume 10, p. 2356, 2010.

[MHR11] G Marcus, E Hemsing, and J Rosenzweig. "Gain length fitting formula for free-electron lasers with strong space-charge effects"." *Physical Review Special Topics - Accelerators and Beams*, **14**(8), 2011.

[MIK04a] T Mihara, Y Iwashita, M Kumada, E Antokhin, E Sugiyama, and CM Spencer. "A super strong permanent magnet for the final focus quadrupole in a linear collider." In *Proceedings of the 2004 Asian Particle Accelerator Conference, Gyeongju, Korea*, pp. 22–26, May 2004.

[MIK04b] T Mihara, Y Iwashita, M Kumada, A Evgeny, and CM Spencer. "Super strong permanent magnet quadrupole for a linear collider." *IEEE Transactions on Applied Superconductivity*, **14**(2):469–472, 2004.

[MLM12] JJ Melone, KWD Ledingham, T McCanny, T Burris-Mog, U Schramm, R Grötzschel, S Akhmadaliev, D Hanf, KM Spohr, M Bussmann, et al. "Characterisation of permanent magnetic quadrupoles for focussing proton beams." *Nuclear Instruments and Methods in Physics Research Section A: Accelerators, Spectrometers, Detectors and Associated Equipment*, **676**:126–134, 2012.

[MME08] P Musumeci, JT Moody, RJ England, JB Rosenzweig, and T Tran. "Experimental generation and characterization of uniformly filled ellipsoidal electron-beam distributions." *Physical Review Letters*, **100**(24):244801, 2008.

[MMG09] JT Moody, P Musumeci, MS Gutierrez, JB Rosenzweig, and CM Scoby. "Longitudinal phase space characterization of the blow-out regime of RF photoinjector operation." *Physical Review Special Topics - Accelerators and Beams*, **12**(7):070704, 2009.

[MPB85] JB Murphy, C. Pellegrini, and R. Bonifacio. "Collective instability of a free electron laser including space charge and harmonics." *Optics Communications*, **53**(3):197–202, 1985.

[MS60] G Möllenstedt and R Speidel. "Elektronenoptischer Mikroschreiber unter elektronenmikroskopischer Arbeitskontrolle:(Informations-Speicherung auf kleinstem Raum)." *Physikalische Blätter*, **16**(4):192–198, 1960.

[MTW53] H Motz, W Thon, and RN Whitehurst. "Experiments on radiation by fast electron beams." *Journal of Applied Physics*, **24**(7):826–833, 1953.

[Nak09] E Nakamura. "Fast-rise high-field kicker magnet operating in saturation." *Nuclear Instruments and Methods in Physics Research Section A: Accelerators, Spectrometers, Detectors and Associated Equipment*, **612**(1):50–55, 2009.

[NTY11] E Nakamura, M Takayama, and S Yabukami. "Fast beam injection and ejection method using a short-pulsed septum magnet for Hadron accelerators." *Nuclear Instruments and Methods in Physics Research Section A: Accelerators, Spectrometers, Detectors and Associated Equipment*, **640**(1):29–37, 2011.

[NVP12] B Naranjo, A Valloni, S Putterman, and JB Rosenzweig. "Stable charged-particle acceleration and focusing in a laser accelerator using spatial harmonics." *Physical Review Letters*, **109**(16):164803, 2012.

[OCW02] T Ohkawa, Y Chiba, M Wakasugi, and T Katayama. "Magnetic field measurements of the kicker magnet for MUSES." In *Proceedings of the 2002 European Particle Accelerator Conference, Paris, France*, June 2002.

[OCW05] T Ohkawa, Y Chiba, and M Wakasugi. "Development of the kicker magnet for MUSES." *Nuclear Instruments and Methods in Physics Research Section A: Accelerators, Spectrometers, Detectors and Associated Equipment*, **547**(2):287–293, 2005.

[OHC06] B. Orlando, R. Hida, R. Cuchet, M. Audoin, B. Viala, D. Pellissier-Tanon, X. Gagnard, and P. Ancey. "Low-resistance integrated toroidal inductor for power management." *IEEE Transactions on Magnetics*, **42**(10):3374 –3376, oct. 2006.

[Oma90] Y Omata. "Magnetic properties of Fe-Co-Ni films with high saturation magnetization prepared by evaporation and electrodeposition." *IEEE Translation Journal on Magnetics in Japan*, **5**(1):17 –28, jan. 1990.

[OS99] PG O'Shea and L Spentzouris. "Particle beam sources working group report." In *AIP Conference Proceedings*, volume 472, p. 980742, 1999.

[OS12] Y Otake and RIKEN SPring. "Overview of SACLA machine status." In *Proceedings of 26th Linear Accelerator Conference, Tel-Aviv, Israel*, pp. 427–431. LINAC2012, 2012.

[OTH98] T Osaka, M Takai, K Hayashi, Y Sogawa, K Ohashi, Y Yasue, M Saito, and K Yamada. "New soft magnetic CoNiFe plated films with high B_s = 2.0-2.1 T." *IEEE Transactions on Magnetics*, **34**(4):1432 –1434, jul 1998.

[Pau90] KP Paulson. "Micro-undulator research at UCSB." *Nuclear Instruments and Methods in Physics Research Section A: Accelerators, Spectrometers, Detectors and Associated Equipment*, **296**(1-3):624–630, 1990.

[PBH00] IV Pogorelsky, I Ben-Zvi, T Hirose, S Kashiwagi, V Yakimenko, et al. "Demonstration of $8{\times}10^{18}$ photons/second peaked at 1.8 Å in a relativistic Thomson scattering experiment." *Physical Review Special Topics - Accelerators and Beams*, **3**(9):090702, 2000.

[PBM09] T Plettner, RL Byer, C McGuinness, and P Hommelhoff. "Photonic-based laser driven electron beam deflection and focusing structures." *Physical Review Special Topics - Accelerators and Beams*, **12**:101302, Oct 2009.

[PCP12] T Popmintchev, MC Chen, D Popmintchev, P Arpin, S Brown, S Ališauskas, G Andriukaitis, T Balčiunas, OD Mücke, A Pugzlys, et al. "Bright coherent ultrahigh harmonics in the keV x-ray regime from mid-infrared femtosecond lasers." *Science*, **336**(6086):1287–1291, 2012.

[PCT12] K Ta Phuoc, S Corde, C Thaury, V Malka, A Tafzi, JP Goddet, RC Shah, S Sebban, and A Rousse. "All-optical Compton gamma-ray source." *Nature Photonics*, **6**(5):308–311, 2012.

[Pel01] C Pellegrini. "The free electron laser collective instability and the development of X-Ray FELs." In *Proceedings of the 2001 Particle Accelerator Conference, Chicago, USA*. IEEE, IEEE, 2001.

[PLP10] G Priebe, D Laundy, PJ Phillips, DM Graham, SP Jamison, S Vassilev, EA Seddon, JB Rosenzweig, GA Krafft, T Heinzl, et al. "First results from the Daresbury Compton backscattering X-ray source (COBALD)." In *SPIE Optical Engineering and Applications*, pp. 780513–780513. International Society for Optics and Photonics, 2010.

[PW80] MW Poole and RP Walker. "Some limitations on the design of plane periodic electromagnets for undulators and free electron lasers." *Nuclear Instruments and Methods*, **176**(3):487–495, 1980.

[RBH94] J Rosenzweig, N Barov, S Hartman, M Hogan, S Park, C Pellegrini, G Travish, R Zhang, P Davis, G Hairapetian, et al. "Initial measurements of the UCLA RF photoinjector." *Nuclear Instruments and Methods in Physics Research Section A: Accelerators, Spectrometers, Detectors and Associated Equipment*, **341**(1):379–385, 1994.

[REK86] G Ramian, L Elias, and I Kimel. "Micro-undulator FELS." *Nuclear Instruments and Methods in Physics Research Section A: Accelerators, Spectrometers, Detectors and Associated Equipment*, **250**(1):125–133, 1986.

[RMG07] S Reiche, P Musumeci, and K Goldammer. "Recent upgrade to the free-electron laser code genesis 1.3." In *Proceedings of the 2007 Particle Accelerator Conference, Albuguerque, NM*, pp. 1269–1271. IEEE, 2007.

[RPB57] S Rubin, TO Passell, and LE Bailey. "Chemical analysis of surfaces by nuclear methods." *Analytical Chemistry*, **29**(5):736–743, 1957.

[RPP07] VA Rebrov, AG Ponomarev, VK Palchik, and NG Melnik. "The new design of magnetic quadrupole lens doublet manufactured from a single piece." *Nuclear Instruments and Methods in Physics Research Section B: Beam Interactions with Materials and Atoms*, **260**(1):34–38, 2007.

[RW06] J Rosenzweig and O Williams. "Limits on production of narrow band photons from inverse Compton scattering." In *AIP Conference Proceedings*, volume 877, p. 437, 2006.

[SBK10] F Stephan, CH Boulware, M Krasilnikov, J Bähr, G Asova, et al. "Detailed characterization of electron sources yielding first demonstration of European X-ray Free-Electron Laser beam quality." *Physical Review Special Topics - Accelerators and Beams*, **13**(2), 2010.

[SBS04] TC Sum, AA Bettiol, HL Seng, J.A. Kan, and F. Watt. "Direct measurement of proton-beam-written polymer optical waveguide sidewall morphorlogy using an atomic force microscope." *Applied Physics Letters*, **85**(8):1398–1400, 2004.

[Sch85] ET Scharlemann. "Wiggle plane focusing in linear wigglers." *Journal of Applied Physics*, **58**(6):2154 –2161, sep 1985.

[Sch13] MAH Schmeißer. "Emittance measurements of a superconducting high frequency electron gun." Forschungsbeleg, Humboldt Universität zu Berlin, July 2013.

[SGF88] RL Sheffield, ER Gray, and JS Fraser. "The Los Alamos Photoinjector Program." *Nuclear Instruments and Methods in Physics Research Section A: Accelerators, Spectrometers, Detectors and Associated Equipment*, **272**(1):222–226, 1988.

[Shi06] T Shintake et al. "Status of Japanese XFEL Project and SCSS test accelerator." In *Proceedings of the 28th Free Electron Laser Conference, Berlin, Germany*, p. 33, 2006.

[SLC96] RW Schoenlein, WP Leemans, AH Chin, P Volfbeyn, TE Glover, P Balling, M Zolotorev, KJ Kim, S Chattopadhyay, and CV Shank. "Femtosecond x-ray pulses at 0.4 Å generated by 90° Thomson scattering: a tool for probing the structural dynamics of materials." *Science*, **274**(5285):236, 1996.

[SPD07] NA Sayko, AG Ponomarev, and AA Drozdenko. "Beam scanning control and data acquisition on the Sumy nuclear microprobe." *Nuclear Instruments and Methods in Physics Research Section B: Beam Interactions with Materials and Atoms*, **260**(1):101–104, 2007.

[Spe01] CM Spencer. "Adjustable Permanent Quadrupoles for the Next Linear Collider." SLAC-PUB 8859, Stanford Linear Accelerator Center, Menlo Park, CA (US), 2001.

[SPR07] VE Storizhko, AG Ponomarev, VA Rebrov, AI Chemeris, AA Drozdenko, AB Dudnik, VI Miroshnichenko, NA Sayko, PA Pavlenko, and LP Peleshuk. "The Sumy scanning nuclear microprobe: Design features and first tests." *Nuclear Instruments and Methods in Physics Research Section B: Beam Interactions with Materials and Atoms*, **260**(1):49–54, 2007.

[SY10] EA Schneidmiller and MV Yurkov. "Using the longitudinal space charge instability for generation of vacuum ultraviolet and X-ray radiation." *Physical Review Special Topics - Accelerators and Beams*, **13**(11):110701–+, November 2010.

[TC87] R Tatchyn and PL Csonka. "Attainment of submillimeter periods and a 0.3-T peak field in a novel micropole undulator device." *Applied Physics Letters*, **50**(7):377–379, 1987.

[TCT89] R Tatchyn, P Csonka, and A Toor. "Perspectives on micropole undulators in synchrotron radiation technology." *Review of Scientific Instruments*, **60**(7):1796–1804, 1989.

[Tec14a] Radiabeam Technologies. "EMD-01-100-925 Dipole.", April 2014.

[Tec14b] Radiabeam Technologies. "EMD-01-130-1088 Dipole.", April 2014.

[Tec14c] Radiabeam Technologies. "EMD-01-201-787 Dipole.", April 2014.

[Tec14d] Radiabeam Technologies. "STM-01-340-110 Small Steering Magnet.", April 2014.

[Tec14e] Radiabeam Technologies. "STM-01-340-138 Medium Stering Magnet.", April 2014.

[TLK87] UA Tapper, NE Lövestam, Erik Karlsson, and Klas G Malmqvist. "A computer-controlled magnetic post-lens scanning system for the Lund proton microprobe." *Nuclear Instruments and Methods in Physics Research Section B: Beam Interactions with Materials and Atoms*, **28**(2):317–324, 1987.

[TOO01] K Tsuchiya, N Ohuchi, T Ogitsu, T Ozaki, and R Sugahara. "Superconducting final focusing system for KEKB." In *Proceedings of the 2001 Particle Accelerator Conference*, volume 1, pp. 181–185. IEEE, 2001.

[TPC12] G Tosin, P Palma Sanchez, JF Citadini, and C Castro Vergasta. "Super hybrid quadrupoles." *Nuclear Instruments and Methods in Physics Research Section A: Accelerators, Spectrometers, Detectors and Associated Equipment*, **674**:67–73, 2012.

[TSS09] AA Trusov, AR Schofield, and AM Shkel. "Performance characterization of a new temperature-robust gain-bandwidth improved MEMS gyroscope operated in air." *Sensors and Actuators A: Physical*, **155**(1):16–22, 2009.

[TTH89] R Tatchyn, A Toor, J Hunter, R Hornady, D Whelan, G Westenskow, P Csonka, T Cremer, and E Källne. "Generation of soft X-ray/VUV photons with a hybrid/bias micropole undulator on the LLNL linac." *Journal of X-Ray Science and Technology*, **1**(1):79–98, 1989.

[WBB06] JW Weigold, TJ Brosnihan, J Bergeron, and X Zhang. "A MEMS condenser microphone for consumer applications." In *19th IEEE International Conference on Micro Electro Mechanical Systems, 2006. (MEMS 2006 Istanbul)*, pp. 86–89. IEEE, 2006.

[WCB03] M Winkler, V Chichkine, K-H Behr, H Geissel, S Eliseev, A Kalimov, G Li, G Münzenberg, WR Plaß, C Scheidenberger, et al. "Development and test of iron-free quadrupole lenses with high magnetic flux densities." *Nuclear Instruments and Methods in Physics Research Section B: Beam Interactions with Materials and Atoms*, **204**:454–459, 2003.

[WFP11] R Weingartner, M Fuchs, A Popp, S Raith, et al. "Imaging laser-wakefield-accelerated electrons using miniature magnetic quadrupole lenses." *Physical Review Special Topics - Accelerators and Beams*, **14**(5), 2011.

[Wil46] RR Wilson. "Radiological use of fast protons." *Radiology*, **47**(5):487–491, 1946.

[WIW10] SM Wiggins, RC Issac, GH Welsh, E Brunetti, RP Shanks, et al. "High quality electron beams from a laser wakefield accelerator." *Plasma Physics and Controlled Fusion*, **52**(12):124032, 2010.

[WRP12] R Weingartner, Sebastian Raith, A Popp, S Chou, et al. "Ultralow emittance electron beams from a laser-wakefield accelerator." *Physical Review Special Topics - Accelerators and Beams*, **15**(11):111302, 2012.

[WZJ04] EN Wang, L Zhang, L Jiang, JM Koo, JG Maveety, EA Sanchez, KE Goodson, and TW Kenny. "Micromachined jets for liquid impingement cooling of VLSI chips." *Journal of Microelectromechanical Systems*, **13**(5):833 – 842, oct. 2004.

[Xie00] M Xie. "Exact and variational solutions of 3-D eigenmodes in high gain FELs." *Nuclear Instruments and Methods in Physics Research Section A: Accelerators, Spectrometers, Detectors and Associated Equipment*, **445**(1):59–66, 2000.

[YOG08] Y Yamaguchi, A Ozawa, A Goto, I Arai, T Fujinawa, N Fukunishi, T Kikuchi, T Ohnishi, T Ohtsubo, H Sakurai, et al. "Rare-RI ring project at RIKEN RI beam factory." *Nuclear Instruments and Methods in Physics Research Section B: Beam Interactions with Materials and Atoms*, **266**(19):4575–4578, 2008.

[ZCK13] Y Zhu, F Chen, W Kang, and X Sun. "Magnetic field design of the BAPS high precision quadrupole magnet." In *Proceedings of 2013 International Particle Accelerator Conference, Shanghai, China*, pp. 3531–3533, 2013.

[ZSC10] R Zheng, W Sun, and X Chen. "Characterizing and smoothing of striated sidewall morphology on UV-exposed thick SU-8 structures for micromachining millimeter wave circuits." *Journal of Micromechanics and Microengineering*, **20**:035007, 2010.

[ZSH04] W Zhang, J Sandberg, H Hahn, J Mi, C Pai, Y Tan, N Tsoupas, J Tuozzolo, W Warburton, J Wei, et al. "SNS extraction fast Kicker pulsed power system." In *Proceedings of the 2004 European Particle Accelerator Conference, Lucerne, Switzerland*, pp. 1810–1812, 2004.